Spatiotemporal Brain Imaging

by

Arthur K. Liu

B.S. EECS, M.I.T. 1993
M.S. EECS, M.I.T. 1995

Submitted to the Harvard-M.I.T. Division of Health Sciences and Technology
in partial fulfillment of the requirements for the degree of

Doctor of Philosophy in Medical Engineering
at the
Massachusetts Institute of Technology

June 2000

Signature of Author: _____
Division of Health Sciences and Technology
April 21, 2000

Certified by: _____
John W. Belliveau, Ph.D.
Associate Professor of Radiology
Thesis Supervisor

Accepted by: _____
Martha L. Gray, Ph.D.
Edward Hood Taplin Professor of Medical and Electrical Engineering
Co-director, Harvard-M.I.T. Division of Health Sciences and Technology

Spatiotemporal Brain Imaging

by

Arthur K. Liu

Submitted to the Harvard-M.I.T. Division of Health Sciences and Technology
On April 28, 2000 in partial fulfillment of the
Requirements for the Degree of Doctor of Philosophy in
Medical Engineering

Abstract

Understanding how the human brain works, in both health and disease, requires data with both high spatial and temporal resolution. This thesis develops and applies a spatiotemporal neuroimaging method. I describe a linear estimation inverse approach, which is a method for the combination of functional magnetic resonance imaging (fMRI) with electroencephalography (EEG) and magnetoencephalography (MEG). fMRI provides millimeter spatial resolution, while EEG and MEG provide millisecond temporal resolution. The thesis is divided into two broad sections: Monte Carlo modeling studies and experimental studies. Improvements to both the bioelectromagnetic forward and inverse solutions are demonstrated.

Through modeling studies, I characterize the accuracy of the method with and without functional and anatomic constraints, the effects of various model mis-specifications, and as a function of EEG/MEG sensor configuration. I describe a noise sensitivity normalization to the traditional linear estimation operator that improves the point spread function (a measure of spatial resolution), increases the spatial homogeneity of the point spread, and allows interpretation of the localization in terms of a statistical measure (F-statistic).

Using experimentally generated current dipoles implanted an epilepsy patient, I examine the accuracy of both a realistic and spherical EEG head model. This experimental data demonstrates the improved accuracy of the realistic head model, and gives us confidence in using this realistic head model for EEG source localization. The optimized and validated forward and inverse methods are then applied to a variety of empirical measurements.

First, the combined multimodality imaging approach is used to simultaneous EEG/fMRI measurements of a visual stimulus, demonstrating the feasibility of measuring and localizing simultaneously acquired electric potential and hemodynamic measurements. Second, combined MEG/fMRI measurements are used to analyze the spatiotemporal characteristics of a cortical network that is responsive to visual motion coherency. Finally, in epilepsy patients, I compare the non-invasive MEG localization of interictal spikes with verification from invasive recordings and surgical results.

These studies, in both normal volunteers and patients, clearly demonstrate the utility, accuracy, and power of the combined use of fMRI, EEG and MEG. The tools demonstrated here provide "real time movies" of the human brain at work during a given task or behavior. This information is required to develop computational models of how the human brain/mind works.

Thesis Supervisor: John W. Belliveau, Ph. D.
Title: Associate Professor of Radiology, Harvard Medical School
Director of Cognitive Neuroimaging, MGH NMR Center

Table of Contents

Acknowledgements

Five years ago, it all began with Jack and a trip to Taos. Right from the start, I realized I was going to be in for quite a ride. I was introduced to the inverse problem and big mountain skiing, all at once. Jack is truly a visionary. He shared with me his own dreams of understanding the human brain. And it was also on that Taos trip that Jack connected me with Anders. Over a span of four months in beautiful La Jolla, Anders laid the foundation for the rest of my work. I really got to know Anders (and the UCSD cleaning people), and that's where I learned to eat all sorts of weird sushi. Those two guys have really helped me develop into a competent scientist. They gave me the tools and the encouragement I needed and then let me loose. For all that (especially the sushi), I'll be forever grateful.

And thanks to my thesis committee chairman Bruce Rosen for taking time out of his busy schedule. I also thank Dr. David Cohen, Biomagnetism Group Leader at the Francis Bitter Magnet Laboratory at MIT. Through many discussions, he was helpful in clarifying various concepts, especially the controversy of MEG versus EEG localization accuracy.

Since I started, I've been able to interact with an amazing cast of characters – Bruce, Diana, Marty, Denis, Giorgio, Dave, Mette, Roger, Nouchine, Christian, Rahul, Eric, Yuka, Kevin, Tony, Thomas, Andre, Sean, Doug, Janine, Peter, and Kevin. A really important part of a Ph.D. is the environment you work in, and all you guys made the place fun and interesting. I also want to thank Dee Dee, Mary and Carol for all their help is getting the stuff I needed and thanks to Mary and Terry for their help in running the magnet.

And thanks to my family. They were there to help me through the toughest times, to help me keep moving forward. My folks have pushed me, even when I didn't want to be pushed. But they've only had my best interests in mind, it just took me a while to figure that out.

I don't know why everyone leaves the best for last, maybe it's because the last is the most memorable. The one person who will always be my most memorable is my wife, Namie. She's been with me, day in and day out, been with me the whole way. Who would've guessed the two of us would be here, now, together? I know Namie had to put up with a lot (and there's plenty more in the future), but the end of this part of the trip is in sight. I can't imagine life without her. I love sharing the good times with her, and she's always given me the support I needed to get through the tough times. And let's not forget Chilly – woof. LY.

You are not here merely to make a living. You are here to enable the world to live more amply, with greater vision, and with a finer spirit of hope and achievement. You are here to enrich the world. You impoverish yourself if you forget this errand.

Woodrow Wilson

1. Introduction

One of the greatest challenges of the 21st century is to understand how the human brain works in health and disease. According to our general model and hypothesis, "complex behavior is mapped at the level of multifocal neural systems rather than specific anatomical sites, giving rise to brain-behavior relationships that are both localized and distributed" (1-3). Understanding how the human brain works requires knowledge of this functional neuroanatomy; namely, "what" type of processing is performed, "where" different processing areas are, and "when" temporal processing is organized between distributed areas. Despite the rapid development of our ability to map "where" in the brain activity is taking place, our ability to map the timing of cortical activity within and between distributed neural networks (i.e., "when") remains a great challenge.

Detection and characterization of large-scale neural interactions requires neuroimaging techniques that can simultaneously sample the entire brain. Prior studies indicate that noninvasive spatiotemporal maps of cerebral activity can be produced by combining the high spatial resolution (millimeters) of functional magnetic resonance imaging (fMRI) (4-7) with the high temporal resolution (milliseconds) of electroencephalography (EEG) (8) and magnetoencephalography (MEG) (9). This multimodal imaging approach is based upon the premise that there exists a coupling between hemodynamics and neuronal activity. Evidence for this neuro-vascular coupling is reviewed in Section 1.3.

1.1 Inverse Approaches

One promising approach to satisfy these spatial and temproal neuroimaging requirements integrates data from multiple techniques. Various authors has proposed techniques for combining electromagnetic measurements (EEG/MEG) with anatomic and functional data (10-17). Localization of neuronal electrical activity within the brain, based upon external electromagnetic measurements (which is known as the electric/magnetic "inverse problem") is fundamentally ill-posed (18). That is, for any set of instantaneous EEG and/or MEG measurements, there are infinitely many electrical source distributions within the head that are consistent with those external recordings. Thus, in order to solve the inverse problem one must place some constraints on the otherwise infinite set of solutions. There are three general classes of inverse solutions used to estimate the location, orientation, and strength of electrical sources within the brain: 1) single/multiple dipole fitting, 2) subspace scanning, and 3) linear estimation.

Historically, the most common approach to the inverse problem has been the single/multiple dipole fitting. In this approach, one assumes that the electric and magnetic measurements are generated by a small number of focal sources, each of which can be modeled as a single fixed or moving dipole. The locations, orientations and strengths of these "equivalent current dipoles" (ECDs) can then be estimated by fitting these parameters using the electric and/or magnetic measurements (19). The dipole fitting involves a multi-dimensional, non-linear optimization. A disadvantage of this approach is that the time required to solve this optimization problem grows

exponentially with the number of ECDs, and thus the global optimum can be found only for models involving a small number of ECDs. For models involving larger numbers of ECDs, approximate techniques have to be used, where the solution found depends on the operator's initial estimate of the locations and orientations of the dipoles. A potential problem with all ECD-based methods is that the solution depends strongly upon the number of assumed dipoles. Although techniques have been proposed for estimating the model order (20-22), the actual number of dipoles cannot generally be determined.

The second type of inverse solution is the subspace scanning approach (20, 23). This method bases the source localization on the signal space, or conversely the noise space, from the actual EEG and/or MEG measurements from a given time window. The scanning procedure calculates the projection for each possible dipole into the signal space. That projection specifies how well a given dipole is able to explain the signal. One drawback to this method is that it is assumed that, for any given time window, only one single dipole is activated. In other words, the subspace scanning approaches will do poorly for extended sources or multiple sources that are temporally correlated, as is likely to be the case with actual human brain activity experiments.

The third general class of inverse approaches is the linear estimation procedure (12, 24-26). The linear estimation approach computes an optimal linear inverse operator which maps the external electromagnetic field measurements into estimated source activities within the brain. This inverse operator explicitly minimizes the expected error between the estimated and actual activity distribution. Unlike the two other general methods, in which activity is modeled as a small number of dipoles, a distributed source model is used by the linear estimation method. The main limitation of this type of inverse method is that the estimated localizations for focal sources are distributed (i.e. non-focal) in nature. For typical brain activation experiments, these assumptions are probably most appropriate. However, in special cases, such as the initial portion of an epileptic spike or for very focal activations (e.g. median nerve stimulation), the ECD approach may better model the focal sources.

1.2 Forward model - Anatomy

In order to solve the inverse problem, one must first solve the forward problem. That is, given the volume conduction properties of the head and the location and orientation of a source, one must calculate the corresponding external electric potentials and magnetic fields generate by that source. A more accurate respresentation of the head will improve any inverse approach used. Fortunately, today a great deal is known about the physiological properties and anatomy of the brain. The primary generators of EEG and MEG are synaptic currents, where the current flows crossing neuronal membranes act as tiny current sources or sinks, for current outflow and inflow, respectively. Note that for each neuron, the net current inflow and outflow through its membrane has to be zero (for conservation of charge). Thus, in order for these fields not to cancel out at the non-invasive sensors, there has to be some net spatial separation between the current sources and sinks within the neurons. Of course, the fields produced by individual neurons are far too weak to be externally observed non-invasively by EEG or MEG. Thus, to generate externally detectable signals, the neurons

within a volume of tissue must be aligned, and their synaptic current flows correlated in time. The scalp-recorded EEG and MEG reflect the linear superposition of the fields generated by all such synaptic currents, across all neurons (typically on the order of 10,000 – 100,000 (27)).

Of all the neurons in the human brain, the cortical pyramidal cells are particularly well suited to generate externally observable electric and magnetic fields, due to their elongated apical dendrites, systematically aligned in a columnar fashion perpendicular to the cortical sheet (27, 28). Inhibitory and excitatory synaptic inputs from different cell populations have characteristic laminar distributions, resulting in characteristic spatial and temporal patterns of net synaptic current flows at different depths through the cortical sheet (29-32). These current flows are typically strongly correlated laterally along the cortical sheet (33). Since the thickness of the cortical sheet is much smaller than the distance to the EEG and MEG sensors, the current source/sink distribution within a small slab of cortex can be represented by a current dipole oriented perpendicularly to the local cortical surface (12, 34), whose strength (moment) varies with time. It is possible to create an accurate representation of the cortical surface from a T1-weighted MRI dataset (12, 35, 36). Not only does this provide anatomic information for the inverse problem, the cortical surface representation is also a useful visualization tool. One can display cortical activity across the entire cortical hemisphere, providing significantly more topographic information than traditional slice data.

Another type of anatomic constraint is the anatomy of the head itself. When modelling the source generators, a model of the conductivity boundaries in the head is required. The simplest model of the head uses spherical surfaces. More realistic boundaries have been shown to provide more accurate source localizations ((37-40). In this thesis, I use realistic conductivity boundaries estimated from T1-weighted MRI to compute a boundary element method (BEM) head model for both EEG and MEG.

Both the cortical surface and the realistic conductivity boundaries can be used with any inverse approach. This type of anatomic data is used to generate a head model that relates source location and orientation to the external electromagnetic measurements. Any improvements in this head model should improve the inverse localization regardless of the method used (see Chapter 6).

1.3 Inverse Constraints - fMRI

So the question remains, which inverse approach should one use? We have chosen to pursue the linear estimation approach as the foundation of a multimodality imaging technique that provides high spatiotemporal resolution. There are three significant advantages with respect to the dipole fitting and subspace scanning methods. First, the linear estimation approach is less sensitive than the other two techniques to multiple, temporally correlated sources. Secondly, the continuous current source model is more biologically plausible and easier to relate to functional imaging data, which is itself distributed in nature, rather than discrete current dipoles. Finally, and more importantly, this approach provides a framework to incorporate spatial information from fMRI.

While numerous groups have combined fMRI with the dipole fitting approach (e.g. (41-43)), the fMRI was used to "guide" the manual placement of dipoles. The presence of manual intervention creates undesirable variations in source localizations that are operator dependent.

Our central hypothesis for incorporating fMRI with EEG/MEG is that the spatial localization of hemodynamic changes using fMRI corresponds to the region of cortical activity as measured by EEG/MEG. A variety of experimental data support this hypothesis.

1.3.1 Neuro-vascular coupling

One can examine this assumption of fMRI/EEG/MEG correlation as two separate questions. First, what is the coupling between neuronal activity and hemodynamic changes? Second, what aspects of the hemodynamic changes are measured using fMRI?

The issue of neuro-vascular coupling has been directly examined using optical imaging. Comparison of optical imaging of "intrinsic signals" (i.e. signals generated by the brain without exogenous contrast agents) with voltage sensitive dyes (44), electrophysiological measurements (44, 45), and cytochrome oxidase staining (45, 46) has demonstrated good correspondence between the different methods in the localization of cortical activity. Optical imaging uses light in or near the visible spectrum to illuminate exposed cortex. The reflected optical signal is then recorded as a function of space and time. These optical measurements reflects changes in 1) light scattering , 2) intrinsic chromophores, such as hemoglobin, cytochromes or NADH , and 3) blood volume (for reviews see (47-49)).

The current optical imaging data support the following model of the temporal orchestration of hemodynamic events following stimulation (46, 50-53). There is an initial increase in the metabolic demands for oxygen of the activated neurons. This increased consumption of oxygen results in an increase of deoxygenated hemoglobin (HbR), starting ~ 100 ms post-stimulus. Within 300 – 500 ms, there is an increase in blood volume due to capillary dilatation. The final hemodynamic event is an increase in blood flow, after 500 – 1500 ms, with the resulting increase in oxygenated hemoglobin (HbO) and decrease in HbR (52).

In addition to these optical studies, direct measurements of oxygen tension using an oxygen sensitive phosphorescent probe (54) provided an independent characterization of oxygen dynamics. Using a special probe with a phosphorescence lifetime that was inversely related to the oxygen tension (i.e. an increase in phosphorescence lifetime corresponded to a decrease in oxygen tension), they found an initial decrease, followed by a larger increase in oxygen tension with stimulation with a similar timecourse to the previous optical data.

The second aspect of neuro-vascular coupling is the spatial correlation between neuronal activity and the resulting hemodynamic changes. Clearly, the temporal changes in blood oxygenation (which takes seconds) are much slower than the underlying neuronal activity (which occurs over milliseconds). However, this difference in temporal dynamics does not necessarily restrict the use of hemodynamic

measurements as spatial constraints in the EEG/MEG inverse solution. The more relevant issue for use of fMRI to constrain the EEG/MEG inverse is the spatial correlation between neuronal activity and hemodynamic changes. Optical imaging localizations correlated well with electrophysiologic measurements (45), cytochrome oxidase staining (45, 46, 55), and lesion studies (45). It has also been demonstrated that different components of the hemodynamic signal measured optically varied in the spatial correlation. Using the early signal from HbR, it was possible to generate high resolution maps of cortical ocular dominance (50) and orientation columns (51). However, the later optical signals that arise from increased blood volume and flow were not able to represent this columnar architecture.

1.3.2 fMRI and neuro-vascular coupling

The current model of neuro-vascular coupling has significant implications for the collection and interpretation of fMRI (or any functional imaging technique that measures changes in hemodynamics). At this time, the majority of fMRI experiments use the positive blood oxygenation dependent (BOLD) signal (6, 7). BOLD contrast is based on changes in the oxygenation state of hemoglobin (56). Since HbR is paramagnetic, a decrease in HbR will result in a decrease of magnetic susceptibility and a corresponding increase in T2* weighted signal intensity.

The temporal dynamics of HbR determined optically predict that the BOLD fMRI signal should initially be negative (called the "initial dip") and then followed by a larger positive signal in activated regions. Also, the current optical data show that the early decrease in HbR is more spatially localized than the later changes in blood volume and flow that result in a decrease in HbR. This suggests that the initial dip should provide a more accurate representation of activated cortex.

The presence of an initial dip in BOLD fMRI has been shown in cats (57), monkeys (58) and humans (59-63). The initial dip was well localized to activated cortex, encompassing a smaller region than the delayed positive BOLD response (58-60, 63). Also, the initial dip was not found in large draining veins, where a large positive response was still seen (58, 60). This difference in spatial resolution between the initial dip and positive signal was put to use in (57). They used orientation gratings of different orientations to generate functional maps based on 1) the initial dip and 2) the delayed positive response. Only the initial dip functional map was able to represented the complementary nature of orthogonal orientation sensitivity. Also, the fMRI spatial mapping of orientation selectivity displayed similar pinwheel density and ratio of clockwise to counter-clockwise pinwheels as was found in electrophysiology and optical studies (44). These results suggest that spatially more accurate neuronal localization can be achieved by using the initial dip in fMRI.

Unfortunately, there is some controversy over the presence of the initial dip in BOLD fMRI. The initial dip was not seen in studies at 4.7 T in anesthetized cats (64), at 2 T in humans (65), and at 2 T and 4.7 T in anesthetized rats (66). Fransson et al. attributed the initial dip to overlap of the undershoot response when the inter-stimulus interval is too short. However, another study did detect the initial dip independent of the inter-stimulus interval (62). Some possible explanations offered for the absence of the

initial dip in these studies include low temporal resolution (64), low signal to noise (64), and insufficient resolution which would result in partial voluming effects that might obscure the initial dip (66).

While the controversy of the initial dip in fMRI has yet to be resolved, the final outcome may not have significant implications for the general use of fMRI as a spatial constraint for the EEG/MEG inverse problem. It is still likely that the spatial resolution of fMRI is, in many cases, still much higher that is reasonable achievable for EEG/MEG localization. The cortical point spread function based on optical measurements has been estimated in primary visual cortex of the macaque to be 1.5 mm (antero-posterior) by 2.7 mm (medio-lateral) (67). The fMRI resolution in human visual cortex, which would be expected to be larger than the optical cortical point spread function (since it would incorporate the cortical point spread function, hemodynamic spread and additional fMRI measurement error), has been estimated to be 3.5 mm(68). We typically tessellate the cortical surface with one dipole per 10 mm along the cortical surface, and thus, spread on the order of 5 mm is relatively insignificant.

1.4 Summary

I am pursuing a multimodality imaging approach that combines hemodynamic measurements from fMRI with electromagnetic measurements from EEG and MEG. This approach provides both high spatial resolution and high temporal resolution. By incorporating anatomic and functional information (as opposed to just mathematical constraints), I hope to further refine and improve the non-invasive localization of human brain activity.

My thesis consists of three general parts. The first is an overview of the forward and inverse problem. The second part consists of various modelling work to characterize the accuracy of the linear estimation approach with and without fMRI and with various combinations of EEG and MEG sensors. Within the second part, I also present a noise sensitivity normalization for the linear estimation approach that provides significant gains in spatial resolution. Finally, the last section consists of various experimental studies: 1) experimental verification of the EEG forward solution, 2) combined EEG/fMRI studies of a simple visual stimulus (flashing checkerboards), 3) combined MEG/fMRI studies of coherent and incoherent visual motion, and 4) MEG studies of interictal activity in epilepsy patients.

1.5 References

1. Mesulam M-M. Large-scale neurocognitive networks and distributed processing for attention, language, and memory. *Ann. Neurol.* 1990; 28: 597-613.
2. McIntosh AR, Rajah MN, and Lobaugh NJ. Interactions of prefrontal cortex in relation to awareness in sensory learning. *Science.* 1999; 284: 1531-1533.
3. Buechel C, Coull JT, and Friston KJ. The predictive value of changes in effective connectivity for human learning. *Science.* 1999; 283: 1538-1541.
4. Bandettini PA, Wong EC, Hinks RS, Tikofsky RS, and Hyde JS. Time course EPI of human brain function during task activation. *Magn. Reson. Med.* 1992; 25: 390-397.

5. Belliveau JW, Kennedy DN, McKinstry RC, Buchbinder BR, Weisskoff RM, Cohen MS, Vevea JM, Brady TJ, and Rosen BR. Functional mapping of the human visual cortex by magnetic resonance imaging. *Science.* 1991; 254: 716-719.
6. Kwong KK, Belliveau JW, Chesler DA, Goldberg IE, Weisskoff RM, Poncelet BP, Kennedy DN, Hoppel BE, Cohen MS, Turner R, Cheng HM, Brady TJ, and Rosen BR. Dynamic magnetic resonance imaging of human brain activity during primary sensory stimulation. *Proc. Natl. Acad. Sci. USA.* 1992; 89: 5675-5679.
7. Ogawa S, Tank DW, Menon R, Ellermann JM, Kim S-G, Merkle H, and Ugurbil K. Intrinsic signal changes accompanying sensory stimulation: Functional brain mapping with magnetic resonance imaging. *Proc. Natl. Acad. Sci. USA.* 1992; 89: 5951-5955.
8. Berger H. On the electroencephalogram of man. *Archiv. fur Psychiatrie Nervenkrankheiten.* 1929; 87: 527-570.
9. Cohen D. Magnetic field measurements of human alpha rhythm. *Science.* 1968; 161: 784-786.
10. Belliveau JW. MRI techniques for functional mapping of the human brain: integration with PET, EEG/MEG and infrared spectroscopy. In: Uemura K, Lassen NA, Jones T, and Kanno I, eds. *Quantification of Brain Function. Tracer Kinetics and Image Analysis in Brain PET.* Amsterdam: Elsevier Science Publishers, 1993: 639-667.
11. Belliveau JW. Functional imaging of the brain. In: *Proceedings of the Eleventh Annual Meeting of the Society of Magnetic Resonance in Medicine, Berlin, Germany, 1992.* SMRM, Berkeley. 203.
12. Dale AM and Sereno MI. Improved localization of cortical activity by combining EEG and MEG with MRI cortical surface reconstruction: A linear approach. *J. Cog. Neurosci.* 1993; 5: 162-176.
13. George JS, Aine CJ, Mosher JC, Schmidt DM, Ranken DM, Schlitt HA, Wood CC, Lewine JD, Sanders JA, and Belliveau JW. Mapping function in the human brain with MEG, anatomical MRI and functional MRI. *J. Clin. Neurophysiology.* 1995; 12: 406-431.
14. Liu AK, Belliveau JW, and Dale AM. Spatiotemporal imaging of human brain activity using fMRI constrained MEG data: Monte Carlo simulations. *Proc. Natl. Acad. Sci. USA.* 1998; 95: 8945-8950.
15. Heinze HJ, Mangun GR, Burchert W, Hinrichs H, Scholz M, Munte TF, Gos A, Scherg M, Johannes S, Hundeshagen H, and et al. Combined spatial and temporal imaging of brain activity during visual selective attention in humans. *Nature.* 1994; 372: 543-546.
16. Snyder AZ, Abdullaev YG, Posner MI, and Raichle ME. Scalp electrical potentials reflect regional cerebral blood flow responses during processing of written words. *PNAS.* 1995; 92: 1689-1693.
17. Dale AM, Liu AK, Fischl B, Oostendorp TF, Buckner RL, Belliveay JW, Rosen BR, Lewine JD, and Halgren E. Dynamic statistical parametric mapping: combining fMRI and MEG to produce high-resolution spatiotemporal maps of cortical activity. *Neuron.* in press;

18. Helmholtz H. Ueber einige Gesetze der Vertheilung elektrischer Strome in korperlichen Leitern, mit Anwendung auf die thierisch-elektrischen Versuche. *Ann. Phys. Chem.* 1853; 89: 211-233, 353-377.
19. Scherg M. Functional imaging and localization of electromagnetic brain activity. *Brain Topography.* 1992; 5: 103-11.
20. Mosher JC, Lewis PS, and Leahy RM. Multiple dipole modeling and localization from spatio-temporal MEG data. *IEEE Trans Biomed Engr.* 1992; 39: 541-557.
21. Supek S and Aine CJ. Simulation studies of multiple dipole neuromagnetic source localization: model order and limits of source resolution. *IEEE Trans. Biomed. Eng.* 1993; 40: 529-540.
22. Gorodnitsky IF, George JS, and Rao BD. Neuromagnetic source imaging with FOCUSS: a recursive weighted minimum norm algorithm. *Electroencephalogr Clin Neurophysiol.* 1995; 95: 231-51.
23. Schwartz D, Badier J, Bihoué P, and Bouliou A. Evaluation of a new MEG-EEG spatio-temporal localization approach using realistic sources. *Brain Topography.* 1999; In Press.
24. Hamalainen MS and Ilmoniemi RJ. *Interpreting measured magnetic fields of the brain: estimates of current distributions.* Helsinki, Finland: Helsinki Univ. of Technology, 1984:
25. Phillips JW, Leahy RM, Mosher JC, and Timsari B. Imaging neural activity using MEG and EEG. *IEEE Eng Med Biol Mag.* 1997; 16: 34-42.
26. Smith WE. Estimation of the spatio-temporal correlations of biological electrical sources from their magnetic field. *IEEE Trans Biomed Eng.* 1992; 39: 997-1004.
27. Nunez PL. *Electric fields of the brain.* New York: Oxford University Press, 1981:
28. Okada Y, Lauritzen M, and Nicholson C. MEG source models and physiology. *Phys Med Biol.* 1987; 32: 43-51.
29. Nicholson C and Freeman JA. Theory of current source density analysis and determination of the conductivity tensor for anuran cerebellum. *J Neurophysiol.* 1975; 38: 356-368.
30. Mitzdorf U. Current source-density method and application in cat cerebral cortex: investigation of evoked potentials and EEG phenomena. *Physiol Rev.* 1985; 65: 37-100.
31. Barth DS and Di S. Laminar excitability cycles in neocortex. *J Neurophysiol.* 1991; 65: 891-8.
32. Schroeder CE, Steinschneider M, Javitt DC, Tenke CE, Givre SJ, Mehta AD, Simpson GV, Arezzo JC, and Vaughan HG, Jr. Localization of ERP generators and identification of underlying neural processes. *Electroencephalogr Clin Neurophysiol Suppl.* 1995; 44: 55-75.
33. Sukov W and Barth DS. Three-dimensional analysis of spontaneous and thalamically evoked gamma oscillations in auditory cortex. *J Neurophysiol.* 1998; 79: 2875-84.
34. Wood CC, George JS, Lewis PS, Ranken DM, and Heller L. Anatomical constraints for neuromagnetic source models. In: *Proceedings of the Society for Neuroscience, 1990.* 1241.

35. Dale AM, Fischl B, and Sereno MI. Cortical Surface-Based Analysis I: Segmentation and Surface Reconstruction. *NeuroImage*. 1999; 9: 179-194.
36. Fischl B, Sereno MI, and Dale AM. Cortical Surface-Based Analysis II: Inflation, Flattening, a Surface-Based Coordinate System. *NeuroImage*. 1999; 9: 195-207.
37. Cuffin BN. EEG localization accuracy improvements using realistically shaped head models. *IEEE Trans Biomed Eng*. 1996; 43: 299-303.
38. Fuchs M, Drenckhahn R, Wischmann HA, and Wagner M. An improved boundary element method for realistic volume-conductor modeling. *IEEE Trans Biomed Eng*. 1998; 45: 980-97.
39. Herrendorf G, B.J. S, Kolle R, Baudewig J, Waberski TD, Buchner H, and Paulus W. Dipole-source analysis in a realistic head model in patients with focal epilepsy. *Epilepsia*. 2000; 41: 71-80.
40. Liu AK, Cuffin BN, Belliveau JW, Ives J, Blume H, Halgren E, Schomer DL, and Dale AM. Accuracy of a Realistic and Spherical EEG head model. *J Clin Neurophys*. submitted;
41. Korvenoja A, Huttunen J, Salli E, Pohjonen H, Martinkauppi S, Palva JM, Lauronen L, Virtanen J, Ilmoniemi RJ, and Aronen HJ. Activation of multiple cortical areas in response to somatosensory stimulation: combined magnetoencephalographic and functional magnetic resonance imaging. *Hum Brain Mapp*. 1999; 8: 13-27.
42. Ahlfors SP, Simpson GV, Dale AM, Belliveau JW, Liu AK, Korvenoja A, Virtanen J, Huotilainen M, Tootell RB, Aronen HJ, and Ilmoniemi RJ. Spatiotemporal activity of a cortical network for processing visual motion revealed by MEG and fMRI. *J Neurophysiol*. 1999; 82: 2545-55.
43. Opitz B, Mecklinger A, Von Cramon DY, and Kruggel F. Combining electrophysiological and hemodynamic measures of the auditory oddball. *Psychophysiology*. 1999; 36: 142-7.
44. Grinvald A, Lieke E, Frostig RD, Gilbert CD, and Wiesel TN. Functional architecture of cortex revealed by optical imaging of intrinsic signals. *Nature*. 1986; 324: 361-364.
45. Masino SA, Kwon MC, Dory Y, and Frostig RD. Characterization of functional organization within rat barrel cortex using intrinsic signal optical imaging through a thinned skull. *Proc Natl Acad Sci U S A*. 1993; 90: 9998-10002.
46. Grinvald A, Frostig RD, Siegel RM, and Bartfeld E. High-resolution optical imaging of functional brain architecture in the awake monkey. *Proc Natl Acad Sci U S A*. 1991; 88: 11559-63.
47. Cohen LB. Changes in neuron structure during action potential propagation and synaptic transmission. *Physiol Rev*. 1973; 53: 373-418.
48. Chance B, Wang NG, Maris M, Nioka S, and Sevick E. Quantitation of tissue optical characteristics and hemoglobin desaturation by time- and frequency-resolved multi-wavelength spectrophotometry. *Adv Exp Med Biol*. 1992; 317: 297-304.
49. Villringer A and Chance B. Non-invasive optical spectroscopy and imaging of human brain function. *Trends Neurosci*. 1997; 20: 435-42.
50. Frostig RD, Lieke EE, Ts'o DY, and Grinvald A. Cortical functional architecture and local coupling between neuronal activity and the microcirculation revealed by in vivo

high-resolution optical imaging of intrinsic signals. *Proc. Natl. Acad. Sci. USA*. 1990; 87: 6082-6086.
51. Malonek D and Grinvald A. Interactions between electrical activity and cortical microcirculation revealed by imaging spectroscopy: implications for functional brain mapping. *Science*. 1996; 272: 551-554.
52. Malonek D, Dirnagl U, Lindauer U, Yamada K, Kanno I, and Grinvald A. Vascular imprints of neuronal activity: relationships between the dynamics of cortical blood flow, oxygenation, and volume changes following sensory stimulation. *Proc Natl Acad Sci U S A*. 1997; 94: 14826-31.
53. Grinvald A, Slovin H, and Vanzetta I. Non-invasive visualization of cortical columns by fMRI. *Nat Neurosci*. 2000; 3: 105-107.
54. Vanzetta I and Grinvald A. Increased cortical oxidative metabolism due to sensory stimulation: implications for functional brain imaging. *Science*. 1999; 286: 1555-8.
55. Dowling JL, Henegar MM, Liu D, Rovainen CM, and Woolsey TA. Rapid optical imaging of whisker responses in the rat barrel cortex. *J Neurosci Methods*. 1996; 66: 113-22.
56. Pauling L and Coryell CD. The magnetic properties and structure of hemoglobin, oxyhemoglobin and carbonmonoxyhemoglobin. *Proc. Natl. Acad. Sci. (USA)*. 1936; 22: 210-216.
57. Kim DS, Duong TQ, and Kim SG. High-resolution mapping of iso-orientation columns by fMRI. *Nat Neurosci*. 2000; 3: 164-169.
58. Logothetis NK, Guggenberger H, Peled S, and Pauls J. Functional imaging of the monkey brain. *Nat Neurosci*. 1999; 2: 555-62.
59. Menon RS, Ogawa S, Hu X, Strupp JP, Anderson P, and Ugurbil K. BOLD based functional MRI at 4 Tesla includes a capillary bed contribution: echo-planar imaging correlates with previous optical imaging using intrinsic signals. *Magn Reson Med*. 1995; 33: 453-9.
60. Hu X, Le TH, and Ugurbil K. Evaluation of the early response in fMRI in individual subjects using short stimulus duration. *Magn Reson Med*. 1997; 37: 877-84.
61. Ernst T and Hennig J. Observation of a fast response in functional MR. *Magn Reson Med*. 1994; 32: 146-9.
62. Yacoub E, Le TH, Ugurbil K, and Hu X. Further evaluation of the initial negative response in functional magnetic resonance imaging. *Magn Reson Med*. 1999; 41: 436-41.
63. Yacoub E and Hu X. Detection of the early negative response in fMRI at 1.5 Tesla. *Magn Reson Med*. 1999; 41: 1088-92.
64. Jezzard P, Rauschecker JP, and Malonek D. An in vivo model for functional MRI in cat visual cortex. *Magn Reson Med*. 1997; 38: 699-705.
65. Fransson P, Kruger G, Merboldt KD, and Frahm J. Temporal characteristics of oxygenation-sensitive MRI responses to visual activation in humans. *Magn Reson Med*. 1998; 39: 912-9.
66. Marota JJ, Ayata C, Moskowitz MA, Weisskoff RM, Rosen BR, and Mandeville JB. Investigation of the early response to rat forepaw stimulation. *Magn Reson Med*. 1999; 41: 247-52.

67. Grinvald A, Lieke EE, Frostig RD, and Hildesheim R. Cortical point-spread function and long-range lateral interactions revealed by real-time optical imaging of macaque monkey primary visual cortex. *J Neurosci.* 1994; 14: 2545-68.
68. Engel SA, Glover GH, and Wandell BA. Retinotopic organization in human visual cortex and the spatial precision of functional MRI. *Cereb Cortex.* 1997; 7: 181-92.

2. Forward/Inverse Background

2.1 Forward Solution

In the typical frequency range of neural activity of 1000 Hz, the electric and magnetic fields of the brain can be accounted for by the quasi-static limit of Maxwell's equations -- that is, magnetic induction and capacitive effects are negligible (1, 2). For a linear isotropic material where the polarization is linearly related to the electric field, Ampère's Law can be written as:

$$\nabla \times \mathbf{H} = \mathbf{J} + \frac{\partial \mathbf{D}}{\partial t} \qquad [2.1.1]$$

where the constitutive equations relating **D** (electric displacement flux density) and **J** (current density) to **E** (electric field intensity) are $\mathbf{D} = \varepsilon \mathbf{E}$ and $\mathbf{J} = \sigma \mathbf{E}$. (For these equations, bold denotes a vector field.) Rewriting in the time-harmonic form gives:

$$\nabla \times \mathbf{H} = \mathbf{J} + j\omega \mathbf{D} \qquad [2.1.2]$$

Replacing **J** and **D** with their constitutive equations:

$$\nabla \times \mathbf{H} = (\sigma + j\omega\varepsilon)\mathbf{E} \qquad [2.1.3]$$

In the quasistatic limit, the electric and magnetic fields are uncoupled:

$$\nabla \times \mathbf{H} \approx \mathbf{J} = \sigma \mathbf{E} \qquad [2.1.4]$$

Therefore the conduction term of Ampère's Law must dominate the right hand side, i.e.:

$$\frac{\sigma}{\omega\varepsilon} >> 1 \qquad [2.1.5]$$

For typical values of $\sigma = 0.3 \frac{S}{m}$, $\varepsilon = 10^5 \varepsilon_o = 8.85 \times 10^{-7} \frac{F}{m}$, and $\omega = 2\pi(1000)$rad (3)

$$\frac{\sigma}{\omega\varepsilon} = 53.98 >> 1 \qquad [2.1.6]$$

and thus the quasistatic approximation is reasonable.

The quasistatic equations governing the magnetic field are:

$$\nabla \times \mathbf{H} \approx \mathbf{J} \qquad [2.1.7]$$

$$\nabla \cdot \mu_o \mathbf{H} = \nabla \cdot \mathbf{B} = 0 \qquad [2.1.8]$$

where **B** is the magnetic flux density. Since a vector field is uniquely specified by its curl and divergence, these two equations uniquely specify **H**. Since $\nabla \cdot (\nabla \times \mathbf{A}) = 0$ identically, one can define **A**, the vector potential, to be the solution to Equation 2.1.8:

$$\mathbf{B} = \nabla \times \mathbf{A} \qquad [2.1.9]$$

To uniquely specify the vector potential also requires the divergence of **A**. As a matter of convenience,

$$\nabla \cdot \mathbf{A} = 0 \qquad [2.1.10]$$

Substituting Equation 2.1.9 into Equation 2.1.7:

$$\nabla \times (\nabla \times \mathbf{A}) = \nabla(\nabla \cdot \mathbf{A}) - \nabla^2 \mathbf{A} = -\nabla^2 \mathbf{A} = \mu_o \mathbf{J} \qquad [2.1.11]$$

The integral of this equation, known as the superposition integral for the vector potential, is:

$$\mathbf{A}(\mathbf{r}) = \frac{\mu_o}{4\pi} \int_{V'} \frac{\mathbf{J}(\mathbf{r}')}{|\mathbf{r} - \mathbf{r}'|} dv' \qquad [2.1.12]$$

where **r** is the coordinate where **A** is being evaluated and **r′** is the coordinate of the current density source. Evaluating Equation 2.1.9:

$$\mathbf{B} = \nabla \times \mathbf{A} = \frac{1}{4\pi} \nabla \times \int_{V'} \frac{\mathbf{J}(\mathbf{r}')}{|\mathbf{r} - \mathbf{r}'|} dv' \qquad [2.1.13]$$

Since the curl operation is taken with respect to the observer (at **r**) and the integration is taken with respect to the source (at **r′**), the order of the curl and the integration can be reversed:

$$\mathbf{B} = \frac{\mu_o}{4\pi} \int_{V'} \frac{\nabla \times \mathbf{J}(\mathbf{r}')}{|\mathbf{r} - \mathbf{r}'|} dv' \qquad [2.1.14]$$

Using the vector identity $\nabla \times (\psi \mathbf{J}) = \psi \nabla \times \mathbf{J} + \nabla \psi \times \mathbf{J}$, where ψ is a scalar, and noting that the first term of the identity is 0 since the curl operation has no dependence on the source at coordinates **r′**, the above expression can be rewritten as:

$$\mathbf{B} = \frac{\mu_o}{4\pi} \int_{V'} \left[\nabla \left(\frac{1}{|\mathbf{r} - \mathbf{r}'|} \right) \times \mathbf{J}(\mathbf{r}') \right] dv' \qquad [2.1.15]$$

Defining a unit vector $\mathbf{i}_{r'r}$ pointing from the source to the observer,

$$\nabla \left(\frac{1}{|\mathbf{r} - \mathbf{r}'|} \right) = -\frac{\mathbf{i}_{r'r}}{|\mathbf{r} - \mathbf{r}'|^2} = -\nabla' \left(\frac{1}{|\mathbf{r} - \mathbf{r}'|} \right) \qquad [2.1.16]$$

This gives the Biot-Savart Law for magnetic flux density:

$$\mathbf{B} = \frac{\mu_o}{4\pi} \int_{V'} \frac{\mathbf{J}(\mathbf{r}') \times \mathbf{i}_{r'r}}{|\mathbf{r} - \mathbf{r}'|^2} dv' \qquad [2.1.17]$$

This results in a simple linear relationship between the electric and magnetic recordings, and the components of dipole moment at any location in the brain. This allows us to express the forward solution in a simple matrix form:

$$\mathbf{x} = \mathbf{A}\mathbf{s} + \mathbf{n} \qquad [2.1.18]$$

where **x** is the vector of instantaneous electric and/or magnetic recordings, **A** is the so-called *gain matrix* (with each column specifying the electric and/or magnetic forward solution for a given dipole component), **s** is a vector of dipole component strengths, and **n** is a vector specifying the noise at each electrode/sensor. The elements of **A** are complicated non-linear functions of the sensor locations, and the geometry and conductive properties of the head.

Historically, the gain matrix has been calculated assuming an idealized head-shape, typically multiple concentric spheres of different conductivities, e.g. (4). However, recent advances in numerical techniques and computer technology have made it practical to compute the forward solution for a more realistic non-spherical head. Furthermore, the advent of high-resolution 3-D MRI scans has made it possible to customize such realistic models to each individual subject's anatomy (5). The details of the generation of the conductivity boundaries are presented in the 4.1 Surface Studies Methods.

2.2 Inverse operator

In the anatomically constrained linear estimation approach, a linear estimator

$$\hat{\mathbf{s}} = \mathbf{W}\mathbf{x} \qquad [2.2.1]$$

is sought which minimizes the expected error, Err_W (in a least-squares sense), of the dipole strength over the cortical surface defined as:

$$Err_W = \left\langle \left\| \hat{\mathbf{s}} - \mathbf{s} \right\|^2 \right\rangle \qquad [2.2.2]$$

where **W** is a linear operator that maps a recording vector **x** into an estimated solution vector $\hat{\mathbf{s}}$. Assuming additive Gaussian noise and the forward model specified in Equation 2.1.18, the optimal linear inverse estimator is given by (see 2.3 Inverse Operator Derivations):

$$\mathbf{W} = \mathbf{R}\mathbf{A}^{\mathsf{T}}\left(\mathbf{A}\mathbf{R}\mathbf{A}^{\mathsf{T}} + \mathbf{C}\right)^{-1} \qquad [2.2.3]$$

where **C** is the covariance matrix of **n**, and **R** is the *a priori* covariance matrix estimate for **s**. Note that if both **C** and **R** are set to a scalar multiple of the identity matrix then this approach reduces to the well-known minimum-norm solution (3). In practice, the noise covariance matrix, **C**, can be estimated from the actual recording data [see, e.g., (3)]. Various derivations of the inverse operator follow in the next section.

This approach provides a convenient framework for incorporating information from fMRI into the inverse problem. A reasonable hypothesis is that there is a positive correlation between local electric/magnetic activity and local hemodynamic response over time. Since the diagonal elements of the matrix **R** encode the prior estimates of dipole strength variance (power) over time at each location i ($\mathbf{R}_{ii} = \sigma_i^2 = \langle s_i^2 \rangle$), this assumption can be incorporated by making each diagonal element $\mathbf{R}_{ii}$ a function of the corresponding fMRI activation. Large values indicate those locations that are more likely to be active and small values indicate that are less likely to be active. Setting $\mathbf{R}_{ii}$ to zero effectively precludes any activity at location i.

If one had knowledge of the correlation of activity between different sources, say locations i and j, such information could be incorporated through the off-diagonal elements of the **R** matrix, by setting $\mathbf{R}_{ij} = \langle s_i s_j \rangle = \sigma_i \sigma_j \mathrm{corr}(i,j)$. Although not considered in these study, this would impose a smoothness constraint on the inverse solution, as suggested by the LORETA approach (6).

The two different categories of mis-specifications will typically affect two different components of the inverse operator. Fundamental mis-specifications affect the **R** matrix, while experimental mis-specifications affect the **A** matrix.

Once the optimal linear inverse estimator **W** is calculated for a given anatomy (cortical surface), sensor placement, and fMRI activation, the estimated spatiotemporal pattern of electric/magnetic activity (dipole strength) can be calculated using the simple expression

$$\hat{\mathbf{s}}(t) = \mathbf{W}\mathbf{x}(t) \qquad [2.2.4]$$

where $\hat{\mathbf{s}}(t)$ and $\mathbf{x}(t)$ are the estimated dipole strength and recording vectors as a function of time.

2.3 Inverse Operator Derivations

Shown here are four different derivations of the linear inverse operator: 1) minimization of expected error (5, 7-9), 2) Bayesian formulation (10-13), 3) Tichonov regularization (14), and 4) generalized Wiener filtering (15-18). All derivations arrive at equivalent inverse operators.

The minimization of expected error begins with a set of measurements

$$\mathbf{x} = \mathbf{As} + \mathbf{n} \qquad [2.3.1]$$

where **x** is the measurement vector, **A** is the gain matrix, **s** is the strength of each dipole component, and **n** is the noise vector. One would like to calculate a linear inverse operator **W** that minimizes the expected difference between the estimated and the correct source solution. The expected error can be defined as:

$$Err_W = \left\langle \left| \mathbf{W}\,\mathbf{x} - \hat{\mathbf{s}} \right|^2 \right\rangle \qquad [2.3.2]$$

Assuming both **n** and **s** are normally distributed with zero mean and covariance matrices **C** and **R**, respectively, the expected error can be rewritten as:

$$Err_W = \left\langle \left| \mathbf{W}(\mathbf{As}+\mathbf{n}) - \mathbf{s} \right|^2 \right\rangle \qquad [2.3.3]$$

$$= \left\langle \left| (\mathbf{WA} - \mathbf{I})\mathbf{s} + \mathbf{Wn} \right|^2 \right\rangle \qquad [2.3.4]$$

$$= \left\langle \left| \mathbf{Ms} + \mathbf{Wn} \right|^2 \right\rangle \qquad [2.3.5]$$

where $\mathbf{M} = \mathbf{WA} - \mathbf{I}$

$$= \left\langle |\mathbf{Ms}|^2 \right\rangle + \left\langle |\mathbf{Wn}|^2 \right\rangle \qquad [2.3.6]$$

$$= \mathrm{tr}(\mathbf{MRM}^T) + \mathrm{tr}(\mathbf{WCW}^T) \qquad [2.3.7]$$

where tr(**A**) is the trace of **A** and is defined as the sum of the diagonal entries

Re-expanding the expression gives

$$= \mathrm{tr}(\mathbf{WARA}^T\mathbf{W}^T - \mathbf{RA}^T\mathbf{W}^T - \mathbf{WAR} + \mathbf{R}) + \mathrm{tr}(\mathbf{WCW}^T) \qquad [2.3.8]$$

The second and third terms can be shown to be equivalent:

$$\mathbf{RA}^T\mathbf{W}^T = \mathbf{RA}^T\left(\mathbf{RA}^T\left(\mathbf{ARA}^T + \mathbf{C}\right)^{-1}\right)^T \qquad [2.3.9]$$

$$= \mathbf{RA}^T\left(\left(\mathbf{ARA}^T + \mathbf{C}\right)^{-1}\right)^T\mathbf{AR} \qquad [2.3.10]$$

One can show that the term inside the parentheses is also symmetric (given that the noise covariance matrix, **C**, is symmetric):

$$\left(\mathbf{ARA}^T + \mathbf{C}\right)^T = \mathbf{AR}^T\mathbf{A}^T + \mathbf{C}^T = \mathbf{ARA}^T + \mathbf{C} \qquad [2.3.11]$$

Since the inverse of a symmetric matrix is also symmetric, one can further simplify Eq. 2.3.10:

$$= \mathbf{RA}^T\left(\mathbf{ARA}^T + \mathbf{C}\right)^{-1}\mathbf{AR} = \mathbf{WAR} \qquad [2.3.12]$$

Substituting into Eq. 2.3.8:

$$= \mathrm{tr}(\mathbf{WARA}^T\mathbf{W}^T - 2\mathbf{RA}^T\mathbf{W}^T + \mathbf{R}) + \mathrm{tr}(\mathbf{WCW}^T) \quad [2.3.13]$$

This last expression can be explicitly minimized by taking the gradient with respect to **W**, setting it to zero and solving for **W**.

$$0 = 2\mathbf{WARA}^T - 2\mathbf{RA}^T + 2\mathbf{WC} \quad [2.3.14]$$

$$\mathbf{WARA}^T + \mathbf{WC} = \mathbf{RA}^T \quad [2.3.15]$$

$$\mathbf{W}(\mathbf{ARA}^T + \mathbf{C}) = \mathbf{RA}^T \quad [2.3.16]$$

This yields the expression for the linear inverse operator:

$$\mathbf{W} = \mathbf{RA}^T(\mathbf{ARA}^T + \mathbf{C})^{-1} \quad [2.3.17]$$

The Bayesian linear inverse operator derivation begins with the expression for conditional probability:

$$\Pr(\mathbf{s}|\mathbf{x}) = \frac{\Pr(\mathbf{x}|\mathbf{s})\Pr(\mathbf{s})}{\Pr(\mathbf{x})} \quad [2.3.18]$$

which one would like to maximize. Beginning with a measurement vector **x**:

$$\mathbf{x} = \mathbf{As} + \mathbf{n} \quad [2.3.19]$$

where **A** is the gain matrix, **s** is the strength of each dipole component, and **n** is the noise vector. Assuming both **n** and **s** are normally distributed with zero mean and covariance matrices **C** and **R**, respectively, rewrite $\Pr(\mathbf{x}|\mathbf{s})$ and $\Pr(\mathbf{s})$:

$$\Pr(\mathbf{x}|\mathbf{s}) = e^{-(\mathbf{As}-\mathbf{x})^T\mathbf{C}^{-1}(\mathbf{As}-\mathbf{x})} \quad [2.3.20]$$

$$\Pr(\mathbf{s}) = e^{-\mathbf{s}^T\mathbf{R}^{-1}\mathbf{s}} \quad [2.3.21]$$

This gives a simplified Bayesian expression:

$$\max[\Pr(\mathbf{s}|\mathbf{x})] = \max\left[\frac{\left(e^{-(\mathbf{As}-\mathbf{x})^T\mathbf{C}^{-1}(\mathbf{As}-\mathbf{x})}\right)\left(e^{-\mathbf{s}^T\mathbf{R}^{-1}\mathbf{s}}\right)}{\Pr(\mathbf{x})}\right] \quad [2.3.22]$$

$$= \max\left[-(\mathbf{As}-\mathbf{x})^T\mathbf{C}^{-1}(\mathbf{As}-\mathbf{x}) - \mathbf{s}^T\mathbf{R}^{-1}\mathbf{s}\right] \quad [2.3.23]$$

$$= \min\left[(\mathbf{As}-\mathbf{x})^T\mathbf{C}^{-1}(\mathbf{As}-\mathbf{x}) + \mathbf{s}^T\mathbf{R}^{-1}\mathbf{s}\right] \quad [2.3.24]$$

Taking the derivative with respect to **s** and setting it to zero:

$$2\mathbf{A}^T\mathbf{C}^{-1}\mathbf{As} - 2\mathbf{A}^T\mathbf{C}^{-1}\mathbf{x} + 2\mathbf{R}^{-1}\mathbf{s} = 0 \quad [2.3.25]$$

$$\mathbf{s} = (\mathbf{A}^T\mathbf{C}^{-1}\mathbf{A} + \mathbf{R}^{-1})^{-1}\mathbf{A}^T\mathbf{C}^{-1}\mathbf{x} = \mathbf{Wx} \quad [2.3.26]$$

which yields the expression for the Bayesian linear operator

$$\mathbf{W} = (\mathbf{A}^T\mathbf{C}^{-1}\mathbf{A} + \mathbf{R}^{-1})^{-1}\mathbf{A}^T\mathbf{C}^{-1} \quad [2.3.27]$$

This Bayesian linear operator is also very similar to the regularization method. Again, begin with a measurement vector **x**:

$$\mathbf{As} = \mathbf{x} \quad [2.3.28]$$

A smoothing functional **F** is defined as:

$$\mathbf{F} = \|\mathbf{As} - \mathbf{x}\|^2 + \lambda\mathbf{M}|\mathbf{s} - \mathbf{s}_1|^2 \quad [2.3.29]$$

where $\lambda\mathbf{M}$ is added for regularization and $\mathbf{s}_1$ is normally taken to be zero. To calculate the operator, the smoothing functional is explicitly minimized (taking its derivative and setting it to zero). Solving for **s**:

$$0 = 2\mathbf{A}^T\mathbf{As} - 2\mathbf{A}^T\mathbf{x} + 2\lambda\mathbf{Ms} \quad [2.3.30]$$

$$\left(\mathbf{A}^T\mathbf{A} + \lambda\mathbf{M}\right)\mathbf{s} = \mathbf{A}^T\mathbf{x} \quad [2.3.31]$$

$$\mathbf{s} = \left(\mathbf{A}^T\mathbf{A} + \lambda\mathbf{M}\right)^{-1}\mathbf{A}^T\mathbf{x} = \mathbf{Wx} \quad [2.3.32]$$

$$\mathbf{W} = \left(\mathbf{A}^T\mathbf{A} + \lambda\mathbf{M}\right)^{-1}\mathbf{A}^T \quad [2.3.33]$$

This is equivalent to the Bayesian linear operator when $\mathbf{C} = \mathbf{I}$ and $\lambda\mathbf{M} = \mathbf{R}^{-1}$. These particular inverse derivations are very general and allows us to express many different kinds of inverse methods. For example, LORETA (6), which imposes a smoothness constraint on the inverse solution, can be expressed in this framework if **M** is the vector laplacian.

Wiener filtering (also known as the Kalman-Bucy method) , uses an optimal linear filter to minimize the expected error between the actual source and the estimated source:

$$Err_W = \left\langle \left| \mathbf{W}\,\mathbf{x} - \hat{\mathbf{s}} \right|^2 \right\rangle \quad [2.3.34]$$

The operator must satisfy the Wiener-Hopf equation:

$$\Psi_{sx} = \mathbf{W}\Psi_x \quad [2.3.35]$$

where $\Psi_{sx} = \left\langle \mathbf{sx}^T \right\rangle$ and $\Psi_x = \left\langle \mathbf{xx}^T \right\rangle$.

Expanding the covariance terms gives:

$$\left\langle \mathbf{s}[\mathbf{As}+\mathbf{n}]^T \right\rangle = \mathbf{W}\left\langle [\mathbf{As}+\mathbf{n}][\mathbf{As}+\mathbf{n}]^T \right\rangle \quad [2.3.36]$$

$$\left\langle \mathbf{ss}^T\mathbf{A} + \mathbf{sn}^T \right\rangle = \mathbf{W}\left\langle \mathbf{Ass}^T\mathbf{A}^T + \mathbf{ns}^T\mathbf{A}^T + \mathbf{Asn} + \mathbf{nn}^T \right\rangle \quad [2.3.37]$$

$$\left\langle \mathbf{ss}^T\mathbf{A} \right\rangle + \left\langle \mathbf{sn}^T \right\rangle = \mathbf{W}\left(\left\langle \mathbf{Ass}^T\mathbf{A}^T \right\rangle + \left\langle \mathbf{ns}^T\mathbf{A}^T \right\rangle + \langle \mathbf{Asn} \rangle + \left\langle \mathbf{nn}^T \right\rangle \right) \quad [2.3.38]$$

Since the noise and signal are independent, the signal-noise covariance terms (e.g. $\left\langle \mathbf{sn}^T \right\rangle$) equal zero, leaving:

$$\left\langle \mathbf{ss}^T\mathbf{A} \right\rangle = \mathbf{W}\left(\left\langle \mathbf{Ass}^T\mathbf{A}^T \right\rangle + \left\langle \mathbf{nn}^T \right\rangle \right) \quad [2.3.39]$$

$$\mathbf{RA}^T = \mathbf{W}\left(\mathbf{ARA}^T + \mathbf{C}\right) \quad [2.3.40]$$

Again, the inverse operator is:

$$\mathbf{W} = \mathbf{RA}^T\left(\mathbf{ARA}^T + \mathbf{C}\right)^{-1} \quad [2.3.41]$$

One additional note regarding the Wiener filter:

A suggested improvement to Wiener estimation is to use an estimate of the signal covariance matrix and incorporate that estimate into the Wiener inverse operator (16, 17, 19). The "new" operator is:

$$\mathbf{W} = \mathbf{A}^*(\mathbf{D} - \mathbf{C})\mathbf{D}^{-1} \quad [2.3.42]$$

where $\mathbf{A}^* = \mathbf{A}^T\left(\mathbf{AA}^T\right)^{-1}$ (pseudoinverse of **A**) and $\mathbf{D} = \left\langle \mathbf{xx}^T \right\rangle = \left\langle [\mathbf{As}+\mathbf{n}][\mathbf{As}+\mathbf{n}]^T \right\rangle = \mathbf{ARA}^T + \mathbf{C}$.

Expanding:

$$\mathbf{W} = \mathbf{A}^T\left(\mathbf{AA}^T\right)^{-1}\left(\mathbf{ARA}^T + \mathbf{C} - \mathbf{C}\right)\left(\mathbf{ARA}^T + \mathbf{C}\right)^{-1} \quad [2.3.43]$$

$$= \left(\mathbf{A}^T\left(\mathbf{A}\mathbf{A}^T\right)^{-1}\mathbf{A}\right)\mathbf{R}\mathbf{A}^T\left(\mathbf{A}\mathbf{R}\mathbf{A}^T+\mathbf{C}\right)^{-1} \quad [2.3.44]$$

The first term is equal to the identity matrix, by definition of the pseudoinverse. Therefore, one again has the equivalent inverse operator:

$$\mathbf{W} = \mathbf{R}\mathbf{A}^T\left(\mathbf{A}\mathbf{R}\mathbf{A}^T+\mathbf{C}\right)^{-1} \quad [2.3.45]$$

Finally, it is possible to show that these various linear operators are equivalent (assuming that both $\left(\mathbf{A}\mathbf{R}\mathbf{A}^T+\mathbf{C}\right)$ and $\left(\mathbf{A}^T\mathbf{C}^{-1}\mathbf{A}+\mathbf{R}^{-1}\right)$ are invertible).

$$\mathbf{R}\mathbf{A}^T\left(\mathbf{A}\mathbf{R}\mathbf{A}^T+\mathbf{C}\right)^{-1} = \left(\mathbf{A}^T\mathbf{C}^{-1}\mathbf{A}+\mathbf{R}^{-1}\right)^{-1}\left(\mathbf{A}^T\mathbf{C}^{-1}\mathbf{A}+\mathbf{R}^{-1}\right)\mathbf{R}\mathbf{A}^T\left(\mathbf{A}\mathbf{R}\mathbf{A}^T+\mathbf{C}\right)^{-1} \quad [2.3.46]$$

$$= \left(\mathbf{A}^T\mathbf{C}^{-1}\mathbf{A}+\mathbf{R}^{-1}\right)^{-1}\left(\mathbf{A}^T\mathbf{C}^{-1}\mathbf{A}\mathbf{R}\mathbf{A}^T+\mathbf{A}^T\right)\left(\mathbf{A}\mathbf{R}\mathbf{A}^T+\mathbf{C}\right)^{-1} \quad [2.3.47]$$

$$= \left(\mathbf{A}^T\mathbf{C}^{-1}\mathbf{A}+\mathbf{R}^{-1}\right)^{-1}\left(\mathbf{A}^T\mathbf{C}^{-1}\right)\left(\mathbf{A}\mathbf{R}\mathbf{A}^T+\mathbf{C}\right)\left(\mathbf{A}\mathbf{R}\mathbf{A}^T+\mathbf{C}\right)^{-1} \quad [2.3.48]$$

$$= \left(\mathbf{A}^T\mathbf{C}^{-1}\mathbf{A}+\mathbf{R}^{-1}\right)^{-1}\mathbf{A}^T\mathbf{C}^{-1} \quad [2.3.49]$$

Although these two expressions are equivalent, it is computationally more efficient to use the first expression (based on the minimization of expected error) since it only requires the inversion of a matrix that is square in the number of sensors, compared to square in the number of dipoles. Typically, the number of sensors is on the order of 200, whereas the number of dipoles can easily be in the thousands.

2.4 Crosstalk Metric

The estimated source strength ($\hat{s}_i$) at each location *i* can be written as a weighted sum of the actual source strengths at all locations, plus a noise contribution. This is due to the linearity of both the forward solution and this inverse operator. More formally,

$$\hat{s}_i = \mathbf{w}_i\mathbf{x} \quad [2.4.1]$$

$$= \mathbf{w}_i\left(\tilde{\mathbf{A}}\mathbf{s}+\mathbf{n}\right) \quad [2.4.2]$$

$$= \mathbf{w}_i\left(\sum_j \tilde{\mathbf{a}}_j s_j + \mathbf{n}\right) \quad [2.4.3]$$

$$= \sum_j\left(\mathbf{w}_i\tilde{\mathbf{a}}_j\right)s_j + \mathbf{w}_i\mathbf{n} \quad [2.4.4]$$

where $\mathbf{w}_i$ is the i^{th} *row* of **W**, and $\tilde{\mathbf{a}}_j$ is the j^{th} *column* of $\tilde{\mathbf{A}}$ (i.e. the "true" lead field including orientation information at location *j*). Depending on the particular type of mis-specification being examined through model studies, **A** (used in the calculation of **W**) and $\tilde{\mathbf{A}}$ may or may not be equivalent. When determining the crosstalk metric for experimental data, **A** and $\tilde{\mathbf{A}}$ will be the same. Note that the first term in Equation 2.4.4 is the sum of the activity (s_j) at every location *j*, weighted by the scalar $\mathbf{w}_i\tilde{\mathbf{a}}_j$. The second term reflects the noise contribution to the estimated activity at location *i*.

An explicit expression for the relative sensitivity of the estimate for a given location to activity coming from other locations is desired. A "crosstalk" metric (ξ_{ij}), similar to the averaging kernel of the Backus-Gilbert method (20), is defined as follows:

$$\xi_{ij}^2 = \frac{\left|(\mathbf{W}\tilde{\mathbf{A}})_{ij}\right|^2}{\left|(\mathbf{W}\tilde{\mathbf{A}})_{ii}\right|^2} = \frac{\left|\mathbf{w}_i\tilde{\mathbf{a}}_j\right|^2}{\left|\mathbf{w}_i\tilde{\mathbf{a}}_i\right|^2} \qquad [2.4.5]$$

With Orientation Constraint

where **WA** is the resolution matrix (21-25).

By comparing Equations 2.4.4 and 2.4.5, one can see that the crosstalk metric ξ_{ij} describes the sensitivity (or weighting) of the estimate at location *i* to activity at location *j* relative to activity at location *i* . If no orientation constraint is used, the crosstalk metric is given by:

$$\xi_{ij}^2 = \frac{\sum_{p=1}^{3}\sum_{q=1}^{3}\left|(\mathbf{W}\tilde{\mathbf{A}})_{(3i+p)(3j+q)}\right|^2}{\sum_{p=1}^{3}\sum_{q=1}^{3}\left|(\mathbf{W}\tilde{\mathbf{A}})_{(3i+p)(3i+q)}\right|^2} \qquad [2.4.6]$$

Without Orientation Constraint

where $(3i+p)$ and $(3j+q)$ are indices for particular orthogonal components at the locations being examined, and p and q are used to sum over the orthogonal components at a given location. A crosstalk value of 0% means that the estimated activity at location *i* is completely insensitive to activity at location *j*. A crosstalk value of 100% means that the estimated activity at location *i* is equally sensitive to activity at locations *i* and *j*. For a particular location, the crosstalk from all other locations can be calculated.

2.5 Point Spread Metric

Closely related to the crosstalk metric is the point spread metric. The point spread for a location *i* describes the sensitivity of the estimates at other locations *j* to activity at location *i*. A location with lower point spread has a smaller spatial extent. The point spread metric (ρ) is defined as:

$$\rho_{ij}^2 = \frac{\left|(\mathbf{W}\tilde{\mathbf{A}})_{ji}\right|^2}{\left|(\mathbf{W}\tilde{\mathbf{A}})_{ii}\right|^2} = \frac{\left|\mathbf{w}_j\tilde{\mathbf{a}}_i\right|^2}{\left|\mathbf{w}_i\tilde{\mathbf{a}}_i\right|^2} \qquad [2.5.1]$$

where $\mathbf{W}\tilde{\mathbf{A}}$ is the resolution matrix. The point spread map, more commonly known as the point spread function (PSF), for a given location *i* corresponds to the *i*th column of the crosstalk matrix (**WA**). Similar to the average crosstalk map, I define the average PSF maps (**APSF**) . For each location I average the point spread between the specified location (*i*) location and all other locations (*j*) on the surface:

$$\mathbf{APSF}_i = \frac{\sum_j \rho_{ij}^2}{j} \qquad [2.5.2]$$

One can see that crosstalk and point spread are closely related. The crosstalk map and the point spread map correspond to the rows and columns, respectively, of the resolution matrix **WA**. In the linear estimation framework examined up to this point, one can show that the resolution matrix is symmetric, and therefore the crosstalk map and the PSF for a given location are equivalent. The resolution matrix is given by:

$$\mathbf{WA} = \mathbf{R}\mathbf{A}^T\left(\mathbf{A}\mathbf{R}\mathbf{A}^T + \mathbf{C}\right)^{-1}\mathbf{A} \qquad [2.5.3]$$

The transpose of the resolution matrix is:

$$(\mathbf{WA})^T = \left(\mathbf{RA}^T\left(\mathbf{ARA}^T + \mathbf{C}\right)^{-1}\mathbf{A}\right)^T \quad [2.5.4]$$

$$= \mathbf{A}^T\left(\left(\mathbf{ARA}^T + \mathbf{C}\right)^{-1}\right)^T \mathbf{AR}^T \quad [2.5.5]$$

The term inside the parentheses is also symmetric (since the noise covariance matrix, **C**, is symmetric):

$$\left(\mathbf{ARA}^T + \mathbf{C}\right)^T = \mathbf{AR}^T\mathbf{A}^T + \mathbf{C}^T = \mathbf{ARA}^T + \mathbf{C} \quad [2.5.6]$$

The source covariance matrix (**R**) is also symmetric, so one can rewrite Equation 2.5.6:

$$= \mathbf{A}^T\left(\mathbf{ARA}^T + \mathbf{C}\right)^{-1}\mathbf{AR} \quad [2.5.7]$$

Since the term, $\mathbf{A}^T\left(\mathbf{ARA}^T + \mathbf{C}\right)^{-1}\mathbf{A}$, and **R** are both symmetric:

$$\mathbf{A}^T\left(\mathbf{ARA}^T + \mathbf{C}\right)^{-1}\mathbf{AR}^T = \mathbf{RA}^T\left(\mathbf{ARA}^T + \mathbf{C}\right)^{-1}\mathbf{A} \quad [2.5.8]$$

Similar to the average crosstalk map, I define a average point spread function map. The average PSF map represents the average of the PSF at each location on the cortical surface.

The relationship between the crosstalk metric and the point spread metric can be more easily seen graphically (Figure 1). The location of interest (i.e. location *i*) is marked in green. The arrows indicate the "direction" of mis-specification, or *where* activity is mis-localized. The crosstalk metric describes the activity from other locations that is mis-localized onto the location of interest (arrows point towards location *i*). Conversely, the point spread metric describes activity that is mis-localized from location *i* (arrows point away from location *i*). In the example below, the crosstalk map and the point spread function are the same. This is due to the symmetry of the resolution matrix. In Chapter 5, I describe a noise sensitivity normalized inverse operator where the resolution matrix is no longer symmetric. Therefore, the crosstalk and point spread maps will no longer be equivalent.

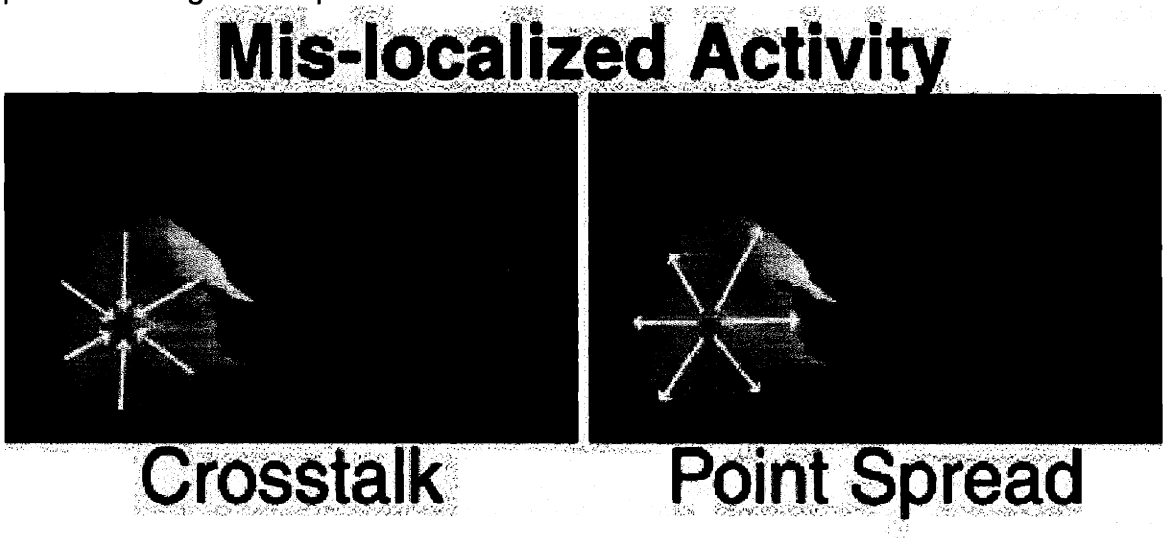

Figure 1: Mis-localized activity specified by the Crosstalk and the Point Spread metrics. The arrows indicate the "direction" of mis-specification.

Given that the crosstalk map and the point spread function are equivalent for the linear estimation operator, our discussion applies equally to both. However, various suggested improvements to the linear estimation technique will result in a non-symmetric resolution matrix. For example, the Backus-Gilbert method (20, 22, 26), which explicitly minimizes the crosstalk will result in some sort of tradeoff with the point spread function.

2.6 References

1. Plonsey R. *Bioelectric Phenomena*. New York: McGraw-Hill, 1969:
2. Nunez PL. *Electric fields of the brain*. New York: Oxford University Press, 1981:
3. Hamalainen M, Hari R, Ilmoniemi RJ, Knuutila J, and Lounasmaa OV. Magnetoencephalography - theory, instrumentation, and application to noninvasive studies of the working human brain. *Review of Modern Physics*. 1993; 65: 413-497.
4. Cuffin BN and Cohen D. Magnetic fields of a dipole in special volume conductor shapes. *IEEE Trans Biomed Eng*. 1977; 24: 372-81.
5. Dale AM and Sereno MI. Improved localization of cortical activity by combining EEG and MEG with MRI cortical surface reconstruction: A linear approach. *J. Cog. Neurosci*. 1993; 5: 162-176.
6. Pascual-Marqui RD, Michel CM, and Lehmann D. Low resolution electromagnetic tomography: a new method for localizing electrical activity in the brain. *Inter J Psychophysiology*. 1994; 18: 49-65.
7. Hamalainen MS and Ilmoniemi RJ. *Interpreting measured magnetic fields of the brain: estimates of current distributions*. Helsinki, Finland: Helsinki Univ. of Technology, 1984:
8. Dale AM. *Source Localization and Spatial Discriminant Analysis of Event-Related Potentials: Linear Approaches*. Ph.D., University of California, San Diego, 1994.
9. Hamalainen MS and Ilmoniemi RJ. Interpreting magnetic fields of the brain: minimum norm estimates. *Med Biol Eng Comput*. 1994; 32: 35-42.
10. Gelb A. *Applied Optimal Estimation*. Cambridge: MIT Press, 1974: pp. 374.
11. Phillips JW, Leahy RM, Mosher JC, and Timsari B. Imaging neural activity using MEG and EEG. *IEEE Eng Med Biol Mag*. 1997; 16: 34-42.
12. Phillips JW, Leahy RM, and Mosher JC. MEG-based imaging of focal neuronal current sources. *IEEE Trans Med Imaging*. 1997; 16: 338-48.
13. Schmidt DM, George JS, and Wood CC. Bayesian inference applied to the electromagnetic inverse problem. *Hum Brain Mapp*. 1999; 7: 195-212.
14. Tichonov AN and Arsenin VY. *Solutions of ill-posed problems*. Washington D.C.: Winston, English translation by F. John, 1977:
15. Deutsch R. *Estimation Theory*. Englewood Cliffs, NJ: Prentice Hall, 1965:
16. Smith WE. Estimation of the spatio-temporal correlations of biological electrical sources from their magnetic field. *IEEE Trans Biomed Eng*. 1992; 39: 997-1004.

17.Sekihara K and Scholz B. Average-intensity reconstruction and Wiener reconstruction of bioelectric current distribution based on its estimated covariance matrix. *IEEE Trans Biomed Eng.* 1995; 42: 149-157.
18.Sekihara K and Scholz B. Generalized Weiner estimation of three-dimensional current distribution from biomagnetic measurements. *IEEE Trans Biomed Eng.* 1996; 43: 281-291.
19.Sekihara K and Scholz B. Generalized Wiener estimation of three-dimensional current distribution from biomagnetic measurements. *IEEE Trans Biomed Eng.* 1996; 43: 281-91.
20.Backus GE and Gilbert F. Uniqueness in the inversion of inaccurate gross Earth data. *Philosophical Transactions of the Royal Society of London A.* 1970; 266: 123-192.
21.Menke W. *Geophysical Data Analysis: Discrete Inverse Theory.* San Diego, CA: Academic Press, 1989:
22.Grave de Peralta Menendez R, Gonzalez Andino S, and Lutkenhoner B. Figures of merit to compare linear distributed inverse solutions. *Brain Topography.* 1996; 9: 117-124.
23.Grave de Peralta-Menendez R, Hauk O, Andino SG, Vogt H, and Michel C. Linear inverse solutions with optimal resoluion kernels applied to electromagnetic tomography. *Human Brain Mapping.* 1997; 5: 454-467.
24.Lutkenhoner B and Grave de Peralta Menendez R. The resolution-field concept. *EEG and Clin. Neurophysiol.* 1997; 102: 326-334.
25.Grave de Peralta-Menendez R and Gonzalez-Andino SL. A critical analysis of linear inverse solutions to the neuroelectromagnetic inverse problem. *IEEE Trans Biomed Eng.* 1998; 45: 440-8.
26.Grave de Peralta Menendez R and Gonzalez Andino SL. Backus and Gilbert method for vector fields. *Hum Brain Mapp.* 1999; 7: 161-5.

3. Volumetric Model Studies

3.1. Volumetric Methods

These first model studies used a spherical head model and did not make any additional assumptions beyond the fMRI spatial constraint. Specifically, no anatomic constraint was used. These results provided an initial estimate of the potential distortion measured by the fMRI constrained linear estimation approach due to various errors in the *a priori* fMRI spatial assumptions. Although the use of a spherical head model clearly is not optimal, the goal of these particular studies is to verify the approach, not determine the accuracy of the forward computation.

A spherical head model with a radius of 10 cm and a 122 channel MEG sensor description was used (Neuromag, Helsinki, Finland). Noise was assumed to be spatially uncorrelated and white with a SNR of 10.

The three different mis-specifications were examined:
1) mis-registration - the number of areas of activation on fMRI correspond to the number of generators of magnetic fields, but the two were offset by some distance (which corresponds to a mis-registration between the MRI and MEG coordinate systems)
2) extra fMRI source - an area of fMRI activation did not generate magnetic fields
3) missing fMRI source - a generator of magnetic fields was not measured as an area of fMRI activation.

The fMRI weighting was systematically varied from no weighting (i.e. minimum norm) to complete fMRI weighting (all locations not specified by fMRI were set to 0). A depth-weighted minimum norm was also computed for comparison (1, 2). The depth-weighted minimum norm weighted each location by the inverse of the power at the detectors given a unit activation at that location.

Either 5 or 10 sources were located at random within a single octant or a single hemisphere of the head model. The single octant placement was chosen to be representative of visual studies where activity is typically concentrated in the posterior portion of the brain, whereas the single hemisphere placement was chosen to represent activity in occurring over most of the brain, as might be seen with more complex cognitive studies. Then the average crosstalk per dipole pair was computed for each type of spatial weighting (minimum norm, depth-weighted minimum norm, and fMRI constrained) and mis-specification between fMRI and actual electromagnetic source. This random placement was first repeated 100 times in the octant placement. Given the long computation time and the expectation that the octant placement would show more distortion than in the hemispheric placement (given the closer proximity of sources), thus providing a more pessimistic estimate of the expected distortion, the hemispheric studies were only repeated 10 times. The average $\pm$ standard error of the mean of the crosstalk was computed from both octant and hemispheric placements.

3.2 Volumetric Results

Shown below is the crosstalk for each of the spatial weightings (Minimum Norm, Depth-Weighted Minimum Norm, and fMRI Constrained) due to the following mis-

specifications: 1) no mis-specification between fMRI and the actual sources, 2) an extra fMRI source that is not an electromagnetic generator, 3) a missing fMRI source that is generating electromagnetic fields, and 4) a spatial mis-registration between fMRI and the actual sources. The crosstalk ± the standard error of the mean for 5 and 10 dipoles placed in a single octant are shown in Tables 3.2.1 and 3.2.2. The crosstalk _ the standard error of the mean for 5 dipoles and 10 dipoles placed in a single hemisphere are shown separately in Tables 3.2.3 and 3.2.4.

Although all values are the crosstalk metric, each column within the table describes slightly different values:
None: percentage of power that is mis-localized among locations that are correctly specified by fMRI.
Extra fMRI source: percentage of power from the correct locations that is placed on the extra fMRI source.
Missing fMRI source: percentage of power from the missing fMRI source that is placed on the locations correctly specified by fMRI.
Spatial: percentage of power that is mis-localized when there is a 1 cm spatial discrepancy

Spatial Weighings	None	Extra fMRI Source	Missing fMRI Source	Spatial (1cm)
Minimum Norm	30 ± 0.5	30 ± 1.3	29 ± 1.3	30 ± 0.5
Depth Weighted	26 ± 0.6	19 ± 1.0	26 ± 1.5	27 ± 0.6
fMRI Constrained	9 ± 0.5	8 ± 0.5	29 ± 1.4	19 ± 0.4

Table 3.2.1: 5 Dipoles in an Octant. Crosstalk (mean ± standard error of the mean). n = 100.

Spatial Weighings	None	Extra fMRI Source	Missing fMRI Source	Spatial (1cm)
Minimum Norm	31 ± 0.3	30 ± 1.1	30 ± 1.1	31 ± 0.3
Depth Weighted	27 ± 0.4	21 ± 0.9	27 ± 1.1	28 ± 0.4
fMRI Constrained	11 ± 0.3	11 ± 0.5	27 ± 1.1	20 ± 0.2

Table 3.2.2: 10 Dipoles in an Octant. Crosstalk (mean ± standard error of the mean). n = 100.

Spatial Weighings	None	Extra fMRI Source	Missing fMRI Source	Spatial (1cm)
Minimum Norm	25 ± 2.5	28 ± 5.0	28 ± 5.3	26 ± 2.5
Depth Weighted	20 ± 2.3	14 ± 1.4	21 ± 5.7	21 ± 2.3
fMRI Constrained	6 ± 1.6	6 ± 1.3	28 ± 4.8	15 ± 1.6

Table 3.2.3: 5 Dipoles in an Hemisphere. Crosstalk (mean ± standard error of the mean). n = 100.

Spatial Weighings	None	Extra fMRI Source	Missing fMRI Source	Spatial (1cm)
Minimum Norm	28 ± 1.5	28 ± 2.9	31 ± 1.8	28 ± 1.5
Depth Weighted	19 ± 1.7	17 ± 3.8	21 ± 1.9	20 ± 1.7
fMRI Constrained	9 ± 1.4	9 ± 1.4	27 ± 2.1	16 ± 1.2

Table 3.2.4: 10 Dipoles in an Hemisphere. Crosstalk (mean ± standard error of the mean). n = 100.

3.3 Volumetric Discussion

There is only a slight difference between 5 and 10 sources in the amount of crosstalk, suggesting that the number of sources will not be problematic. Also, when

the sources are placed in closer proximity (i.e. placement in one octant versus placement in a hemisphere), there is a small increase in crosstalk. More sources andsources that are closer together will both increase the crosstalk. However, the increase due to the number of sources and the proximity of sources would, on average, be small.

Regarding the various spatial constraints, minimum norm was the least successful at dealing with the various types of mis-specifications examined. The addition of a depth-dependent weighting on the minimum norm produces very little improvement (< 5% for the various metrics). However, the addition of the fMRI weighting to the minimum norm correctly localizes more of the activation, produces less crosstalk, and also places less activation on an extra fMRI source. Unfortunately, none of these various weighted minimum norm schemes handles a source that is missing from fMRI. Although the inclusion of fMRI weighting does not worsen the situation, in even the best cases a hemodynamically undetected source would still perturb the other sources by approximately 28%, on average.

3.4 References

1. Wang JZ, Williamson SJ, and Kaufman L. Magnetic source images determined by a lead-field analysis: the unique minimum-norm least-squares estimation. *IEEE Trans Biomed Eng.* 1992; 39: 665-75.

2. Hamalainen M, Hari R, Ilmoniemi RJ, Knuutila J, and Lounasmaa OV. Magnetoencephalography - theory, instrumentation, and application to noninvasive studies of the working human brain. *Review of Modern Physics.* 1993; 65: 413-497.

4. fMRI-Constrained Inverse: Surface Model Studies

4.1 Surface Methods

4.1.1 Head Model

The boundary element method (BEM) was adapted for calculating both the EEG and MEG forward solutions (1-3). Both forward solution computation requires the locations of all possible sources and the detector locations. All locations are constrained to be within the cortical surface for all model studies. Each possible source location is represented either by three orthogonal current dipoles placed at that location (without cortical orientation constraint) or a single current dipole oriented normal to the cortical surface (with cortical orientation constraint).

The computation of the MEG forward solution computation has been shown to only require the inner skull boundary to achieve an accurate solution (4-6). The EEG forward solution computation requires the specification of boundaries between brain and skull, skull and scalp, and scalp and air, and the relative conductivities of each of those regions. Given the greater difficulty in computing the EEG forward solution, these initial surface model studies only use the MEG forward solution.

The surfaces required for computation of the forward solution (cortical surface and other boundaries within the head) are automatically reconstructed from high-resolution T1-weighted 3D MR images using the technique described by (7-9). The skull is first automatically stripped off the 3D anatomical data set by inflating a stiff deformable spherical template from a starting position in the white matter. The surface expands outward until it settles exactly at the outer edge of the brain. Since bone appears dark on MR images, this outer brain surface is used to estimate the inner skull surface. The outer brain surface is also used to strip the skull from a set of slices, which would otherwise be achieved by hand-tracing each slice.

The gray/white matter boundary for each cortical hemisphere is then estimated with a region-growing method, starting from a seed point in the white matter. The gray/white matter boundary was targeted because that surface approaches itself less closely than does the pial surface. The end result is a solid block of voxels without any voids with the topology of the cortical surface. The boundary between filled and unfilled 1 x 1 x 1 mm voxels is tessellated to generate a surface that typically consists of about 150,000 vertices for each hemisphere.

The resulting surface is smoothed using a deformable template algorithm. Each vertex is moved according to the vector sum of a curvature-minimizing force and an MRI force that works to prevent each vertex from penetrating the white matter. The resulting refined surface settles near layer 4, which gives it a somewhat atrophied appearance. The cortical orientation at each location on the surface is based on this smoothed surface.

The actual surfaces determined from the MR images of a volunteer (SA) were used. The MEG detector locations used were a whole head 122 channel MEG sensor description (Neuromag, Helsinki, Finland).

4.1.2 Monte Carlo Model

To simulate fMRI areas of activation, either 5, 10, or 20 sources were randomly located on the cortical surface, each with varying volumetric extent (point source, 1 cm diameter, or 2 cm diameter). The random selection ensures no systemic location bias in these model studies. The numbers and extents of sources chosen represent experimentally realistic fMRI results. Although point sources are not physiologically realistic, they were included in our simulations in order to allow comparison with standard ECD models. The diagonal elements of **R** (the *a priori* source variance estimates $\mathbf{R}_{ii} = \sigma_i^2$) corresponding to fMRI visible areas of activation were set to 1. The *a priori* variance estimates, or "weighting", at other locations not visible by fMRI ("missing" locations) were varied between $\sigma_i = 0$, 0.01, 0.1, or 1. This corresponds to 100, 99, 90, and 0% relative fMRI weighting, respectively. The classical minimum norm solution is equivalent to a relative fMRI weighting of 0%. I made no *a priori* assumptions about source correlation. Therefore, the off-diagonal elements of **R** were set to zero, i.e. $\mathbf{R}_{ij} = 0$ for $i \neq j$. It should be noted that this does not force the sources to be uncorrelated or orthogonal in time. Noise was assumed to be additive, Gaussian, uniform, and spatially uncorrelated. More precisely, $\mathbf{C} = \mathbf{I}\frac{\mathrm{tr}(\mathbf{ARA}^T)/n}{\mathrm{SNR}^2}$, where **I** is the identity matrix, tr is the trace of a square matrix, SNR is the assumed rms signal-to-noise ratio, and *n* is the number of sensors. Here, I assumed a conservative SNR of 10, which is typically observed in MEG experiments. In actual experiments, the noise is usually spatially correlated, and thus the off-diagonal elements of **C** are typically non-zero. In practice, the entire **C** matrix can be estimated from the experimental data (e.g. (10)).

In these simulations, the crosstalk metric ξ_{ij} was always calculated between fMRI visible locations *i*, and either other fMRI visible locations or fMRI invisible ("missing") locations *j*.

The random source placement was repeated 10 times and the crosstalk metrics was averaged, depending on the conditions being examined. For each random source placement, 100 missing locations were randomly selected. For comparison with our standard solution, I also calculated a lead field weighted solution (10). This is accomplished by inversely weighting each location by the sensor power generated by unit activity at that location, i.e. replacing $\mathbf{R}_{ii}$ with $\frac{\mathbf{R}_{ii}}{\|\mathbf{a}_i\|}$ in Equation 2.2.3.

4.2 Surface Results

Several studies have used fMRI or PET activation data as a prior constraint on the inverse solution. In one such approach, single equivalent current dipoles (ECDs) are placed at the center-of-mass of fMRI (11-14) or PET (15, 16) defined regions of cortical activation. A refinement of this approach uses a continuous source model (17). In the linear estimation framework presented here, these cases correspond to: setting the fMRI weighting to 100%, assuming an infinite signal-to-noise ratio, and either point or extended source models. Here, cortical areas of fMRI activation are tiled uniformly

with dipoles. By either fixing the dipole orientation (e.g., using anatomical information), or allowing the ECDs to freely rotate over time, the estimated time courses of these fMRI defined sources can then be determined using a standard pseudo inverse technique.

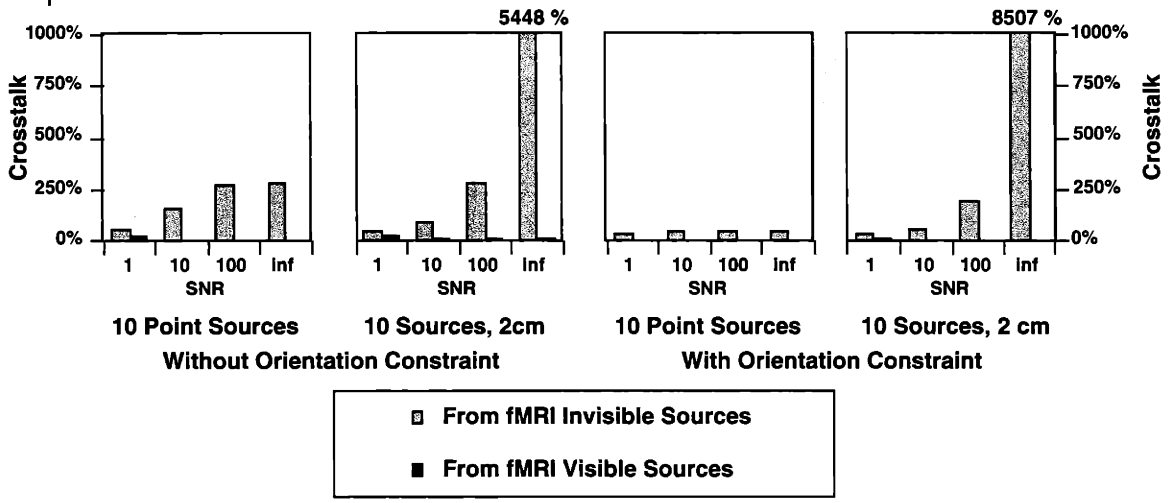

Figure 4.2.1: Crosstalk versus Noise Regularization. Crosstalk is shown for 10 sources (point and 2 cm in diameter), with and without orientation constraint. The assumed SNR was either 1, 10, 100 or infinite. A relative fMRI weighting of 100% was used. The light bars are crosstalk from fMRI invisible sources. The dark bars are crosstalk from fMRI visible sources.

The results indicate that allowing for finite signal-to-noise greatly reduces the predicted distortion from fMRI invisible sources. The extremely large amount of distortion from fMRI invisible sources when assuming infinite SNR demonstrates a potential problem with an fMRI-constrained pseudoinverse solution, which implicitly assumes infinite SNR.

Simulation studies were performed to examine the sensitivity of these proposed methods, to the potential presence of fMRI invisible (missing) sources. Figure 4.2.1 shows that the crosstalk from fMRI visible sources is quite small (< 21%), but the crosstalk from fMRI invisible sources is quite large, particularly for the extended source description. It should be noted that assuming infinite SNR is equivalent to using the Moore-Penrose pseudoinverse as the inverse operator. Importantly, the data further indicates that allowing for finite signal-to-noise greatly reduces the predicted distortion from fMRI invisible sources. However, the crosstalk remains high, and thus the presence of fMRI invisible sources could still be quite problematic.

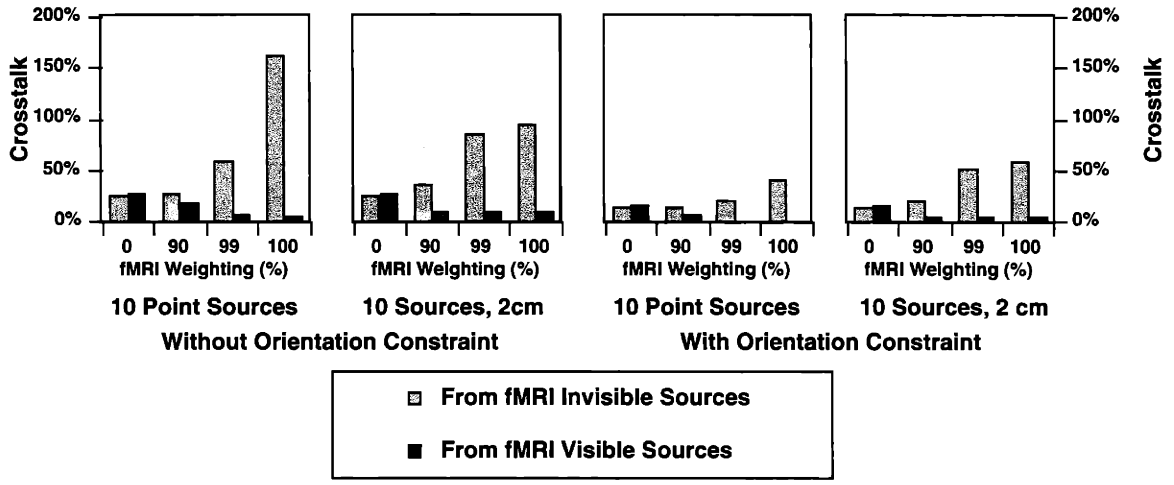

Figure 4.2.2: Crosstalk versus Relative fMRI Weighting. Crosstalk is shown for 10 sources (point and 2 cm in diameter), with and without orientation constraint. The relative fMRI weighting was either 0%, 90%, 99%, or 100%. The light bars are crosstalk from fMRI invisible sources. The dark bars are crosstalk from fMRI visible sources.

The optimal fMRI weighting requires a compromise between resolving fMRI visible sources (i.e., higher fMRI weighting) and minimizing distortion from fMRI invisible sources (i.e., lower fMRI weighting). The results indicate that a 90% fMRI weighting greatly reduces the crosstalk from fMRI visible sources, while only slightly increasing the crosstalk from fMRI invisible sources.

Based on the above results, I explored the effect of varying the degree of fMRI weighting. The crosstalk was calculated from both fMRI visible and invisible locations for varying source extent. The potential benefits of including an orientation constraint (in addition to the fMRI weighting) were also evaluated in these simulations. Figure 4.2.2 shows the results for two different source sizes - point sources (zero extent), and extended sources of 2 cm diameter. The point source (although physiologically unrealistic) is typically used in equivalent current dipole (ECD) modeling, while the 2 cm extended source is representative of the extent of contiguous activation typically observed with fMRI.

For a given fMRI visible source, Figure 4.2.2 shows that with increasing relative fMRI weighting, the crosstalk from other fMRI visible locations decreases, while the crosstalk from fMRI invisible locations increases. The use of the cortical orientation constraint reduces crosstalk from both fMRI visible and invisible sources. With no fMRI weighting (0%), crosstalk from both fMRI visible and invisible sources is identical, as would be expected. This corresponds to the well-known minimum norm solution. At this limit, a substantial crosstalk of 28% and 15% is predicted for the anatomically unconstrained and anatomically constrained cases respectively. At the other limit of 100% fMRI weighting, the crosstalk from fMRI visible sources is minimized (<8%); however, the crosstalk from fMRI invisible sources is greatly increased (>40%). Thus, unless the coupling between neuronal and hemodynamic activity is perfect, the use of 100% fMRI weighting is not optimal.

One would like to select a weighting that results in acceptably low distortion between the fMRI visible locations while achieving reasonable levels of distortion from

the fMRI invisible locations. Inspection of the results in Figure 4.2.2B and 4.2.2D (for the realistic extended source case) indicates that most of the benefit of fMRI weighting is achieved at a level of 90%. Although this weighting does not minimize the crosstalk from other visible sources, the improvement of going to 99% or even 100% fMRI weighting is small. More importantly, the data indicate that 90% fMRI weighting does not significantly increase crosstalk from invisible sources. In other words, 90% fMRI weighting is a reasonable compromise for typically-sized extended source distributions. Therefore, the remaining simulation results use 90% fMRI weighting. The general pattern of results is similar for other fMRI weightings.

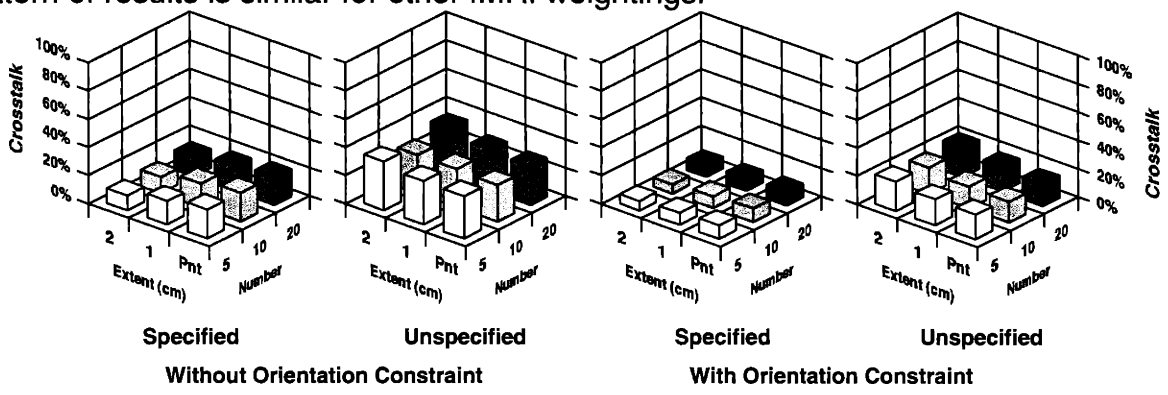

Figure 4.2.3: Crosstalk versus Extent and Number of Sources. The extent of sources was either 0 cm (point), 1 cm or 2 cm in diameter. The number of sources was 5, 10 or 20. The same colored bars all represent the same number of sources, although the extent varies for any given color. A relative fMRI weighting of 90% was used.

The results indicate that the crosstalk is relatively independent of source extent and number. This demonstrates that the proposed linear estimation method is appropriate for modelling multiple, extended areas of activation, as typically encountered in functional neuroimaging studies.

In a typical fMRI experiment, a number of discrete regions of activation are observed. Any inverse procedure that is applied to this type of data will have to handle multiple, extended source configurations. Figure 4.2.3 shows that the crosstalk from both fMRI visible and invisible sources is relatively independent of the number and the spatial extent of the sources, within the realistic range plotted. Importantly, utilizing the orientation constraint consistently results in very small crosstalk (< 10%) from the fMRI visible sources, while the crosstalk from potential fMRI invisible sources remains moderate (< 21%). This demonstrates the ability of this linear approach to cope with physiologically realistic source distributions, even in the presence of fMRI invisible (missing) sources. Obviously, since the crosstalk is substantially higher for fMRI invisible sources than for fMRI visible sources, the accuracy of the source activity estimates deteriorates with increasing neuronal activity from fMRI invisible locations.

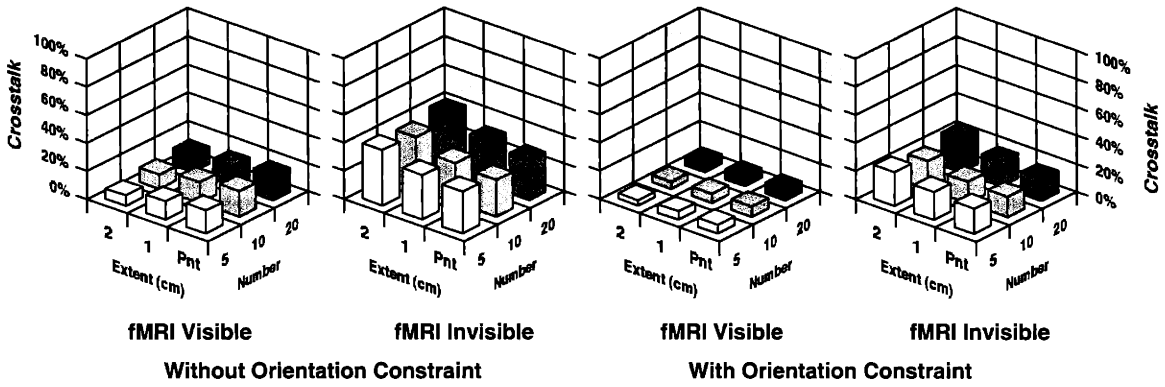

Figure 4.2.4: Crosstalk versus Extent and Number of Sources with Lead Field Weighting. The extent of sources was either 0 cm (point), 1 cm or 2 cm in diameter. The number of sources was 5, 10 or 20. The same colored bars all represent the same number of sources, although the extent varies. A relative fMRI weighting of 90% was used. These results are very similar to the non-lead field weighted inverse solution (within 2%).

Previous studies from other laboratories have suggested that lead field weighting can be used to improve the accuracy of source estimates (10, 18). The potential utility of lead field weighting in the linear estimation procedure was evaluated (Figure 4.2.4). Comparison of Figure 4.2.3 to Figure 4.2.4 shows a very similar result, although there is a small decrease (~2%) in crosstalk from fMRI visible locations and a small increase (~2%) in crosstalk from fMRI invisible locations. Given that the changes are so small and that the lead field weighting has no fundamental physiologic basis, it does not appear to be a particularly useful constraint.

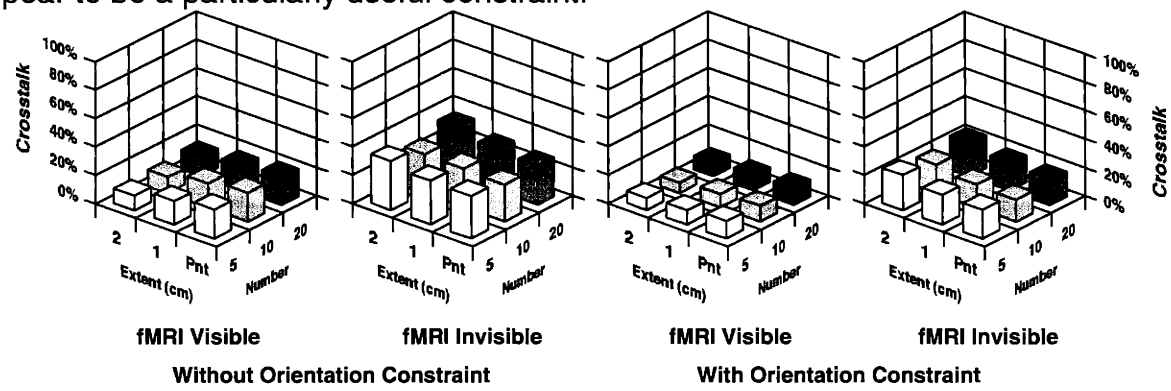

Figure 4.2.5: Crosstalk with Orientation Error versus Extent and Number of Sources. Extent of sources was either point, 1 cm or 2 cm in diameter. Number of sources was 5, 10 or 20. An orientation error of $\pm 30^{o}$ was used. A relative fMRI weighting of 90% was used.

A small increase in distortion (approximately 2%) is seen in the presence of errors in assumed source orientation. The above simulation results demonstrate that constraining activity to the cortical surface greatly reduces the predicted crosstalk from both fMRI visible and invisible sources. Obviously, the usefulness of this anatomic constraint depends upon the accuracy of the anatomic information. In general, both errors in the cortical location and its orientation will affect the solution, with orientation errors the more problematic of the two. A small change in source location will only result in small differences in the measured fields, whereas a change in orientation can

result in variations from maximally measured amplitudes to zero measured external fields. Therefore, the effect of cortical orientation errors on the accuracy of these inverse solutions was examined. Orientation errors were simulated by randomly perturbing the assumed cortical orientation or each source by $\pm 30^{o}$ about the correct orientation, a range presumably exceeding our true measurement error. Angle errors were drawn from a uniform distribution. The crosstalk metric was computed to provide a quantitative measure of our sensitivity to orientation error (Figure 4.2.5). Comparison of the crosstalk values in Figure 4.2.6 to those in Figure 4.2.3, reveals very little difference, with only a slight increase in distortion ($\approx$ 2%). Thus, orientation errors within this range would not significantly affect the accuracy of localization.

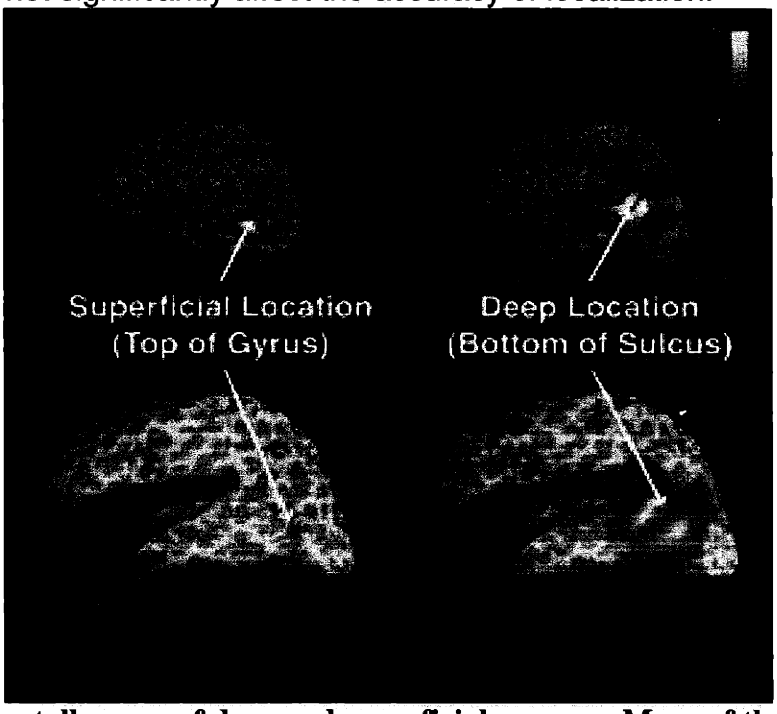

Figure 4.2.6: Crosstalk maps of deep and superficial sources. Maps of the crosstalk metric (ξ_{ij}) for two different locations *i* (see arrows) were computed for all locations *j*, shown in folded (top) and inflated (bottom) cortical surface views. Surface curvature is represented in grayscale (light and dark gray corresponding to gyri and sulci, respectively).

The crosstalk represents the relative sensitivity of the dipole strength estimate at a given location to activity at other locations (shown in color, ranging from 0 (gray), to 10 (yellow)). Note the greater spread of the crosstalk for the deep location (right) relative to the superficial location (left), reflecting different intrinsic spatial resolution for these locations, when only anatomical constraints are used.

All cortical locations may potentially contribute to the estimated activity at any given location (see Equation 2.4.4). The maps shown in Figure 4.2.6 indicate the relative weighting of activity of each and every location in the estimated activity at the indicated locations (white arrow). These crosstalk maps were calculated using the cortical location constraint and no fMRI constraint (equivalent to 0% relative fMRI weighting). The superficial location on top of the gyrus (left figures) clearly shows much less sensitivity to activity at other locations, and consequently intrinsically higher spatial

resolution, than the deeper location at the bottom of the nearby sulcus (right figures). The example further suggests that deep sources potentially benefit most from the additional inclusion of the fMRI constraint.

This type of spatial crosstalk information can show which regions of the brain are intrinsically less sensitive to localization error. In addition, such crosstalk maps can directly address the issue of mis-localized activity between two or more areas of fMRI activation. If there is little overlap between the crosstalk maps of those areas, one can be confident that the localization at one area is unaffected by activity at the other area. Conversely, if the spatial crosstalk map of one region of fMRI activity encompasses another region of fMRI activity, this particular method would not be able to accurately separate the activity from those two areas. Individual crosstalk maps can potentially be used to place some confidence limits on the interpretation of the estimated time-courses.

4.3 Surface Discussion

These simulation results demonstrate that the use of anatomic and functional MRI information can significantly improve the accuracy of our temporal estimates of dynamic human brain activity. In the ideal case, where all neuronal source activity is accurately detected by fMRI (no "missing" or "fMRI invisible" sources), the properly fMRI weighted and noise regularized linear inverse produces source timecourse estimates that should accurately reflect the true neuronal activity within the cortex. Happily, this holds true even for multiple and extended sources, as is typically encountered in human fMRI data. Additionally, the simulations demonstrate that the use of an orientation constraint consistently improves the accuracy of our source estimates. Perhaps surprisingly, errors in the specified cortical orientation, over a rather large range (encompassing any realistic error), produce very little distortion in our estimates.

These data indicate that a fMRI weighting of approximately 90% is a reasonable compromise between sensitivity to crosstalk from fMRI visible and invisible sources. The optimal fMRI weighting depends on the confidence in the hypothesis that neuronal and hemodynamic activity are tightly coupled. However, even if this hypothesis is strictly correct, the hemodynamic response caused by a given neuronal source may be too small to be detected, given finite fMRI signal-to-noise. Therefore, some intermediate level of fMRI weighting is required to properly account for potential fMRI invisible sources.

In addition, EEG/MEG averaged data always contain some finite residual noise due to spontaneous brain activity (i.e., activity not time-locked to the stimulus). It is therefore essential to allow for a finite amount of additive noise. Sensitivity to such noise can be minimized by its proper estimation and inclusion within the noise covariance matrix **C** in the linear inverse operator. As shown above in Figure 4.2.1, decreasing the assumed EEG/MEG SNR (in the **C** matrix) also has the effect of reducing the effect of missing sources. However, such modelling errors are more properly accounted for by judicious fMRI weighting (in the **R** matrix). Experimentally, the **C** matrix can and should be computed from the actual EEG/MEG measurement data.

Given proper fMRI weighting and noise regularization, the distortion between fMRI visible locations is quite small, and is further reduced by incorporating an orientation constraint. Extra fMRI sources do not result in additional crosstalk at other fMRI visible locations, since the crosstalk from fMRI visible sources has little dependence on the number of sources. In comparison, fMRI invisible sources (electromagnetic generators which do not appear by fMRI) are still problematic. However, it may be possible to detect the presence of such missing sources and other mis-specifications in the model.

4.4 References

1. Barnard ACL, Duck IM, Lynn MS, and Timlake WP. The application of electromagnetic field theory to electrocardiography - II: Numerical solution of the integral equations. *Biophys.* 1967; 7: 463-491.
2. de Munck JC. A linear discretization of the volume conductor boundary integral equation using analytically integrated elements. *IEEE Trans. Biomed. Eng.* 1992; 39: 986-990.
3. Oostendorp TF and van Oosterom A. Source parameter estimation using realistic geometry in bioelectricity and biomagnetism. In: Nenonen J, Rajala HM, and Katila T, eds. *Biomagnetic Localization and 3D Modeling, Report TKK-F-A689.* Helsinki: Helsinki University of Technology, 1992:
4. Meijs JWH, Bosch FGC, Peters MJ, and Lopes da Silva FH. On the magnetic field distribution generated by a dipolar current source situated in a realistically shaped compartment model of the head. *Electroenceph. Clin. Neurophysiol.* 1987; 66: 286-298.
5. Meijs JW, Weier OW, Peters MJ, and van Oosterom A. On the numerical accuracy of the boundary element method. *IEEE Trans Biomed Eng.* 1989; 36: 1038-49.
6. Hamalainen MS and Sarvas J. Realistic conductivity geometry model of the human head for interpretation of neuromagnetic data. *IEEE Trans. Biomed. Eng.* 1989; 36: 165-171.
7. Dale AM and Sereno MI. Improved localization of cortical activity by combining EEG and MEG with MRI cortical surface reconstruction: A linear approach. *J. Cog. Neurosci.* 1993; 5: 162-176.
8. Fischl B, Sereno MI, and Dale AM. Cortical Surface-Based Analysis II: Inflation, Flattening, a Surface-Based Coordinate System. *NeuroImage.* 1999; 9: 195-207.
9. Dale AM, Fischl B, and Sereno MI. Cortical Surface-Based Analysis I: Segmentation and Surface Reconstruction. *NeuroImage.* 1999; 9: 179-194.
10. Hamalainen M, Hari R, Ilmoniemi RJ, Knuutila J, and Lounasmaa OV. Magnetoencephalography - theory, instrumentation, and application to noninvasive studies of the working human brain. *Review of Modern Physics.* 1993; 65: 413-497.
11. Belliveau JW. MRI techniques for functional mapping of the human brain: integration with PET, EEG/MEG and infrared spectroscopy. In: Uemura K, Lassen NA, Jones T, and Kanno I, eds. *Quantification of Brain Function. Tracer Kinetics and Image Analysis in Brain PET.* Amsterdam: Elsevier Science Publishers, 1993: 639-667.

12.Ahlfors SP, Simpson GV, Dale AM, Belliveau JW, Liu AK, Korvenoja A, Virtanen J, Huotilainen M, Tootell RB, Aronen HJ, and Ilmoniemi RJ. Spatiotemporal activity of a cortical network for processing visual motion revealed by MEG and fMRI. *J Neurophysiol.* 1999; 82: 2545-55.
13.Korvenoja A, Huttunen J, Salli E, Pohjonen H, Martinkauppi S, Palva JM, Lauronen L, Virtanen J, Ilmoniemi RJ, and Aronen HJ. Activation of multiple cortical areas in response to somatosensory stimulation: combined magnetoencephalographic and functional magnetic resonance imaging. *Hum Brain Mapp.* 1999; 8: 13-27.
14.Opitz B, Mecklinger A, Von Cramon DY, and Kruggel F. Combining electrophysiological and hemodynamic measures of the auditory oddball. *Psychophysiology.* 1999; 36: 142-7.
15.Heinze HJ, Mangun GR, Burchert W, Hinrichs H, Scholz M, Munte TF, Gos A, Scherg M, Johannes S, Hundeshagen H, and et al. Combined spatial and temporal imaging of brain activity during visual selective attention in humans. *Nature.* 1994; 372: 543-546.
16.Snyder AZ, Abdullaev YG, Posner MI, and Raichle ME. Scalp electrical potentials reflect regional cerebral blood flow responses during processing of written words. *PNAS.* 1995; 92: 1689-1693.
17.George JS, Aine CJ, Mosher JC, Schmidt DM, Ranken DM, Schlitt HA, Wood CC, Lewine JD, Sanders JA, and Belliveau JW. Mapping function in the human brain with MEG, anatomical MRI and functional MRI. *J. Clin. Neurophysiology.* 1995; 12: 406-431.
18.Wang J-Z, Williamson SJ, and Kaufman L. Magnetic source images determined by a lead-field analysis: the unique minimum-norm least-squares estimation. *IEEE Trans.Biomed.Eng.* 1992; 39: 665-675.

5. Model Studies of EEG/MEG Sensor Number

5.1 Abstract

Both electroencephalography (EEG) and magnetoencephalography (MEG) are now used to localize brain activity. But, there has been some controversy regarding the relative accuracy of those two techniques. This paper theoretically compares the use of EEG, MEG, and combined EEG/MEG data sets for source localization. In general, the accuracy of localization depends on the accuracy of the particular inverse procedure utilized, which implicitly incorporates the forward solution as well. In this case, I continue the use of a linear estimation approach with distributed source model and evaluate its accuracy using the concepts of a crosstalk and point spread metrics. The crosstalk metric for a specified location on the cortex describes the amount of activity incorrectly localized onto that location from other locations. The point spread metric provides the complementary measure: for that same location, the point spread describes the mis-localization of activity from that specified location to other locations in the brain. I also examine the concept of a "noise sensitivity normalized" inverse operator. Our results show that 1) surprisingly, EEG localization is more accurate than MEG localization for the same number of sensors averaged over many source locations and orientations, 2) as expected, combining EEG with MEG produces the best accuracy for the same total number of sensors, and 3) the noise sensitivity operator improves the spatial resolution relative to the standard linear estimation operator.

5.2 Introduction

The electromagnetic inverse problem for the human brain is to determine the neural source distribution that gives rise to external electromagnetic measurements, i.e., electroencephalography (EEG) and magnetoencephalography (MEG). But, there has been some debate over the relative accuracy of EEG or MEG based source localization. The controversy began with early experimental EEG studies using phantoms (1) and implanted electrodes in epilepsy patients (2, 3). Those studies reported localization accuracy of 10 mm for the phantoms to 20 mm in the patients. In comparison, MEG studies reported localization accuracy of 3 mm in spherical phantoms (4-7) and 4 – 8 mm for skull phantoms (4, 5, 7, 8). Based on these results, it was commonly assumed that MEG localization accuracy was far superior to EEG.

However, there were theoretical reason to believe that the MEG and EEG accuracy should be comparable. In an attempt to directly address this controversy, both MEG and EEG measurements were made while generating current dipoles from implanted electrodes in an epilepsy patient (9). A sinusoidal stimulus waveform was used to remove the spike artifacts that likely contributed to the poor EEG localization performance of the previous EEG measurements (2, 3). The average MEG and EEG localization errors for dipoles with sufficiently good signal to noise were found to be 8 mm and 10 mm, respectively. These results suggested that MEG and EEG provide comparable accuracy.

Unfortunately, more recent experimental data have not necessarily clarified this issue of relative accuracy. Phantom studies have reported localization accuracy for EEG of 7 – 8 mm (10) and for MEG of 2 – 4 mm (10-12). The localization superiority of MEG over EEG is less obvious in data from measurements made in patients. Using data generated from artificial current dipoles implanted in epilepsy patients the localization accuracy of EEG was 10 - 17 mm (13-15) with the best EEG accuracy in one patient of 1 – 4 mm (14). This is compared to a localization accuracy of 17 mm for MEG measurements of artificial dipoles generated from implanted subdural strips (16). Other studies have estimated accuracy by comparing lesion data (e.g. tumor, epileptogenic focus) in epileptic patients with the non-invasive location estimates from EEG (17-21) or MEG (19-27). Similar to the results of the artificial current dipoles, the EEG and MEG accuracy were comparable (ranging from 10 – 20 mm).

Generally, in these experimental studies, it is difficult to separate the effect of errors in the head model from localization errors due to differences between EEG and MEG. Specifically, there are fundamental differences between the forward solution accuracy required by EEG and MEG, with MEG requiring a simpler model (28-30). Therefore, one would expect better accuracy for the more accurate MEG head model. It is possible to use modelling studies to examine the relative accuracy of EEG and MEG by using the same forward solution to generate both the synthetic external EEG/MEG measurements and the resulting inverse solution. In other words, modelling studies can examine EEG and MEG localization accuracy unbiased by possible inaccuracies in the forward model that may differentially affect localization of experimental EEG or MEG measurements. However, even the modelling studies have been equivocal. Some modelling work found MEG to be more accurate than EEG (31, 32), while others found EEG and MEG accuracy to be comparable (33) or EEG accuracy better than MEG (34, 35).

Clearly, the data from phantoms, patients and theoretical studies gives conflicting evidence for the relative accuracy of EEG and MEG. However, there are numerous confounding factors in the interpretation of all this data. For example, experimental measurements in phantoms and living human heads may reflect the higher accuracy of the MEG forward solution, measurement errors, or differences in signal to noise. Also, the modelling studies used spherical head models with differences between EEG and MEG sensor sampling. Here I attempt to address these limitations using a linear estimation technique with a distributed source model. I used a realistic head model and similar EEG and MEG sensor placement. In addition, I present a noise sensitivity normalized inverse operator that is based on the linear estimation approach. Monte Carlo modelling studies (sampling over numerous source locations and orientations) were used to determine the theoretical limits (i.e. assuming the no errors in the head model) of EEG and MEG localization. Localization estimates were computed using MEG or EEG data, both separately and combined. The effect of sensor sampling density (i.e., number of sensors) was examined.

It is difficult to characterize spatial accuracy in terms of a distance error for the linear estimation approach because of the extended nature of the localization estimates. Therefore, I quantified localization accuracy using a crosstalk metric (36)and a point

spread metric that are specified by the resolution matrix (37-41). These two metrics provide complementary accuracy information. The crosstalk metric for a specified location on the cortex describes the amount of activity incorrectly localized onto that location from other locations. The point spread metric provides the complementary measure: for that same location, the point spread describes the mis-localization of activity from that specified location to other locations in the brain. Lower crosstalk and point spread values indicate higher localization accuracy. As pointed out by numerous authors (e.g. (31, 36, 42-44)), localization accuracy is highly dependent on the location of the source. Therefore, to better approximate realistic data which can occur anywhere in the brain, our simulations use a large random sampling of source locations to provide an average estimate of localization accuracy.

5.3 Methods

5.3.1 Forward solution

The realistic boundary element method (BEM) was adapted for calculating both the EEG and MEG forward solutions (45, 46). Both forward solution computations require the locations of all possible sources, the sensor locations, and the sensor orientations (for MEG only). Each possible source location is represented by a current dipole oriented normal to the cortical surface.

The computation of the MEG forward solution has been shown to only require the inner skull boundary to achieve an accurate solution (28-30) . The EEG forward solution computation requires the specification of boundaries between brain and skull, skull and scalp, scalp and air, and the relative conductivities of each of those regions. Here I assumed conductivity ratios of 1:0.0125:1 for brain:skull:scalp (47).

The surfaces required for computation of the forward solution (cortical surface and other boundaries within the head) are automatically reconstructed from high-resolution T1-weighted 3D MRI using our previously described technique (48-50).

The various surfaces used in our calculations are shown in Figure 1. Each of the conductivity boundaries is represented by 642 vertices. Typically the cortical surface is initially tessellated with about 150,000 vertices per hemisphere. For the inverse computation, the cortical surface is decimated to approximately 3000 dipoles per hemisphere, which is roughly equivalent to 1 dipole every 10 mm along the cortical surface.

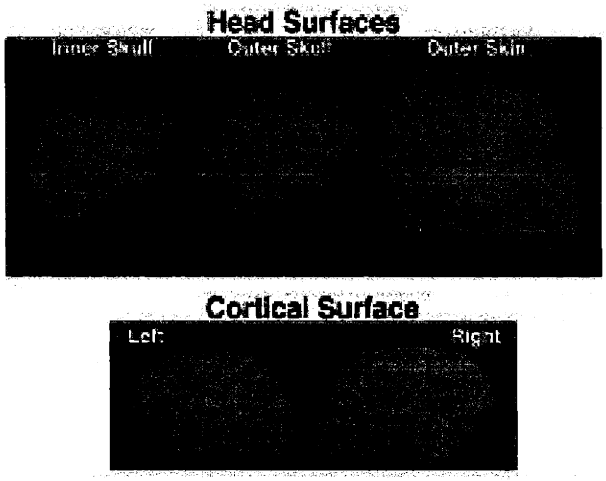

Figure 1: EEG/MEG forward solution surfaces. The top figures show the three head surfaces used in the calculation of the forward solutions. The bottom figures are the left and right cortical surfaces used to determine the locations and orientations of the sources. The MEG forward solution was computed using only the inner skull surface, whereas the EEG forward solution requires all three boundaries.

The computation of the forward solution also requires specification of the EEG electrode and/or MEG sensor locations. I began with a realistic sensor description of 122 MEG sensors (51), which is the same configuration that was used in (36). The 122 MEG sensors are placed at 61 discrete locations with two orthogonal planar gradiometers at each location. The 61 locations were subsampled to 30 locations. Both the 61 and 30 locations were distributed over the entire head. For the two sets of locations, I created three types of sensor configurations: magnetometer, radial gradiometer, and two orthogonal planar gradiometers. To minimize effects from sampling differences, the EEG sensor configurations were determined by projecting the 61 and 30 MEG locations onto the outer skin. I also examined the various combinations of MEG and EEG sensor configurations. The MEG sensor locations are shown in Figure 2, overlaid on an axial maximum intensity projection of the T1-weighted MRI. The EEG sensor locations are shown similarly in Figure 3.

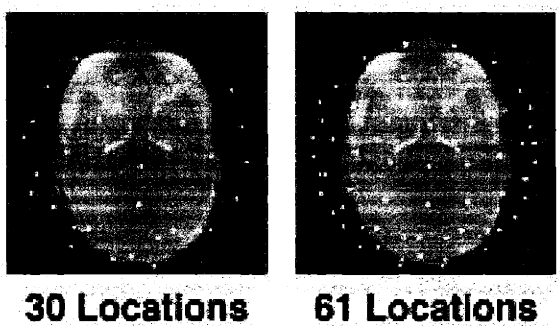

Figure 2: MEG Sensor Locations. Two different sets of locations.

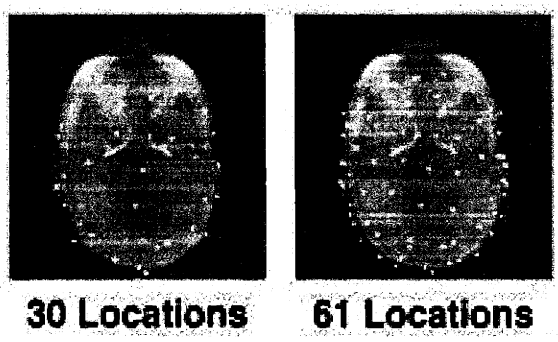

Figure 3: EEG Sensor Locations. Two different sets of locations.

For the combined EEG/MEG sensor configurations, the gain matrix (**A**) contains both the EEG and MEG forward solutions that were calculated separately. The dimensions of the combined gain matrix are [(number of EEG sensors plus number of MEG sensors) x (number of dipoles)].

5.3.2 Inverse Operator Derivations

See Chapter 2.2 "Inverse Operator" and Chapter 2.3 "Inverse Operator Derivations."

5.3.3 Crosstalk Metric

See Chapter 2.4 "Crosstalk Metric."

5.3.4 Point Spread Metric

See Chapter 2.5 "Point Spread Metric."

5.3.5 Noise sensitivity normalization

Similar to the statistical analysis of functional MRI, I am primarily interested in locations whose activity (i.e., "signal") is significantly larger than the noise. Therefore, I propose to normalize each row of the inverse operator based on the noise sensitivity of the inverse operator at that location. Locations that have low noise sensitivity are given a larger weighting that those locations with high noise sensitivity. I can estimate the noise sensitivity by projecting the noise covariance estimate into the inverse operator. The new inverse operator will be pre-multiplied by a diagonal noise sensitivity matrix (**D**), square in the number of dipoles, where each diagonal element is:

$$\mathbf{D}_{ii} = \frac{1}{\mathrm{diag}_i \sqrt{\left(\mathbf{W}\mathbf{C}\mathbf{W}^{\mathrm{T}}\right)}} \qquad 1$$

The noise sensitivity normalized inverse is now:

$$\mathbf{W}^{\mathrm{ns\_norm}} = \mathbf{D}\mathbf{W} \qquad 2$$

The resulting activity estimates will now resemble an f-statistic, instead of an activation power. Our new activity estimates, $\hat{\mathbf{s}}_i^{\mathrm{ns\_norm}}$,at each location *i*, which I refer to as "noise sensitivity normalized estimates", are:

$$\hat{\mathbf{s}}_i^{\text{ns\_norm}} = \left(\mathbf{W}^{\text{ns\_norm}}\,\mathbf{x}\right)_i = (\mathbf{DWx})_i = \sqrt{\frac{\left(\mathbf{Wxx}^{\mathrm{T}}\mathbf{W}^{\mathrm{T}}\right)_i}{\left(\mathbf{WCW}^{\mathrm{T}}\right)_i}} \qquad 3$$

For these model studies, I have assumed Gaussian, white noise, so the noise covariance matrix (**C**) is a multiple of the identity matrix. In this particular case, this noise sensitivity normalization corresponds to normalizing the rows of the inverse operator by the norm of the row:

$$\mathbf{W}_i^{\text{ns\_norm}} = \frac{\mathbf{W}_i^{\text{orig}}}{\left\|\mathbf{W}_i^{\text{orig}}\right\|} \qquad 4$$

I note that since I am scaling each row of **W** by a single value, the rows of the resolution matrix are simply scaled by that same value. Therefore the crosstalk metric remains unchanged with this noise sensitivity normalization. However, the PSF will be affected since the scaling of each column of **W** is not uniform.

5.3.6 Monte Carlo Simulations

Either 5, 10, or 20 sources were randomly located on the cortical surface, each with varying volumetric extent (1 cm or 2 cm diameter). The random selection ensures no systemic location bias in these model studies. The numbers and extents of sources were chosen to represent experimentally realistic regions of brain activity that might be seen with some cognitive task. The diagonal elements of **R** (the *a priori* source covariance estimates $\mathbf{R}_{ii} = \sigma_i^2$) were set to 1 or 0.01. These values correspond to fMRI weightings of 0% (equivalent to minimum norm) and 90%, respectively. I have previously shown that an fMRI weighting of 90% represents a reasonable compromise between separation of activity from correctly localized sources (by fMRI) and minimization of error due to missing fMRI sources (36).

I made no *a priori* assumptions about source correlation. Therefore, the off-diagonal elements of **R** were set to zero, i.e. $\mathbf{R}_{ij} = 0$ for $i \neq j$. It should be noted that this does not force the sources to be uncorrelated or orthogonal in time. Noise was assumed to be additive, Gaussian, uniform, and spatially uncorrelated. More precisely, $\mathbf{C} = \mathbf{I}\frac{\mathrm{tr}\left(\mathbf{ARA}^{\mathrm{T}}\right)/n}{\mathrm{SNR}^2}$, where **I** is the identity matrix, tr is the trace of a square matrix, SNR is the assumed rms signal-to-noise ratio, and *n* is the number of sensors. Here, a conservative SNR of 10 was assumed.

In these model studies, the number of MEG sensors was assumed to be either 30, 60 (30 locations with two orthogonal planar gradiometers), 61 or 122 (61 locations with two orthogonal planar gradiometers), with the smaller numbers of sensors subsampled from the complete 122 channel description to still give full head coverage at a sparser sampling. For the EEG sensors, 30 or 61 sensors were distributed over the entire head. To minimize any sampling differences between MEG and EEG, the locations of the EEG sensors were based on the corresponding MEG sensor configuration projected down onto the outer skin surface. In addition, all combinations of MEG and EEG sensors were studied. For each of the sensor configurations, the crosstalk was averaged over the different number and extent of sources.

For comparison of the noise sensitivity normalized inverse, the average crosstalk map and the average PSF were computed at each source location. No fMRI weighting was used, thus removing the need for Monte Carlo simulations.

One additional set of modelling studies was performed here. In computing the EEG forward solution, conductivity ratios, not exact conductivities, of the different head regions were used. If the actual conductivities differ from the assumed conductivities, even though the conductivity ratios are correctly estimated, then the computed source activities using EEG will not be in the same units as the computed source activities using MEG. This effectively introduces a scaling factor between the EEG and MEG forward solutions (44). I modeled the effect of mis-estimating the scaling factor between EEG and MEG forward solutions (corresponding to the mis-estimate of the actual conductivities) from 0.2 to 5. The scaling factor was incorporated into the combined EEG/MEG forward solution by multiplying those rows corresponding to EEG sensors by the factor. This scaled gain matrix was used in the computation of the inverse operator. The correct gain matrix, i.e., a scaling factor of 1, was used for the crosstalk metric computation. More explicitly, if one represents the scaled forward solution by $\mathbf{A}_s$ and the true forward solution by $\tilde{\mathbf{A}}$, the crosstalk matrix is given by:

$$\mathbf{W}_s\tilde{\mathbf{A}} = \mathbf{R}\mathbf{A}_s^T\left(\mathbf{A}_s\mathbf{R}\mathbf{A}_s^T + \mathbf{C}\right)^{-1}\tilde{\mathbf{A}} \qquad 5$$

For this portion of the model studies, I assumed 30 EEG electrodes and 30 MEG radial gradiometers, and an fMRI weighting of 90%.

5.4 Results

Figures 4 and 7 show the average crosstalk versus sensor configuration. No fMRI weighting (equivalent to minimum norm) was used in Figure 4. An fMRI weighting of 90% was used in Figure 7.

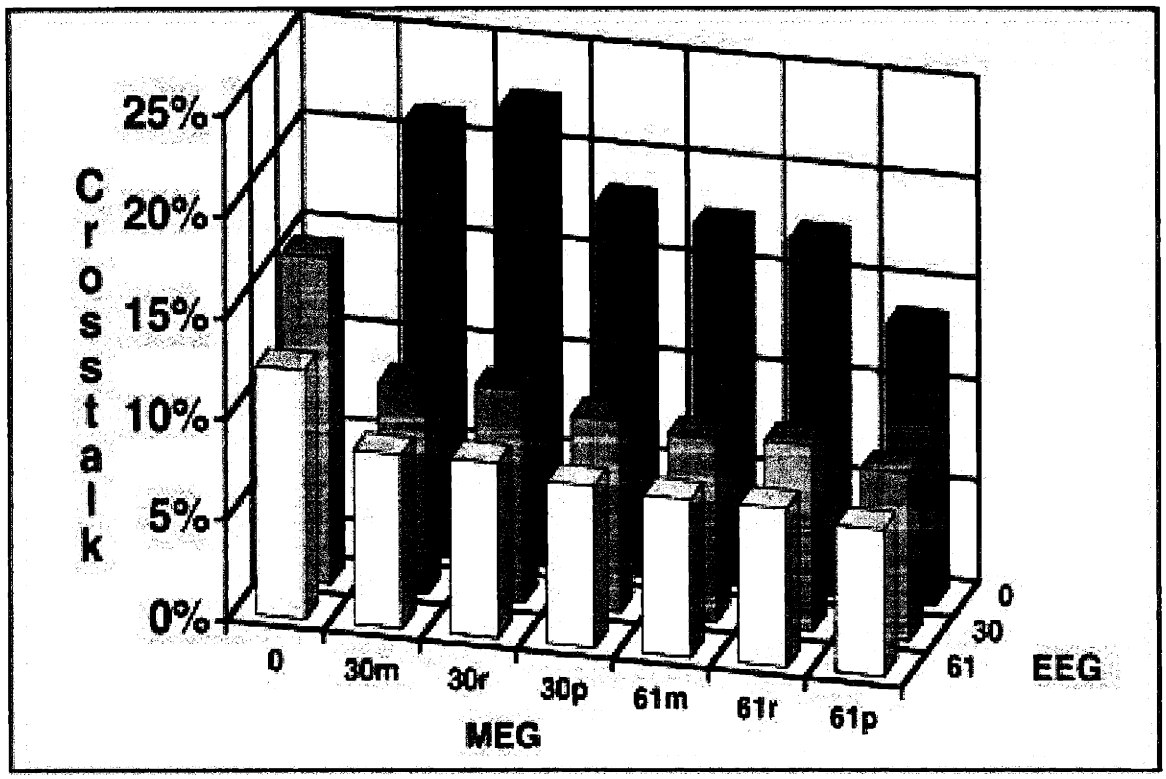

Figure 4: Average crosstalk versus sensor number - No fMRI weighting. The sensor configuration consisted of 30 magnetometers (30m), 30 radial gradiometers (30r), 60 orthogonal planar gradiometers (30p), 61 magnetometers (61m), 61 radial gradiometers (61r), 122 orthogonal planar gradiometers (61p) sensors, 30 EEG sensors , 61 EEG sensors, and all possible combinations of MEG and EEG sensors. The crosstalk values were averaged over a range of source number (5,10, or 20 sources) and extent (1 cm or 2cm in diameter).

Increasing the number of sensors for both MEG and EEG decreases the average crosstalk (i.e. improves average localization accuracy). There is little difference between equal numbers of magnetometers, radial gradiometers or planar gradiometers. The average crosstalk for the EEG configurations is better than the same number of MEG sensors. Additionally, there is a large decrease in crosstalk with the combined sensor configurations.

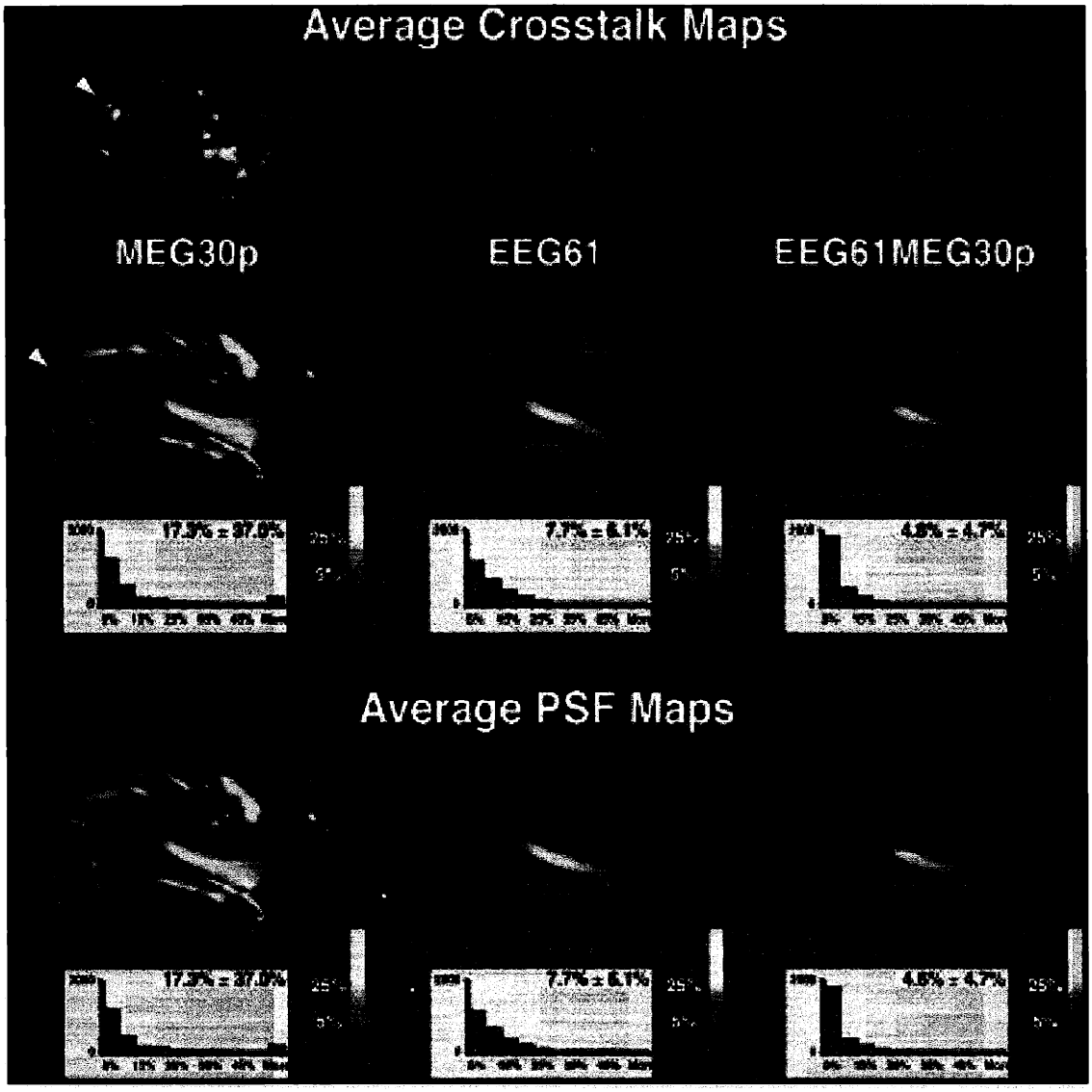

Figure 5: Average crosstalk map and average point spread function map at each location for three different sensor configurations. Below each map is the histogram of values. No fMRI weighting was used.

The average crosstalk map and average PSF map for three different sensor configurations (60 MEG planar gradiometers, 61 EEG sensors and the combined 61 EEG/ 60 MEG sensors) are shown in Figure 5. As expected, the crosstalk and PSF maps are equivalent. For the same number of sensors, EEG (7.7% ± 6.1%) has lower average crosstalk than MEG (17.3% ± 37.0%), . This difference is largely due to the very large crosstalk for MEG measurements of the deep or radial sources. The combined EEG/MEG sensor configuration provides the lowest average crosstalk. There is large spatial variability in the crosstalk map, especially for the MEG sensors. For both MEG and EEG, the crosstalk is larger in the depths of the sulci than on the gyri, with the largest crosstalks in the insula, inferior frontal and superior temporal cortex. The MEG average crosstalk maps also show the orientation dependence MEG. The locations on

the crowns of gyri that are largely radial in orientation have very high average crosstalk (e.g. see white arrow).

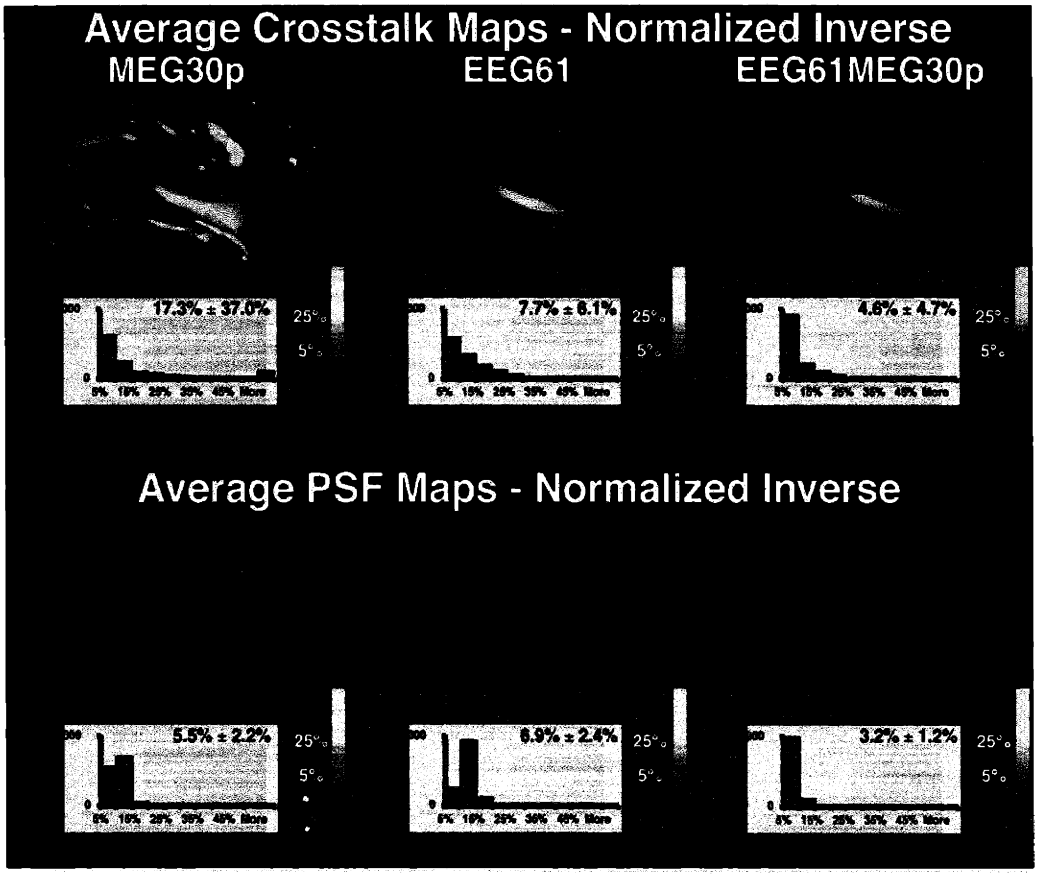

Figure 6: Average crosstalk and average PSF maps for the noise sensitivity normalized inverse operator. Below each map is the histogram of values. No fMRI weighting was used.

The average crosstalk and average PSF maps for three different sensor configurations (60 MEG planar gradiometers, 61 EEG sensors and the combined 61 EEG/ 60 MEG sensors) using the noise sensitivity normalized inverse operator are shown in Figure 6. The crosstalk maps are unchanged from Figure 5. However, the PSF maps are greatly different, especially for 60 MEG planar gradiometers only. There is greater spatial uniformity and no PSFs are greater than 20% with the noise sensitivity normalized inverse. The average PSF over all locations is lower for the normalized inverse, with the largest gain occurring for MEG sensors only (70% lower).

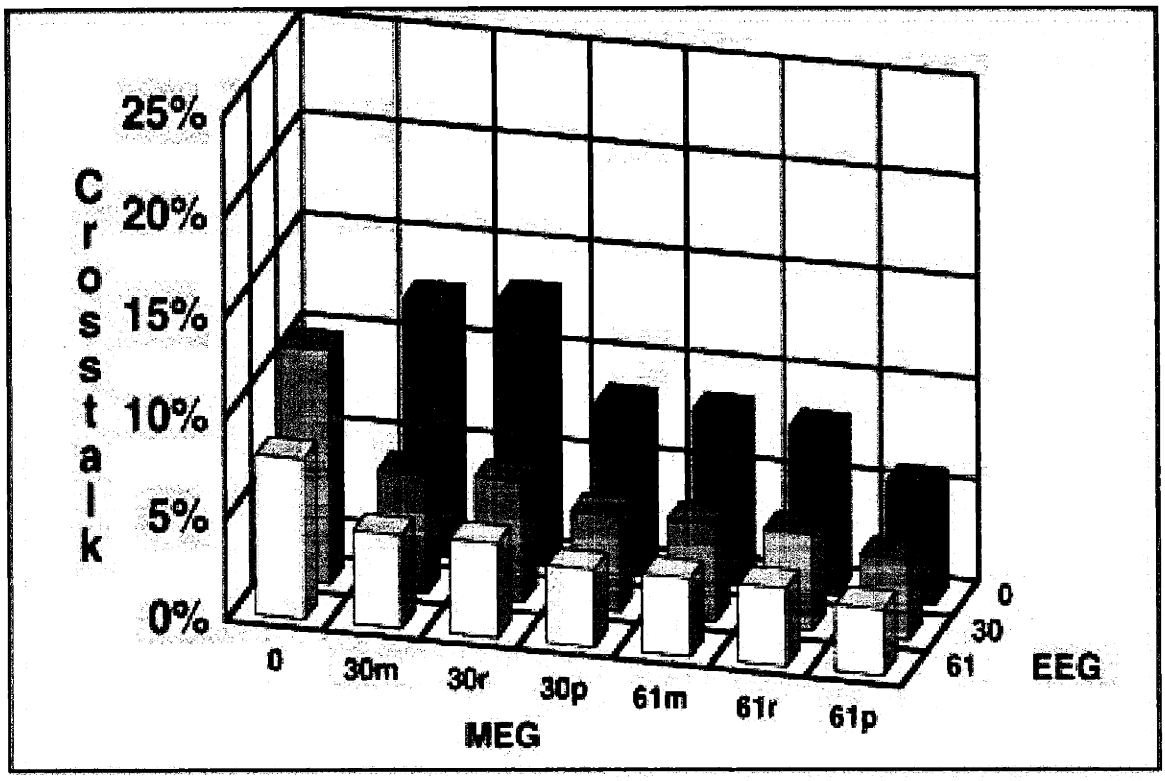

Figure 7: Average crosstalk versus sensor number - 90% fMRI weighting. The sensor configuration consisted of 30 magnetometers (30m), 30 radial gradiometers (30r), 60 orthogonal planar gradiometers (30p), 61 magnetometers (61m), 61 radial gradiometers (61r), 122 orthogonal planar gradiometers (61p) sensors, 30 EEG sensors , 61 EEG sensors, and all possible combinations of MEG and EEG sensors. The crosstalk values were averaged over a range of source number (5,10, or 20 sources) and extent (1 cm or 2cm in diameter).

The general trend of the results using fMRI weighting (Figure 7) is similar to that without fMRI weighting (Figure 4). The addition of fMRI information results in lower crosstalk for all sensor configurations. However, it should be noted that this improvement is for those sources that are correctly specified by fMRI. In cases where fMRI has mis-specified the source, crosstalk increases relative to the fMRI unweighted solution shown in Figure 4 (for a more in depth discussion, see (36). Increasing the number of sensors, regardless of the type, improves localization accuracy. The localization accuracy for the same number of sensors is only slightly better with EEG. The average crosstalk for the combined EEG and MEG sensors is lower than either EEG or MEG alone, with 61 EEG and 122 MEG (61p) sensors providing the lowest crosstalk of the different sensor configurations studied.

The observed improvement in localization accuracy obtained by combining EEG and MEG data is predicated by the assumption that one knows the proper scaling factor between the two forward solutions. If this scaling factor is unknown, additional errors can arise. Figure 8 demonstrates the effect of mis-specifying the EEG/MEG scaling factor.

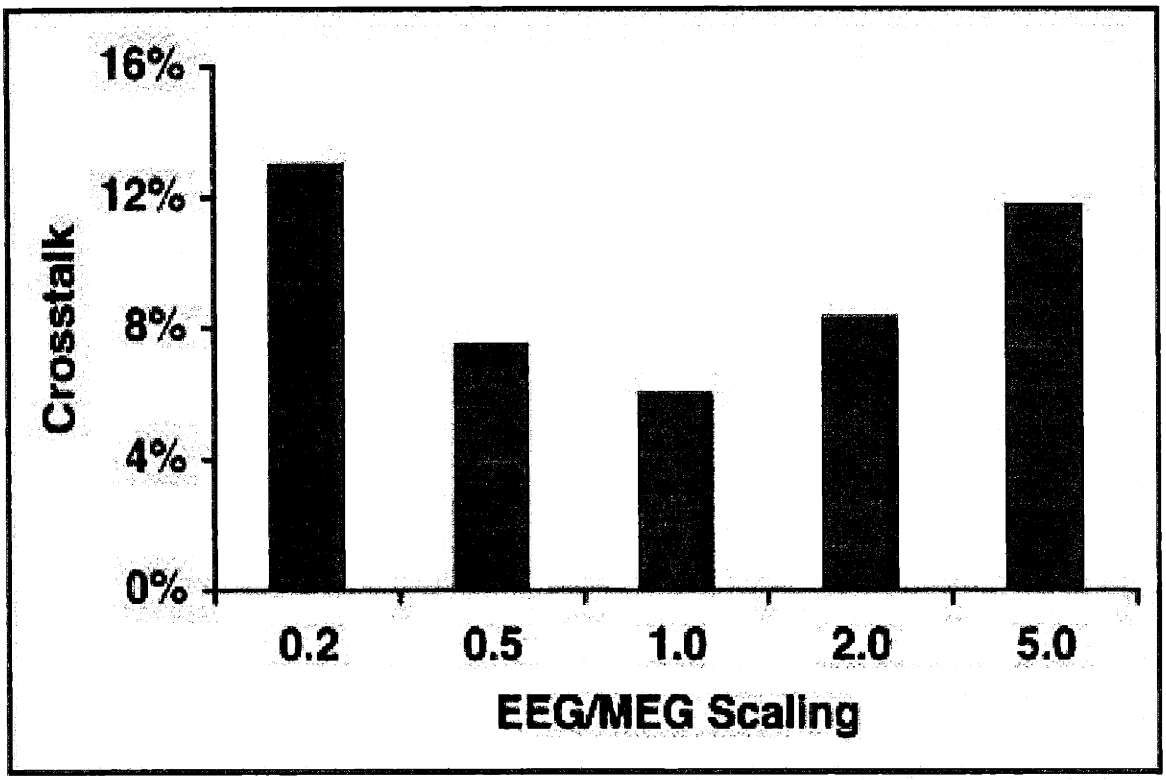

Figure 8: Average crosstalk versus EEG/MEG forward solution scaling. A sensor configuration of 30 EEG sensors and 30 MEG radial gradiometers was used. An fMRI weighting of 90% was used. The scaling factor between the EEG and MEG forward solutions was varied from 0.2 to 5. A scaling factor of 1 assumes no error in the scaling between EEG and MEG forward solutions. The crosstalk values were averaged over a range of source number (5,10, or 20 sources) and extent (1 cm or 2cm in diameter).

An increasing discrepancy between the EEG and MEG forward solution (modeled by a deviation of the EEG/MEG scaling factor from unity) results in increasingly larger average crosstalk.

5.5 Discussion

Changes in the sensor configuration produce similar results independent of the use of fMRI weighting. Not surprisingly, increasing sensor number, regardless of the type of MEG sensor, results in improved localization accuracy. Comparing MEG to EEG for the same number of sensors, one sees that, on average, EEG is superior to MEG. In fact, when using no fMRI weighting, 30 EEG sensors (16.1%) have lower average crosstalk than even 61 MEG magnetometers (17.6%) or radial gradiometers (17.4%). The superiority of EEG over MEG results from the greater depth and orientation sensitivity of MEG. For EEG sensors alone, there are no average crosstalk values greater than 40%. In comparison, for 60 MEG planar gradiometers, 12% of the average crosstalk values are greater than 40%. While, the fMRI weighting constraint reduces crosstalk for properly detected sources in all cases, the relative difference between EEG and MEG are less pronounced with fMRI weighting. When including the

fMRI constraint, the crosstalk is largely defined by the spatial priors provided by the fMRI. Subsequently, the inverse operator is less sensitive to depth and orientation.

The lowest crosstalk is achieved by combining EEG and MEG sensors. Using 61 EEG sensors and 122 MEG planar gradiometers together results in 1/3 of the average crosstalk of 30 MEG sensors alone. The largest improvements in crosstalk (a decrease of > 50% in crosstalk) are seen when going from 0 to 30 EEG sensors in addition to any number of MEG sensors. The next largest decreases in crosstalk occur with the addition of 30 MEG sensors (magnetometers or radial gradiometers) to any number of EEG sensors. Once both EEG and MEG sensors are included, there are only small decreases in crosstalk. This last result suggests an important experimental consideration. Increasing MEG sensors does not increase the setup time for the experiment, whereas the placement of numerous EEG sensors can be extremely time consuming. However, significant gains in localization accuracy can be achieved simply by placing a small number of EEG channels to be recorded simultaneously with a large number of MEG channels. Clearly a combined EEG/MEG approach is superior to using either technique independently, regardless of whether fMRI information is included. Although the forward solutions for MEG and for EEG were computed using two different models, I assumed that there were no errors in the head models. Therefore, these results are not affected by any discrepancy between the two head models.

Our results compared the average crosstalk to the average PSF over all locations. Using the standard linear estimation inverse operator, the crosstalk map and the PSF are equivalent (i.e. the resolution matrix is symmetric). In general, this equivalence will not necessarily be true. In fact, the crosstalk map and PSF reflect two different aspects of localization accuracy. The crosstalk metric for a specified location on the cortex describes the amount of activity incorrectly localized onto that location from other locations, where the point spread metric provides the complementary measure: for that same location, the point spread describes the mis-localization of activity from that specified location to other locations in the brain. If the crosstalk map for a location was a delta function, the estimate at that location would completely reflect activity at that location. If the PSF for a location was a delta function, a point source at that location would be spatially localized as a point source.

Typically, neither the crosstalk map nor the PSF would be a delta function. However, the spatial extent of these two maps can be used to determine the confidence of the estimates. If there are other active areas that overlap with the crosstalk map for a given location, the activity at that location is affected by those other areas. In that situation, the estimate for that location will not only reflect activity from that location, but will reflect a weighted sum of all the activity within the region defined by the crosstalk map. If, on the other hand, there are no other active areas within a crosstalk map, one can be confident that the estimated activity reflects the true activity. The PSF is easier to interpret than the crosstalk map. The PSF for a location defines the spatial extent of activity that would be localized for a point source at that location. Any activity in the region defined by the PSF cannot be separated from activity at the given location.

While the noise sensitivity normalized inverse has no effect on the crosstalk map, there is significant improvement in the point spread function, especially at deep and

radial sources for MEG sensors only. Therefore, one would expect to have more focal sources with similar temporal accuracy as the unnormalized inverse operator. However, there is a disadvantage to using the noise sensitivity normalized inverse operator. Since each location has a different normalization factor, direct amplitude comparisons between the timecourses of different locations cannot be made. Although, one can still make comparisons for a given location across different conditions.

Many empirical experiments are now collecting EEG and MEG data simultaneously. Both types of data are acquired in the hope of producing more accurate source localization estimates. To maximally use this combined information, the scaling factor between the two different types of data must be known. Since the EEG forward solution is calculated using conductivity ratios instead of actual conductivities, there can be a discrepancy between EEG and MEG with respect to the units of the estimated source strengths. Thus, when combining the two techniques, error is introduced when the EEG/MEG forward solution scaling factor is mis-estimated. One finds that even if the conductivity ratios are known, the actual scaling factor between EEG and MEG needs to be known within a factor of 2. If the scaling factor is mis-estimated by a factor of 0.2 (or 5), the average crosstalk is over twice as large as when the scaling factor is correctly determined.

Certain caveats apply to these results. First, to specifically evaluate the inverse procedure, I assumed that there were no errors in the EEG and MEG forward solutions. Currently, the MEG forward solution is more accurate than the EEG forward solution, owing to the fact that the MEG forward solution requires only the inner skull surface and does not depend on the conductivities of the various tissue types in the brain (28-30). If errors in the head model are included, which is likely to be the case with the currently available head models, the EEG accuracy will worsen relative to the MEG accuracy. Second, I also assumed equal signal-to-noise ratios for all sensor types measurements. In cases where the SNR differs (such as magnetometers versus radial gradiometers), localization using the modality with the best SNR will result in greater accuracy than is shown here. Finally, I did not constrain the source orientations. As discussed above, since MEG poorly localizes radial versus tangential sources, some of the measured superiority of EEG is due to this orientation dependence of MEG.

Recently, other simulations examining the combination of EEG and MEG measurements were presented (44). Fuchs et al. used a single equivalent current dipole (ECD) inverse approach to localize test dipoles in a spherical three-shell head model. Because these authors used both a different forward model and inverse method, our results are not directly comparable. However, similar results were obtained with respect to two findings: 1) increasing sensor number decreases localization errors and 2) a combination of EEG and MEG is better than either modality alone.

Overall, these results demonstrate that both EEG and MEG are useful technologies for the localization of brain activity. The lowest crosstalk, and hence the highest temporal accuracy, was achieved by combining EEG and MEG data, providing motivation for further development of both methodologies. A large reduction in the PSF, i.e. increase in spatial accuracy, was provided by using the noise sensitivity normalized inverse operator. More accurate head models will improve localization accuracy, but

will not eliminate the need for the acquisition of simultaneous EEG and MEG information.

5.6 References

1. Henderson CJ, Butler SR, and Glass A. The localization of equivalent dipoles of EEG sources by the application of electrical field theory. *Electroencephalogr Clin Neurophysiol.* 1975; 39: 117-30.
2. Smith DB, Sidman RD, Flanigin H, Henke J, and Labiner D. A reliable method for localizing deep intracranial sources of the EEG. *Neurology.* 1985; 35: 1702-7.
3. Smith DB, Sidman RD, Henke JS, Flanigin H, Labiner D, and Evans CN. Scalp and depth recordings of induced deep cerebral potentials. *Electroencephalogr Clin Neurophysiol.* 1983; 55: 145-50.
4. Barth DS, Sutherling W, Broffman J, and Beatty J. Magnetic localization of a dipole current source implanted in a sphere and in a human cranium. *Electroenceph. Clin. Neurophysiol.* 1986; 63: 260-273.
5. Janday BS and Swithenby SJ. Analysis of magnetoencephalographic data using the homogeneous sphere model: empirical tests. *Phys Med Biol.* 1987; 32: 105-13.
6. Hansen JS, Ko HW, Fisher RS, and Litt B. Practical limits on the biomagnetic inverse process determined from in vitro measurements in spherical conducting volumes. *Phys Med Biol.* 1988; 33: 105-11.
7. Yamamoto T, Williamson SJ, Kaufman L, Nicholson C, and Llinas R. Magnetic localization of neuronal activity in the human brain. *Proc Natl Acad Sci U S A.* 1988; 85: 8732-8736.
8. Weinberger H, Brickett P, Coolsma F, and Baff M. Magnetic Localisation of Intracranial Dipoles: Simulation with a Physical Model. *Electroenceph. Clin. Neuophysiol.* 1986; 64: 159-170.
9. Cohen D, Cuffin BN, Yunokuchi K, Maniewski R, Purcell C, Cosgrove GR, Ives J, Kennedy JG, and Schomer DL. MEG versus EEG localization test using implanted sources in the human brain. *Ann Neurol.* 1990; 28: 811-817.
10. Leahy RM, Mosher JC, Spencer ME, Huang MX, and Lewine JD. A study of dipole localization accuracy for MEG and EEG using a human skull phantom. *Electroencephalogr Clin Neurophysiol.* 1998; 107: 159-73.
11. Menninghaus E, Lutkenhoner B, and Gonzalez SL. Localization of a dipolar source in a skull phantom: realistic versus spherical model. *IEEE Trans Biomed Eng.* 1994; 41: 986-9.
12. Gharib S, Sutherling WW, Nakasato N, Barth DS, Baumgartner C, Alexopoulos N, Taylor S, and Rogers RL. MEG and ECoG localization accuracy test. *Electroencephalography and clinical Neurophysiology.* 1995; 94: 109-114.
13. Cuffin BN, Cohen D, Yunokuchi K, Maniewski R, Purcell C, Cosgrove GR, Ives J, Kennedy J, and Schomer D. Tests of EEG localization accuracy using implanted sources in the human brain. *Ann Neurol.* 1991; 29: 132-8.
14. Cuffin BN. EEG localization accuracy improvements using realistically shaped head models. *IEEE Trans Biomed Eng.* 1996; 43: 299-303.

15.Krings T, Chiappa KH, Cuffin BN, Cochius JI, Connolly S, and Cosgrove GR. Accuracy of EEG dipole source localization using implanted sources in the human brain. *Clin Neurophysiol.* 1999; 110: 106-14.
16.Balish M, Sato S, Connaughton P, and Kufta C. Localization of implanted dipoles by magnetoencephalography. *Neurology.* 1991; 41: 1072-6.
17.Herrendorf G, B.J. S, Kolle R, Baudewig J, Waberski TD, Buchner H, and Paulus W. Dipole-source analysis in a realistic head model in patients with focal epilepsy. *Epilepsia.* 2000; 41: 71-80.
18.Krings T, Chiappa KH, Cuffin BN, Buchbinder BR, and Cosgrove GR. Accuracy of electroencephalographic dipole localization of epileptiform activities associated with focal brain lesions. *Ann Neurol.* 1998; 44: 76-86.
19.Nakasato N, Levesque MF, Barth DS, Baumgartner C, Rogers RL, and Sutherling WW. Comparisons of MEG, EEG, and ECoG source localization in neocortical partial epilepsy in humans. *Electroencephalogr Clin Neurophysiol.* 1994; 91: 171-8.
20.Ko DY, Kufta C, Scaffidi D, and Sato S. Source localization determined by magnetoencephalography and electroencephalography in temporal lobe epilepsy: comparison with electrocorticography: technical case report. *Neurosurgery.* 1998; 42: 414-21; discussion 421-2.
21.Diekmann V, Becker W, Jurgens R, Grozinger B, Kleiser B, Richter HP, and Wollinsky KH. Localisation of epileptic foci with electric, magnetic and combined electromagnetic models. *Electroencephalogr Clin Neurophysiol.* 1998; 106: 297-313.
22.Sutherling WW, Crandall PH, Darcey TM, Becker DP, Levesque MF, and Barth DS. The magnetic and electric fields agree with intracranial localizations of somatosensory cortex. *Neurology.* 1988; 38: 1705-14.
23.Sutherling WW, Crandall PH, Engel J, Jr., Darcey TM, Cahan LD, and Barth DS. The magnetic field of complex partial seizures agrees with intracranial localizations. *Ann Neurol.* 1987; 21: 548-58.
24.Sutherling WW, Crandall PH, Cahan LD, and Barth DS. The magnetic field of epileptic spikes agrees with intracranial localizations in complex partial epilepsy. *Neurology.* 1988; 38: 778-86.
25.Stefan H, Schuler P, Abraham-Fuchs K, Schneider S, Gebhardt M, Neubauer U, Hummel C, Huk WJ, and Thierauf P. Magnetic source localization and morphological changes in temporal lobe epilepsy: comparison of MEG/EEG, ECoG and volumetric MRI in presurgical evaluation of operated patients. *Acta Neurol Scand Suppl.* 1994; 152: 83-8.
26.Mikuni N, Nagamine T, Ikeda A, Terada K, Taki W, Kimura J, Kikuchi H, and Shibasaki H. Simultaneous recording of epileptiform discharges by MEG and subdural electrodes in temporal lobe epilepsy. *Neuroimage.* 1997; 5: 298-306.
27.Tiihonen J, Hari R, Kajola M, Nousiainen U, and Vapalahti M. Localization of epileptic foci using a large-area magnetometer and functional brain anatomy [see comments]. *Ann Neurol.* 1990; 27: 283-90.
28.Meijs JWH, Bosch FGC, Peters MJ, and Lopes da Silva FH. On the magnetic field distribution generated by a dipolar current source situated in a realistically shaped

compartment model of the head. *Electroenceph. Clin. Neurophysiol.* 1987; 66: 286-298.
29. Hamalainen MS and Sarvas J. Realistic conductivity geometry model of the human head for interpretation of neuromagnetic data. *IEEE Trans. Biomed. Eng.* 1989; 36: 165-171.
30. Meijs JWH, Weier OW, Peters MJ, and Van Oosterom A. On the numerical accuracy of the boundary element method. *IEEE Trans.Biomed.Eng.* 1989; 36: 1038-1049.
31. Murro AM, Smith JR, King DW, and Park YD. Precision of dipole localization in a spherical volume conductor: a comparison of referential EEG, magnetoencephalography and scalp current density methods. *Brain Topogr.* 1995; 8: 119-25.
32. Stok CJ. The influence of model parameters on EEG/MEG single dipole source estimation. *IEEE Trans Biomed Eng.* 1987; 34: 289-96.
33. Malmivuo J, Suihko V, and Eskola H. Sensitivity distributions of EEG and MEG measurements. *IEEE Trans Biomed Eng.* 1997; 44: 196-208.
34. Pascual-Marqui RD and Biscay-Lirio R. Spatial resolution of neuronal generators based on EEG and MEG measurements. *Int J Neurosci.* 1993; 68: 93-105.
35. Mosher JC, Spencer ME, Leahy RM, and Lewis PS. Error bounds for EEG and MEG dipole source localization. *Electroencephalography and clinical Neurophysiology.* 1993; 86: 303-321.
36. Liu AK, Belliveau JW, and Dale AM. Spatiotemporal imaging of human brain activity using functional MRI constrained magnetoencephalography data: Monte Carlo simulations. *Proc Natl Acad Sci U S A.* 1998; 95: 8945-50.
37. Menke W. *Geophysical Data Analysis: Discrete Inverse Theory.* San Diego, CA: Academic Press, 1989:
38. Grave de Peralta Menendez R, Gonzalez Andino S, and Lutkenhoner B. Figures of merit to compare linear distributed inverse solutions. *Brain Topography.* 1996; 9: 117-124.
39. Grave de Peralta-Menendez R, Hauk O, Andino SG, Vogt H, and Michel C. Linear inverse solutions with optimal resoluion kernels applied to electromagnetic tomography. *Human Brain Mapping.* 1997; 5: 454-467.
40. Lutkenhoner B and Grave de Peralta Menendez R. The resolution-field concept. *EEG and Clin. Neurophysiol.* 1997; 102: 326-334.
41. Grave de Peralta-Menendez R and Gonzalez-Andino SL. A critical analysis of linear inverse solutions to the neuroelectromagnetic inverse problem. *IEEE Trans Biomed Eng.* 1998; 45: 440-8.
42. Hari R, Joutsiniemi SL, and Sarvas J. Spatial resolution of neuromagnetic records: theoretical calculations in a spherical model. *Electroencephalography and clinical Neurophysiology.* 1988; 71: 64-72.
43. Supek S and Aine CJ. Simulation studies of multiple dipole neuromagnetic source localization: model order and limits of source resolution. *IEEE Trans. Biomed. Eng.* 1993; 40: 529-540.

44. Fuchs M, Wagner M, Wischmann HA, Kohler T, Theissen A, Drenckhahn R, and Buchner H. Improving source reconstructions by combining bioelectric and biomagnetic data. *Electroencephalogr Clin Neurophysiol.* 1998; 107: 93-111.
45. de Munck JC. A linear discretization of the volume conductor boundary integral equation using analytically integrated elements. *IEEE Trans. Biomed. Eng.* 1992; 39: 986-990.
46. Oostendorp TF and van Oosterom A. Source parameter estimation using realistic geometry in bioelectricity and biomagnetism. In: Nenonen J, Rajala HM, and Katila T, eds. *Biomagnetic Localization and 3D Modeling, Report TKK-F-A689.* Helsinki: Helsinki University of Technology, 1992:
47. Cuffin BN. Effects of head shape on EEG's and MEG's. *IEEE Trans. Biomed. Eng.* 1990; BME-37: 44-52.
48. Dale AM, Fischl B, and Sereno MI. Cortical Surface-Based Analysis I: Segmentation and Surface Reconstruction. *NeuroImage.* 1999; 9: 179-194.
49. Fischl B, Sereno MI, and Dale AM. Cortical Surface-Based Analysis II: Inflation, Flattening, and a Surface-Based Coordinate System. *NeuroImage.* 1999; 9: 195-207.
50. Dale AM and Sereno MI. Improved localization of cortical activity by combining EEG and MEG with MRI cortical surface reconstruction: A linear approach. *J. Cog. Neurosci.* 1993; 5: 162-176.
51. Knuutila JET, Ahonen AI, Hamalainen MS, Kajola MJ, Laine PO, Lounasmaa OV, Parkkonen LT, Simola JTA, and Tesche CD. A 122-channel whole-cortex squid system for measuring the brains magnetic fields. *IEEE Trans. Magn.* 1993; 29: 3315-3320.

6. Accuracy of a Realistic and Spherical EEG Head Model

6.1 Abstract

The accuracy of the volume conductor head model plays an integral part in the accuracy of inverse solution calculations to localize EEG sources in the brain. Because accuracy is difficult to judge in healthy human subjects, epilepsy patients undergoing invasive EEG provide and invaluable source of information. Using experimental data generated from implanted dipoles in such a patient, we were able to verify and compare the accuracy of a realistic and spherical head model over many dipole locations. For the most inferior dipoles, where the skull geometry is poorly represented by a sphere, the realistic head model was superior to the spherical model (RMS error of 8.5% versus 11.9%). For the remaining dipoles, the two models were comparable, with RMS errors of 6.85% for the realistic and 6.92% for the spherical. Knowledge of the different tissue resistivities is also required for accurate forward solutions. Using our experimental data, we were able to estimate the absolute resistivity values for brain, skull and scalp. The estimated resistivity values for brain:skull:scalp (Ω-m) for the realistic head model are 3.42 : 273 : 3.42. Due to the relative independence of the spherical head model over a wide range of resistivities and the effect of skull thickness, we could not estimate with any confidence the best absolute resistivities for the spherical head model. Our results provide direct validation of our realistic head model. Using a realistic geometry volume conductor provides an improvement in the accuracy of the forward head model, particularly in regions not well fit by the spherical approximation (e.g. inferior and frontal).

6.2 Introduction

Localization of neuronal activity using scalp EEG requires solving both the forward and the inverse problem. While we are not primarily concerned with accuracy of the forward model, *per se*, the accuracy of the forward model will affect any inverse algorithm used. Ultimately, we are interested in making non-invasive estimates of brain activity and this accuracy will, in part, reflect the accuracy of the forward solution. In this study we used both a realistic and a spherical geometry to generate a conductivity model for the head. We made direct comparisons between the forward solutions (i.e. surface potentials or measurements at the EEG electrodes) computed using those two head models and experimentally measured scalp EEG generated from many implanted dipolar sources.

The accuracy of the head model will be affected by numerous factors. These factors include the estimates of the boundaries of the different tissue types in the head, and the resistivities of the different tissue types. Instead of comparison of the forward solutions, most studies have used one head model to generate the forward solution and then used a different head model for source localization. We refer to this error in the inverse localization as "forward-inverse localization error." Previous studies have used theoretical considerations to examine the effect of variations in the geometry of the resistivity boundaries on both the forward solution directly and the forward-inverse

localization error. Some of this modelling work has studied various perturbations on the spherical model, such as ellipsoidal surfaces (1), eccentric spheres (2), small "bumps" or "depressions" (3), and variations in the radii of the surfaces (4-6). Other studies examined the effect of geometry in a realistic boundary element model (BEM) (7), finite element model (FEM) (8) and a finite difference model (9). In these studies, forward model difference were as large as 30% and forward-inverse localization errors were as large as 1.7 cm.

Additional work has examined the effect of mis-estimates of tissue resistivity (e.g. brain, skull or bone) on the head model. Using spherical models, a few groups have studied the resistivity effect (4, 6, 10). Other groups have used either FEM (11-14) or boundary element models (BEM) (15, 16) of the head. For large variations in resistivity, the forward-inverse localization errors could be greater than 2.0 cm.

In addition to the above modelling studies, some groups have compared different head models by performing inverse localizations using experimental data with the different head models. Fuchs et al. localized a single epileptic spike using both a spherical head model and a BEM realistic head model (17). The maximum difference in dipole location between the two head models was 2.4 cm. In addition the spatial localization using the realistic head model was in better agreement with the cortical anatomy around the temporal pole. In another study of an epileptiform discharge (18), realistic and spherical head models were used to localize an averaged interictal spike. The realistic model was 1.36 cm from the hippocampus (presumed to be the focus of seizure activity, but may not have been the actual source) and the spherical model localized the dipole 2.24 cm away from the hippocampus.

Overall, the theoretical and experimental results show that accurate resistivity and geometry information is important. Reported forward-inverse localization errors could be greater than 2 cm in some cases. While we mainly summarized the maximal reported errors, smaller errors may still be significant. For example, the thickness of the cortical ribbon is typically 3.0 mm (19-21). Localization errors greater than the cortical thickness can move a cortical source into white matter, or can move a source from one bank of a sulcus to another. Obviously, greater accuracy in both the forward solution and the inverse localization is desirable.

Unfortunately, all of these studies, while further characterizing the importance of geometry and resistivity in the head model, have certain limitations. In the theoretical studies, it is assumed that the spherical head model is the poorer of the two models being examined. That assumption may not necessarily always be true. In these experimental studies, the main limitation is that the actual generators could not be determined. The improvement in accuracy was inferred based upon anatomical or assumed clinico-anatomical correlations.

One previous study does provide some direct evidence for the increased accuracy of a more realistic head model (22). In three epilepsy patients with implanted depth electrodes, current dipoles were generated and the resulting scalp EEG was measured. In that experiment, the true location and the orientation of the current dipole was known. A realistic and a spherical head model were studied. The realistic head model, however, was only based upon the upper portion of the individual's scalp. The

remaining resistivity boundaries (outer and inner skull) were constructed by scaling the scalp surface. This resulted in three relatively smooth resistivity boundaries with uniform thickness. The difference between the realistic and spherical head models was quantified using localization error. The results varied from patient to patient. For one patient, the realistic head model was clearly better. For the other two, there was little improvement in localization when utilizing the realistic head model. The discrepancy was largely attributed to the signal to noise ratio (SNR), with the improvement of the realistic model larger when the SNR was larger.

In this study, we were able to extend these previous results. Again, we had the relatively unique opportunity to study the accuracy of the EEG forward solution using experimental scalp EEG measurements generated from current dipoles at known locations and orientations within a living patient's head. Using high resolution T1-weighted MRI, we constructed a more accurate head model than was used in the previous paper. In all of these data, we only compare forward solutions, not inverse localizations, which allows these results to be applicable to any inverse approach. We compared both a realistic BEM and spherical head model with those experimental measurements. We also examined a large range of resistivities to determine the optimal resistivity values for this patient. This data allowed us to determine the relative accuracy of the head models compared to one another, and also the absolute accuracy of the two models given the optimal resistivity values.

6.3 Methods

The subject was a patient with medically refractory epilepsy who had multi-contact electrodes implanted in the brain to monitor epileptic activity for presurgical evaluation. Informed consent for participation in the study was obtained from the patient according to Beth Israel Deaconess Medical Center procedures. A whole head, high resolution (1.4 x 1 x 1 mm) T1-weighted MRI data set was collected prior to the implantation procedure. Dipole sources with known locations and orientations were generated by injecting current between implanted depth electrode contacts and, simultaneously, the scalp EEG was measured.

6.3.1 Resistivity Boundaries

We generated a realistic head model and a spherical head model. To minimize the effect of the computational model on our comparison, we used the BEM to compute both head models. For the BEM forward computation, three resistivity boundaries are required: 1) inner skull, 2) outer skull, and 3) outer skin. The realistic surfaces were automatically reconstructed from high-resolution T1-weighted 3D MRI using our previously described technique (23). The corresponding spherical surfaces were computed with the same center as the center of the realistic inner skull surface, which was determined by averaging the locations of all the points used to specify the inner skull boundary. The radius for each of the spherical surfaces was calculated from the best fitting sphere for each of the realistic boundaries. The radii of the spherical inner skull, outer skull and outer skin were 75 mm, 78 mm, and 85 mm, respectively. Each of the resistivity boundaries is initially generated with 2562 vertices, and then for

computational tractability subsampled to 642 vertices. The realistic and spherical surfaces are shown in Figure 1.

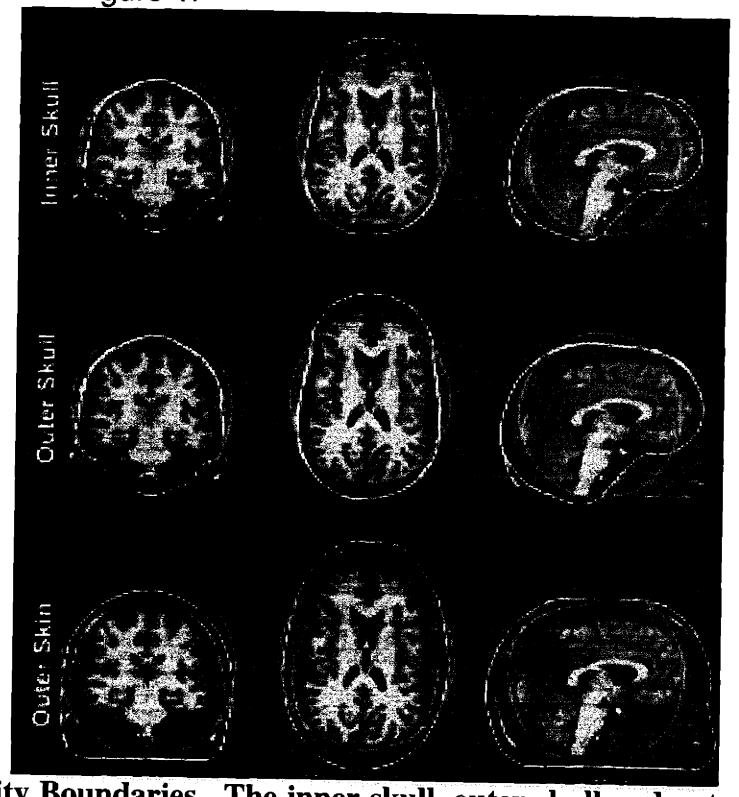

Figure 1: Resistivity Boundaries. The inner skull, outer skull and outer skin are overlaid (yellow) in three orthogonal views of the T1-weighted MR volume. The spherical estimates of the inner skull, outer skull and outer skin are overlaid in green.

6.3.2 Resistivities

We first examined the effect of varying the ratios of resistivities between the three regions. The resistivity ratios specify the surface topography of the scalp EEG (i.e. the 3-D "shape" of the EEG). The BEM head model requires the resistivities for each of the regions: brain, skull and scalp. We examined a large range of resistivity values that likely would encompass the real values (12). The range of resistivities, in Ω–m, for brain, skull, and scalp were 1.5 – 4.5, 80 – 500, and 1.15 – 3.45, respectively. By normalizing the error between the measurements and the model potentials, we remove the effect of the absolute values of the resistivities. This allows us to simply examine the effect of the ratios of resistivities. Since any three numbers can be specified, within a scaling factor, by two ratios, we held the scalp resistivity constant at 1.0, and varied brain resistivity from 0.4 – 4.0 and skull resistivity from 20 to 440.

Using a selected ratio of resistivities, we could then determined the best scaling factor. This scaling factor, along with the resistivity ratios, will specify the absolute resistivity values that result in a head model that best agrees with the experimental measurements.

6.3.3 Current Dipoles

The implanted electrodes were used to create current dipoles with known locations and orientations in the brain. The electrodes were rings mounted 0.5 cm apart (center to center) on hollow plastic catheters containing wires connected to each ring; each catheter had 7 or 8 rings. The catheters passed through the skull through electrically non-conducting plastic anchors which completely blocked the surgical openings in the skull used to insert the catheters into the brain. Biphasic 4 μA current pulses with a total pulse duration of 35 ms were passed through various pairs of electrodes to create the dipoles. The shape of the pulse was optimized to provide as flat a curve as possible for accuracy of A/D conversion. This current pulse amplitude is well below the threshold of stimulation. The electrode spacing was selected as either 0.5 cm or 1.0 cm which corresponds to dipole moments of either 2 or 4 μA-cm, respectively. Multiple current pulses were applied to each electrode pair so that signal averaging could be performed with the recorded scalp EEGs.

Using 4 different catheters, 15 current dipoles were generated. The 3-dimensional electrode locations were determined from a CT; the scalp EEG electrodes were also present when this CT was obtained. The dipole orientations were estimated as the best-fitting orientation using the locations of the dipoles on the same catheter. The locations of the dipoles are shown in Figure 2.

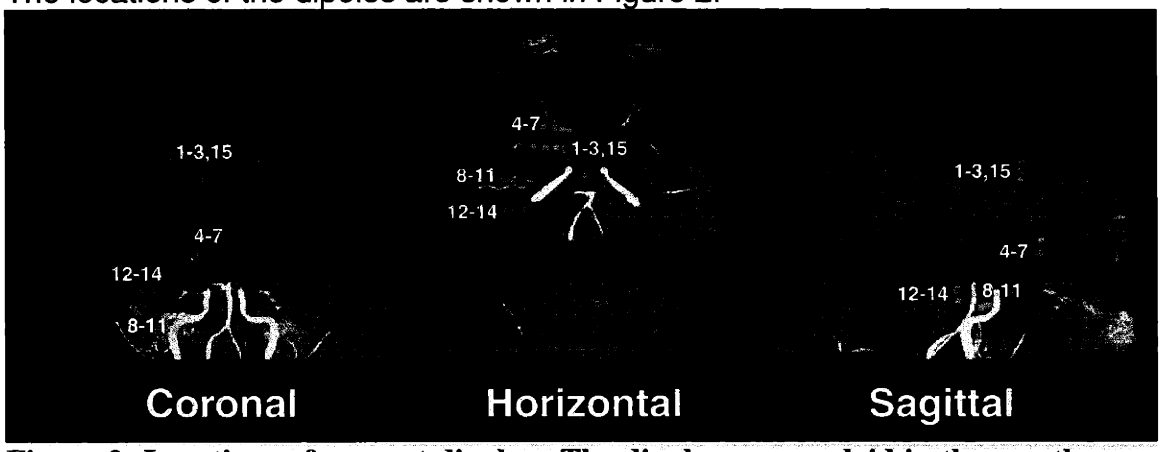

Figure 2: Locations of current dipoles. The dipoles are overlaid in three orthogonal views of a maximum intensity projection of the MR volume.

6.3.4 EEG

A total of 27 scalp EEG electrodes were placed in a modified 10-20 system configuration. Additional electrodes at non-standard locations were included where possible and some locations were shifted or omitted to avoid surgical wounds in the scalp. Unfortunately, there was an open hole (3 mm diameter) in the left temporal region of the skull due to a missing catheter. This hole could provide an unnatural path for current to get to the scalp and distort the EEG spatial pattern. To minimize the possible distortion, no electrodes were placed near this hole. The 3-dimensional EEG electrode locations were determined from the same CT used to determine the implanted electrode locations. The CT coordinate system was then manually co-registered with the MRI coordinate system. The locations of the electrodes are shown in Figure 3.

The EEG produced by each current pulse to a pair of implanted electrodes was digitized at a rate of 2000 samples/sec. A bandwidth of 1 to 500 Hz was used for the recordings followed by digital (moving average) LP filtering at 70 Hz. EEGs of each pulse were visually inspected and those with artifacts or high noise levels were not included in the average. For each dipole, approximately 500 current pulses were averaged.

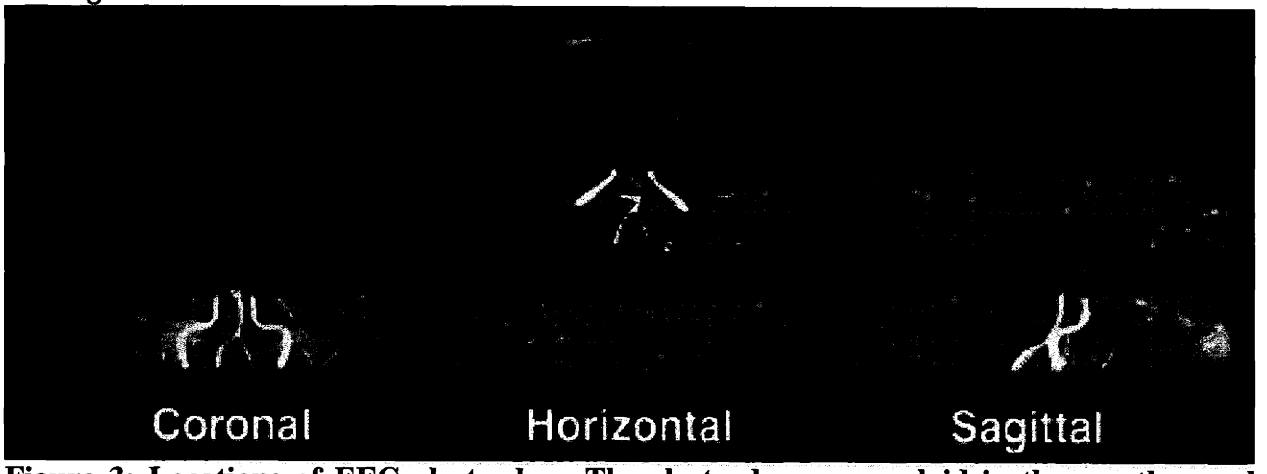

Figure 3: Locations of EEG electrodes. The electrodes are overlaid in three orthogonal views of a maximum intensity projection of the MR volume.

6.3.5 Forward Computation

The BEM was used for calculating the EEG forward solution (24-26). The isolated problem approach of (27) was used in this forward computation. The inverse computation can be divided into two separate computations (26). The first portion only involves the resistivity boundaries (inner skull, outer skull, and outer skin) and the resistivities in each region. This computation needs to only be calculated once for any given individual. The second computation computes the forward solution over all the electrodes for each dipole, given its location and orientation. The initial computation requires approximately 40 minutes on an SGI (Mountain View, CA) O2 computer with an R5000 processor. Then, the forward solution computation for each dipole takes approximately 2 seconds.

6.3.6 Error Metric

For both head models, we computed the scalp EEG for each of the 15 dipoles, using the locations and orientations determined from CT. Initially we assumed a single ratio of resistivities for brain, skull and scalp of 1:80:1. To directly compare these computed forward solutions with the actual scalp EEG measurements, all of the scalp potentials (for the models and measurements) were normalized by the norm of the potentials (Equation 1).

$$V_i^{norm} = \frac{V_i}{\sqrt{\sum_i (V_i)^2}} \quad [1]$$

where V_i is scalp EEG measurement at electrode i. Then for each dipole, we computed the normalized RMS error, averaged across all electrodes, between the head model and the measurements, given by:

$$\%\ \text{error} = \frac{\sqrt{\sum_i \left(V_i^{Meas} - V_i^{Model}\right)^2}}{\sqrt{\sum_i \left(V_i^{Meas}\right)^2}} \times 100 \quad [2]$$

where V_i^{Meas} is normalized scalp EEG measurement at electrode i, and V_i^{Model} is the normalized model-estimated scalp EEG at electrode i.

6.4 Results

We computed the % RMS error for each dipole using the realistic and spherical head models (Figure 4A). The average RMS error for all 15 dipoles for the realistic head model is 7.28%, compared to 8.26% RMS error for the spherical head model. The largest errors occurred in the most inferior dipoles (8 -11). The smallest errors were found in the more superior dipoles (1 - 3). The dipole locations can be found in Figure 3. The RMS error averaged across the inferior dipoles 8 – 11 for the realistic and spherical models are 8.48% and 11.94%, respectively. The RMS error averaged across the other 11 dipoles for the realistic and spherical model is 6.85% and 6.92%, respectively.

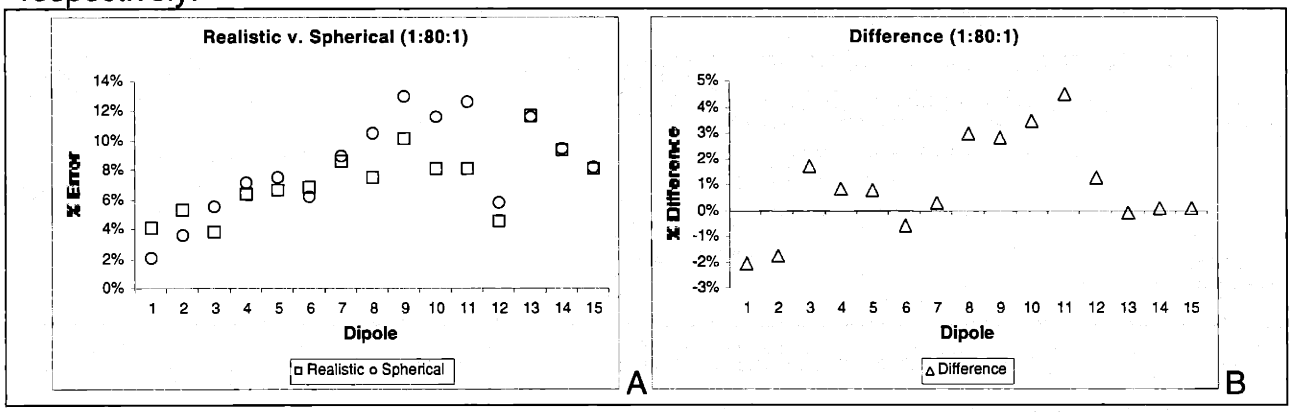

Figure 4: Error (A) and Relative Error (Spherical – Realistic Error) (B) versus Dipole Number.

Using the data from Figure 4A, we then computed the relative difference in error between the realistic and spherical head models (spherical error – realistic error) for each dipole (Figure 4B). In figure 4B, positive values indicate dipoles that are better fit with the realistic dipole. Negative values indicate dipoles that are better fit with the spherical model. The largest positive relative error was found in the inferior dipoles. The spherical model was better for only three dipoles, located more superiorly.

In Figure 5A, we display the % error for each dipole as a function of the distance of the dipole from the center of the head model. There is no relationship between distance and error in either the realistic or the spherical head model.

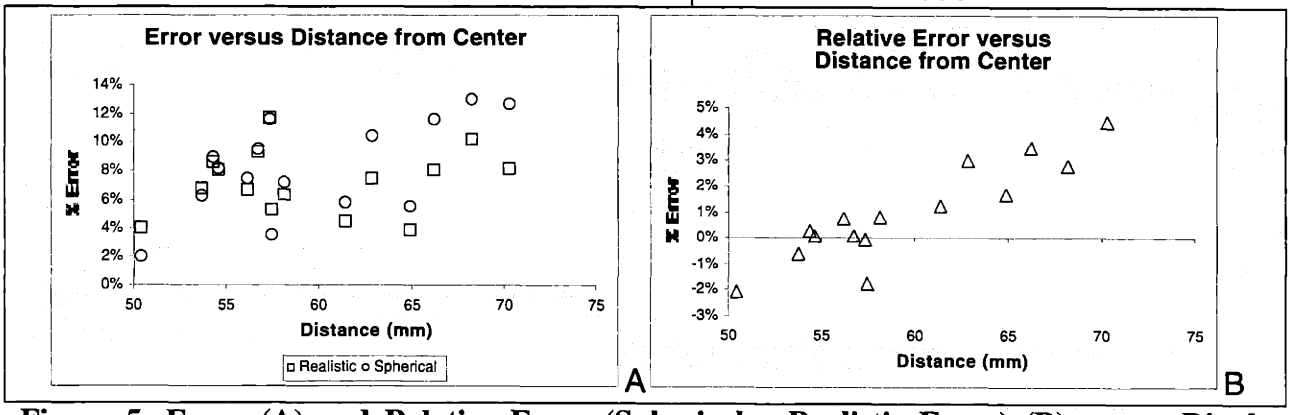

Figure 5: Error (A) and Relative Error (Spherical – Realistic Error) (B) versus Dipole Distance from Center for Realistic and Spherical Models.

Using the results presented in Figure 5A, we computed the relative error as a function of distance (Figure 5B). Clearly, there is a linear trend in relative error with distance ($R^2 = 0.812$).

Similar to the data in Figure 5, we calculated the % error and relative error for each dipole as a function of the measured EEG SNR) for that dipole in Figure 6, respectively. The average SNR ranged from 4.9 to 23.3, with an average SNR of 12.9. For each model independently, there does not appear to be any correlation between SNR and the % error. There is also no relationship between the relative error and SNR ($R^2 = 0.0983$).

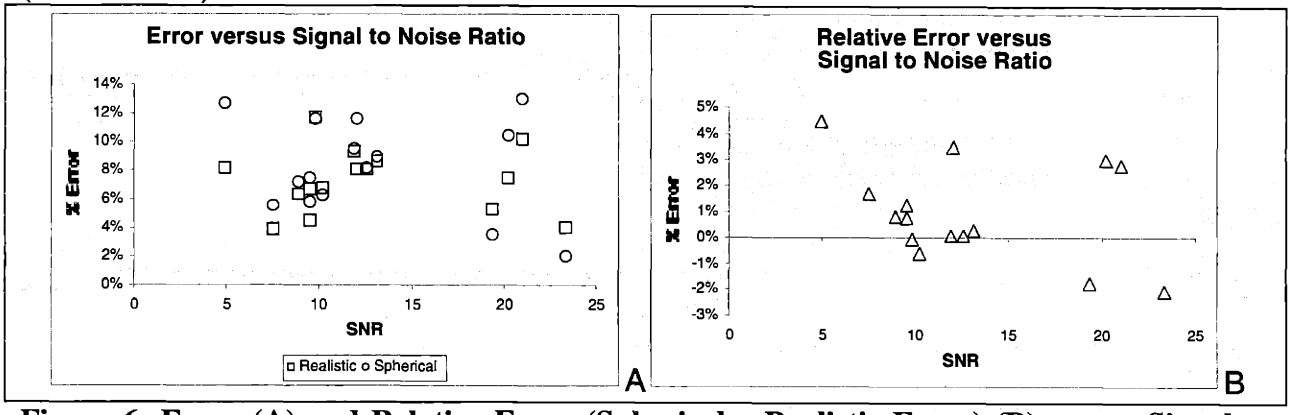

Figure 6: Error (A) and Relative Error (Spherical – Realistic Error) (B) versus Signal to Noise Ratio for Realistic and Spherical models.

The remaining data examined the effect of varying the resistivity of the three different regions. First, we examined the effect of varying the ratios of the resistivities for the realistic and spherical head models. We averaged the error over all 15 dipoles for each set of resistivity ratios. The resistivity ratios for brain:skull:scalp varied from 0.4 : 20 : 1.0 to 4.0 :440 : 1.0. The error surfaces are shown in Figure 7.

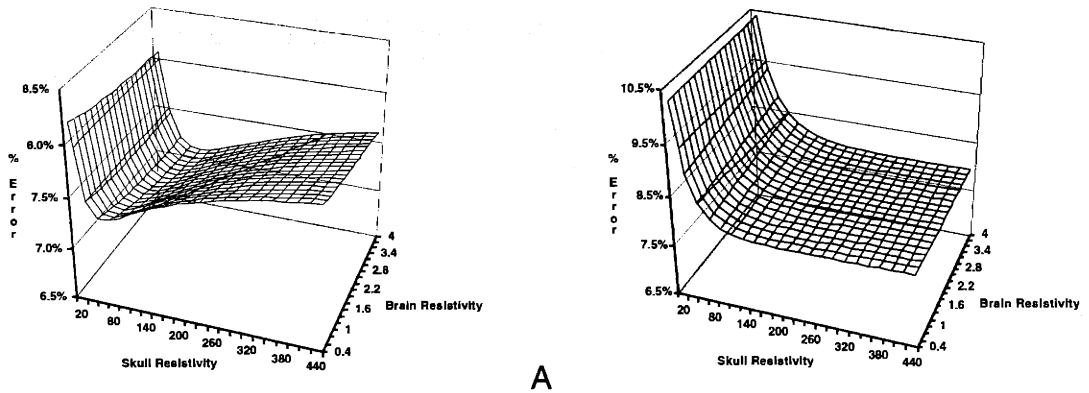

A B

Figure 7: Error versus Skull and Brain Resistivity for the Realistic (A) and Spherical (B) Head Models. Note that the vertical scale (% Error) differs between the realistic and spherical graphs.

For both head models, we can clearly see that the skull resistivity plays the largest role in determined the average error. In comparison, there is little dependence on the brain resistivity, especially for the spherical head model.

Given the dominant effect of the skull resistivity, we kept brain and scalp resistivity equal at 1.0 to determine the lowest error for the two models (Figure 8). For the realistic model, the lowest error between the model and the measurements (normalized) is 7.28% and occurs at a skull resistivity of 80. For the spherical model, the lowest error (7.92%) occurs between 220 and 260. However, above a skull resistivity of 160 (% error = 7.95%), there is the skull resistivity has very little effect on the error.

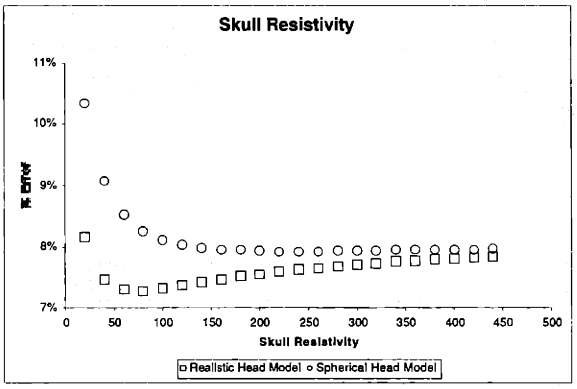

Figure 8: Error versus Skull Resistivity for the Realistic and the Spherical Head Models. Brain and scalp resistivity were equal at 1.0.

Using the lowest resistivity ratios determined from Figure 8, which best fit the normalized experimental measurements, we computed the scaling factor to best match the absolute measurements. For each dipole we computed the ratio of the norm (for all 15 dipoles and all 27 surface electrodes) of the model scalp EEG to the norm of the experimental measurements. For the realistic head and a resistivity ratio of 1:80:1 for brain:skull:scalp, the average scaling factor was 3.42. For the spherical head and a resistivity ratio of 1:240:1 for brain:skull:scalp, the average scaling factor was 4.11. In other words, for this patient, the optimal resistivity values for brain:skull:scalp (Ω-m) for

the realistic head model are 3.42 : 273 : 3.42 and for the spherical model are 4.11 : 987 :4.11.

6.5 Discussion

The results presented here were based upon experimental measurements from a patient. We were able to make relevant comparisons between a realistic and a spherical head model. Overall, the two head models are quite comparable in accuracy using the optimal skull resistivity ratios (average RMS error of 7.28% for the realistic and 7.92% for the spherical). The relative accuracy was quite different for the most inferior dipoles (8 – 11), where the realistic head model (8.48%) is more accurate than the spherical head model (11.94%). While the data in Figure 5 show a relationship between accuracy and distance from the center of the surfaces, the increased accuracy of the realistic model is more likely due to the location, rather than the distance. It turns out that the inferiorly located dipoles are also the farthest from the center. That area of the skull is extremely non-spherical, which is probably the cause for the improvement provided by the realistic head model. A similar dependence on source location has been reported for MEG (27).

Unlike the previous study (22), which found the realistic model more accurate than the spherical at higher SNR, we found essentially no relationship between the measurement SNR and the relative accuracy of head models. This discrepancy may be due to the small number of dipoles sampled in both the previous work and the present study.

This experimental data also allowed us to determine the absolute resistivities that would best fit the measurements for the realistic and spherical models. The absolute resistivity values for the realistic model (3.42 : 273 : 3.42 Ω-m) are within the range of realistic resistivities (12). In contrast, the optimal resistivity values for the spherical model (4.11 : 987 :4.11 Ω-m), especially for the skull resistivity, are larger than would be predicted by the current literature. The large discrepancy between the absolute realistic and spherical absolute resistivities is largely the result of two factors. The first is the difficulty of determining the optimal resistivity ratios for the spherical head model. The average error is essentially independent of the skull resistivity above 160, varying from 7.95% to 7.92%. The resulting range of absolute skull resistivities extends from 500 for a skull receptivity of 160 to 2880 for a skull resistivity of 440. The second factor that affects the estimation of absolute resistivities in the spherical head model is the estimate of the skull thickness. We used a simple, single set of concentric spheres that were best fit to the realistic head model. The realistic head model had a skull thickness of 4 mm, compared to the spherical skull which was 3 mm thick. Due to the simple and symmetric geometry of the spherical head model, increasing the spherical skull thickness will reduce the conductivity values proportionally. For example, if one uses a skull thickness of 6 mm (1), instead of 3 mm, the optimal absolute resistivities would be 2.05 : 493 : 2.05, which is in the range of realistic resistivities. Given the relative independence of the spherical head model over a wide range of resistivities and the effect of skull thickness, we cannot estimate with any confidence the best absolute resistivities for the spherical head model.

This variation in the absolute resistivity values is not significant in terms of localization errors for EEG measurements alone. The spatial localization for any inverse approach will only depend on the topography of the scalp EEG, which is dependent on the resistivity ratios. Variations in the absolute resistivity will not affect that topography, and hence will not affect the localization. The absolute resistivities will alter the absolute magnitude of the estimated neuronal sources. Notice that the topography of the scalp EEG computed with the spherical head model is much less sensitive to the resistivities (Figure 8). Over the range of skull resistivities from 160 to 440, the error for the spherical head model only ranges from 7.92% to 7.96%, which is approximately 1/10 the variation of the realistic head model over the same range. The symmetry present in the spherical head model results in small changes in the overall topography of the scalp EEG as skull resistivity is changed.

However, the estimation of absolute resistivity values is of critical importance for combining EEG measurements with MEG measurements for localization of neuronal activity. Numerous authors have shown that combined EEG/MEG measurements localize activity more accurately than either modality alone (28-34). When the forward solution is computed with incorrect absolute resistivity, but accurate resistivity ratios, there is a discrepancy between the electric and magnetic forward solutions. For example, if the resistivities are 10 times to large, the potentials generated by unit activity at a given location will be underestimated by a factor of 10. This does not change the localization results for the EEG measurements alone. However, if EEG and MEG data are combined, the source at the given location can either provide a good match for the EEG data (10 times the unit dipole strength to compensate for factor of 10 in resistivity) or a good match for the MEG data (unit strength dipole), but cannot account for both sets of data simultaneously. Then, the best fitting dipole location will be mis-localized from the correct location to best fit the two discrepant measurements. It is possible that, depending on the amount of the mis-estimation of the absolute resistivities, the combined electromagnetic inverse localization would actually be worse than using either approach alone. This requirement of knowledge of the absolute resistivities may limit the use of the spherical head model for combined EEG/MEG studies, given the above mentioned difficulties in estimating those resistivities for the spherical head model.

Finally, the head model accuracy that we have demonstrated is quite impressive considering the average measurement SNR of 12.9, which corresponds to 7.7% noise. Also, errors in determining some of the model parameters (e.g. dipole orientations) will result in errors in our assessment of the forward model accuracy. In fact, if we optimize the dipole orientation, the average error for the realistic head model is further reduced to 5.79%, with the angle between the optimal and experimentally specified orientation ranging from 9° to 30°. Given these experimental uncertainties, the errors we report here are likely to be worse than the inherent accuracy of this realistically shaped head model.

6.6 Conclusions

These results provide direct evidence that for locations near the base of the skull, a realistic head model is more accurate than a spherical head model, adding further

support to the use of more accurate head models in the EEG forward problem. Our current implementation of the realistic BEM head model is completely automatic and requires only a high resolution T1-weighted MRI to generate the resistivity boundaries. This ease of use makes the routine use of our realistic head model feasible. With a average error of approximately 7%, we are quite confident in the use of this realistic model in the analysis of experimentally measured scalp EEG. This is especially true given that the additive noise present in many evoked potential experiments can be on that same order (i.e. SNR of ~ 14).

However, we would be remiss if we did not acknowledge the accuracy of the spherical model (average of approximately 8%). The difference between the realistic and spherical head models in many locations is quite small. Given the simple computational requirements of the spherical solution, there are still numerous situations where using a simplified spherical geometry for the head model is adequate.

6.7 References

1. Cuffin BN. Effects of head shape on EEG's and MEG's. *IEEE Trans. Biomed. Eng.* 1990; BME-37: 44-52.
2. Cuffin BN. Eccentric spheres models of the head. *IEEE Trans Biomed Eng.* 1991; 38: 871-8.
3. Cuffin BN. Effects of local variations in skull and scalp thickness on EEG's and MEG's. *IEEE Trans Biomed Eng.* 1993; 40: 42-8.
4. Stok CJ. The influence of model parameters on EEG/MEG single dipole source estimation. *IEEE Trans Biomed Eng.* 1987; 34: 289-96.
5. Eshel Y, Witman S, Rosenfeld M, and Abboud S. Correlation between skull thickness asymmetry and scalp potential estimated by a numerical model of the head. *IEEE Trans Biomed Eng.* 1995; 42: 242-9.
6. Radich BM and Buckley KM. EEG dipole localization bounds and MAP algorithms for head models with parameter uncertainties. *IEEE Trans Biomed Eng.* 1995; 42: 233-41.
7. Buchner H, Waberski TD, Fuchs M, Wischmann HA, Wagner M, and Drenckhahn R. Comparison of realistically shaped boundary-element and spherical head models in source localization of early somatosensory evoked potentials. *Brain Topogr.* 1995; 8: 137-43.
8. Yan Y, Nunez PL, and Hart RT. Finite-element model of the human head: scalp potentials due to dipole sources. *Med Biol Eng Comput.* 1991; 29: 475-81.
9. Witwer JG, Trezek GJ, and Jewett DL. The effect of media inhomogeneities upon intracranial electrical fields. *IEEE Trans Biomed Eng.* 1972; 19: 352-62.
10. Ary JP, Klein SA, and Fender DH. Location of sources of evoked scalp potentials: corrections for skull and scalp thicknesses. *IEEE Trans Biomed Engineering.* 1981; 28: 447-452.
11. Awada KA, Jackson DR, Baumann SB, Williams JT, Wilton DR, Fink PW, and Prasky BR. Effect of conductivity uncertainties and modeling errors on EEG source localization using a 2-D model. *IEEE Trans Biomed Eng.* 1998; 45: 1135-45.

12.Haueisen J, Ramon C, Eiselt M, Brauer H, and Nowak H. Influence of tissue resistivities on neuromagnetic fields and electric potentials studied with a finite element model of the head. *IEEE Trans Biomed Eng.* 1997; 44: 727-35.
13.Marin G, Guerin C, Baillet S, Garnero L, and Meunier G. Influence of skull anisotropy for the forward and inverse problem in EEG: simulation studies using FEM on realistic head models. *Hum Brain Mapp.* 1998; 6: 250-69.
14.Pohlmeier R, Buchner H, Knoll G, Rienacker A, Beckmann R, and Pesch J. The influence of skull-conductivity misspecification on inverse source localization in realistically shaped finite element head models. *Brain Topogr.* 1997; 9: 157-62.
15.Musha T, Ivanov V, and Konyshev V. Source estimation in the human brain from EEG based on the SSB Head Model. *Methods Inf Med.* 1994; 33: 120-2.
16.Haueisen J, Bottner A, Nowak H, Brauer H, and Weiller C. The influence of conductivity changes in boundary element compartments on the forward and inverse problem in electroencephalography and magnetoencephalography. *Biomed Tech (Berl).* 1999; 44: 150-7.
17.Fuchs M, Drenckhahn R, Wischmann HA, and Wagner M. An improved boundary element method for realistic volume-conductor modeling. *IEEE Trans Biomed Eng.* 1998; 45: 980-97.
18.Herrendorf G, B.J. S, Kolle R, Baudewig J, Waberski TD, Buchner H, and Paulus W. Dipole-source analysis in a realistic head model in patients with focal epilepsy. *Epilepsia.* 2000; 41: 71-80.
19.Brodmann K. *Vergleichende Lokalisationslehre der Großhirnrinde in ihren Prinzipien dargestellt auf Grund des Zellenbaues.* Leipzig: Barth, 1909:
20.Zilles K. Cortex. In: Paxinos G, eds. *The Human Nervous System.* San Diego, CA: Academic Press, 1990: 575-802.
21.von Economo C. *The cytoarchitectonics of the human cerebral cortex.* London: Oxford University Press, 1929:
22.Cuffin BN. EEG localization accuracy improvements using realistically shaped head models. *IEEE Trans Biomed Eng.* 1996; 43: 299-303.
23.Dale AM and Sereno MI. Improved localization of cortical activity by combining EEG and MEG with MRI cortical surface reconstruction: A linear approach. *J. Cog. Neurosci.* 1993; 5: 162-176.
24.Barnard ACL, Duck IM, Lynn MS, and Timlake WP. The application of electromagnetic field theory to electrocardiography - II: Numerical solution of the integral equations. *Biophys.* 1967; 7: 463-491.
25.de Munck JC. A linear discretization of the volume conductor boundary integral equation using analytically integrated elements. *IEEE Trans. Biomed. Eng.* 1992; 39: 986-990.
26.Oostendorp TF and van Oosterom A. Source parameter estimation in inhomogeneous volume conductors of arbitrary shape. *IEEE Trans Biomed Eng.* 1989; 36: 382-91.
27.Hamalainen MS and Sarvas J. Realistic conductivity geometry model of the human head for interpretation of neuromagnetic data. *IEEE Trans. Biomed. Eng.* 1989; 36: 165-171.

28.Fuchs M, Wagner M, Wischmann HA, Kohler T, Theissen A, Drenckhahn R, and Buchner H. Improving source reconstructions by combining bioelectric and biomagnetic data. *Electroencephalogr Clin Neurophysiol.* 1998; 107: 93-111.
29.Cohen D and Cuffin BN. Demonstration of useful differences between magnetoencephalogram and electroencephalogram. *Electroencephalography and clinical Neurophysiology.* 1983; 56: 38-51.
30.Mosher JC, Spencer ME, Leahy RM, and Lewis PS. Error bounds for EEG and MEG dipole source localization. *Electroencephalography and clinical Neurophysiology.* 1993; 86: 303-321.
31.Lopes da Silva FH, Wieringa HJ, and Peters MJ. Source localization of EEG versus MEG: empirical comparison using visually evoked responses and theoretical considerations. *Brain Topogr.* 1991; 4: 133-42.
32.Pascual-Marqui RD and Biscay-Lirio R. Spatial resolution of neuronal generators based on EEG and MEG measurements. *Int J Neurosci.* 1993; 68: 93-105.
33.Cohen D and Cuffin BN. A method for combining MEG and EEG to determine the sources. *Phys Med Biol.* 1987; 32: 85-9.
34.Ko DY, Kufta C, Scaffidi D, and Sato S. Source localization determined by magnetoencephalography and electroencephalography in temporal lobe epilepsy: comparison with electrocorticography: technical case report. *Neurosurgery.* 1998; 42: 414-21; discussion 421-2.

7. Simultaneous EEG/fMRI Measurement/Localization

7.1 Abstract

Combined analysis of electroencephalography (EEG) and functional magnetic resonance imaging (fMRI) has the potential to provide higher spatiotemporal resolution than either method alone. In some situations, where the activity of interest cannot be reliably reproduced (e.g. epilepsy, learning, sleep states), accurate combined analysis will require simultaneous acquisition of EEG and fMRI. Simultaneous measurements ensure that the EEG and fMRI recordings reflect the exact same brain activity.

We took advantage of the spatial filtering properties of the bipolar montage to allow recording of evoked potentials with fMRI. These EEG and fMRI measurements are of sufficient quality to allow source localization of the cortical generators. In addition, our source localization approach provides a principled combined EEG/fMRI analysis (fEEG), without requiring any manual selection of fMRI activations or placement of source dipoles.

We found good spatial overlap between the two techniques independently. As expected, the combined EEG/fMRI analysis provided better spatiotemporal resolution than either approach alone. Ultimately, this type of simultaneous acquisition and analysis will allow true multimodal imaging for the accurate characterization of neurophysiological activity in the human brain.

7.2 Introduction

Functional Magnetic Resonance Imaging (fMRI) and Electroencephalography (EEG) reflect two fundamentally different aspects of brain activity. fMRI measures changes in the blood oxygenation (1-3), whereas EEG measures the electric potential directly generated by neuronal activity (4). While the underlying contrast mechanisms are different from fMRI (hemodynamic) and EEG (electromagnetic), they are complementary is their spatiotemporal resolutions. fMRI has high spatial resolution, typically on the order of millimeters (5), while EEG has millisecond temporal resolution (4).

Although separate measurements of fMRI and EEG will be adequate for many situations, simultaneous acquisition is necessary when the activity of interest cannot be easily reproduced. For example, in epilepsy patients, spontaneous interictal activity (epileptiform activity between seizures) may vary from spike to spike, which may reflect different cortical generators. Simultaneous EEG/fMRI recordings have been used (6, 7) to measure the interictal activity with the hypothesis that interictal epileptiform discharges are likely to produce a focal change measurable by fMRI (8). While those studies used the simultaneously recorded EEG to monitor for the presence of interictal activity, they did not use the EEG collected for any type of localization.

Other work has combined the analysis of functional imaging and electrophysiological data that was collected separately. These studies include (a) Positron emission tomography (PET) and EEG (9, 10) (b) fMRI and EEG (11) (c) fMRI and magnetoencephalography (MEG) (12, 13) (d) fMRI, MEG and EEG (14) (e) fMRI,

EEG and invasive recordings (15), and (f) PET, MEG and invasive recordings (16). All of these studies primarily used the spatial information from the functional imaging data to guide the placement of current dipoles for the EEG and/or MEG inverse solution. This type of "combined" analysis requires significant manual intervention, since one must decide whether to "place" a dipole in a region of fMRI activation.

This work represents a significant advance, both in terms of the measurement technique and the combined source localization approach. For the first time, we collect evoked response potentials to a visual stimulus along with fMRI at 1.5 Tesla. Both types of data were of sufficient quality to allow source localization. In addition, our combined fMRI/EEG inverse procedure allows a principled combination of the spatial information provided by fMRI, without any manual selection of fMRI activations.

Methods.

Subject Information: Three normal volunteers were scanned (two male, one female) ages 28 - 37. Informed consent was obtained from each subject prior to the experiment in accordance with Massachusetts General Hospital policies (IRB #1999-P-010946/1; MGH). All subjects have normal or corrected to normal vision. The SNR of the BOLD recording for the second male subject was not sufficient for our analysis, therefore we present results only for the remaining two subjects.

Anatomical MRI acquisition: Anatomical MRI was performed using a quadrature birdcage transmit/receive head coil on our 1.5 T scanner (General Electric, Milwaukee, WI). For each subject, three whole head acquisitions were collected using T1 weighted 3D-SPGR (TR/TE = 24 ms/8 ms) sequence with 124 slices 1.3 mm thick (matrix size 256×192, FOV 25 cm). The individual acquisitions were motion corrected and averaged to increase gray/white matter contrast to noise.

Functional MRI acquisition: Functional MRI was performed on the same 1.5 T scanner, using a quadrature birdcage transmit/receive head coil. The first echo-planar sequence was a T1-weighted spin-echo inversion recovery (TR/TE/TI = 2s / 20 ms / 800 ms) with 10 slices (7 mm-thick, 1 mm gap, 1.56 mm × 1.56 mm in-plane resolution) oriented perpendicular to the calcarine fissure was acquired. These images were later used to coregister the functional data with the subject's anatomical MRI set. Functional MRI data were acquired from those same slices using a gradient echo sequence (TE/TR = 50 ms/1000 ms) with the same slice thickness and gap, but 3.1 mm x 3.1 mm in-plane resolution. We have designed our own gradient echo sequence adapted for interleaved fMRI and EEG acquisition (**Fig. 1**). The sequence allows for 30 seconds of continuous fMRI acquisition, followed by a window of 30 seconds without MRI scanning for clean EEG acquisition. Both fMRI and EEG windows were structured to include 15 seconds of checkerboard reversal visual stimulation followed by 15 seconds of fixation. This interleaved EEG/fMRI sequence cycles for 15 minutes for each run and data was collected from each subject for a total of 2 runs or 450 fMRI time points. A workstation (SGI - O_2) was used to trigger both the MRI scanner and the EEG acquisition hardware, **Fig. 1** show the timing diagram for these two types of trigger used. The external triggering of the MRI scanner was necessary to achieve accurate synchrony with the EEG triggering and to avoid time-out of the General Electric scanner system. After

approximately 19 seconds from the beginning of the EEG window a MRI trigger pulse was sent to the scanner to avoid this time-out glitch. This pulse was sent during fixation in the EEG window and did not interfere with the EEG acquisition.

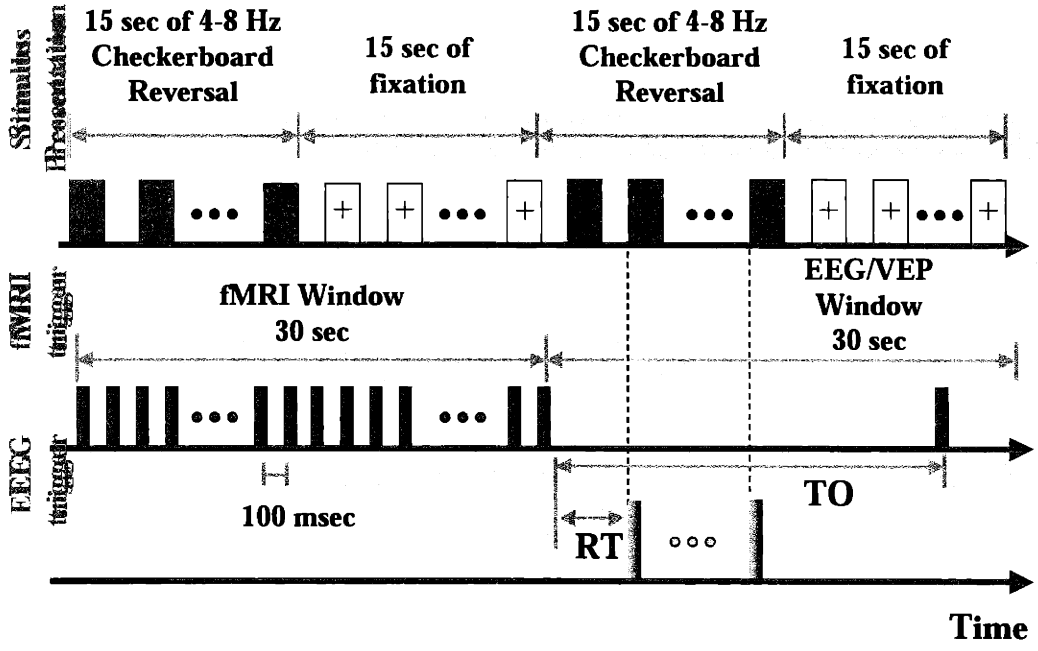

Fig. 1: The sequence used for interleaved EEG/fMRI recordings. In blue are depicted the triggers that are delivered to the EEG recording system, in orange the triggers that are delivered to the 1.5 Tesla scanner system and on the top is sketch of the stimulus presentation. "RT" in the figure indicates the delay needed for the recovery time of the amplifiers from the transients' generated during scanning, due to influence of RF and magnetic gradient switching. "TO" is the fMRI pulse sent to the scanner to avoid time-out. The sequence in figure is repeated 15 times in each run (2 runs @ 4 Hz, 1 run @ 8 Hz) to collect a total of 1,200 epochs.

We examined both structural and functional scans for possible local artifacts of the MRI due to the presence of the EEG cap (Neuroscan Labs) on the subject's head. **Fig. 2** shows that the position of electrodes is visible in the structural scans as signal dropout, but the brain's parenchyma was not affected by the presence of the electrodes.

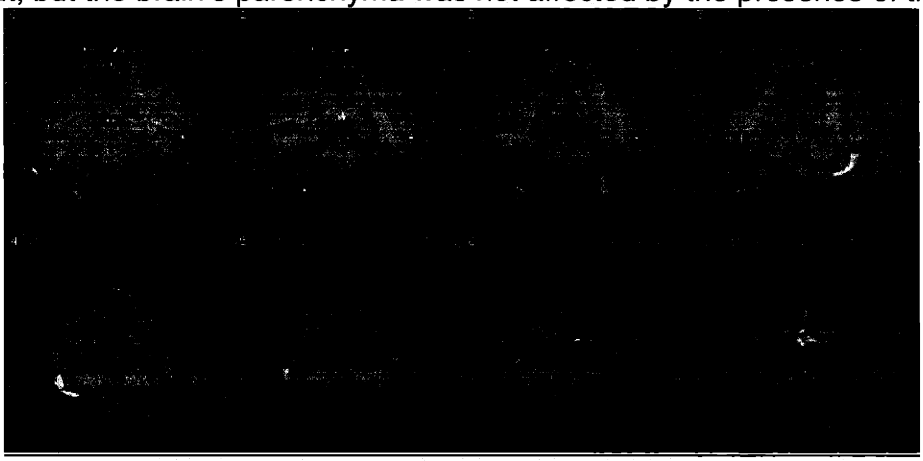

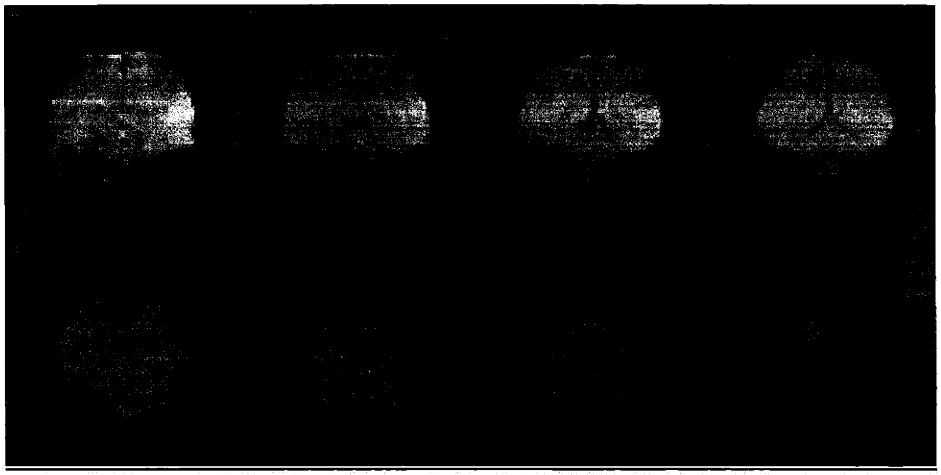

Fig. 2: (Top) EPI high resolution T1 weighted images. The presence of the electrodes can be clearly seen on the structural images (see green arrows). (Bottom) EPI gradient echo images, all the different slices acquired are unaffected from any type of image artifact despite the presence of an EEG cap with 32-electrodes on the subject's head.

fMRI Analysis: At the beginning of each fMRI window, the spins are back into a resting state after more than 10 seconds without RF excitation during the EEG window. Statistical analysis of the MRI signal was done after removing the first five (5) time points of each fMRI window, given the initial lack of equilibrium of the spins for each slice (17). **Fig. 3** shows this problem in detail: at the beginning of each fMRI window the spins are in a complete relaxation state and an overshoot response is visible. In a previous study we found that it is sufficient to discard the first five time points at the beginning of each fMRI window.

We applied a Gaussian smoothing kernel (FWHM of 1 voxel) to the raw fMRI data. Then, the fMRI data was analyzed using the standard Student's t-test (MEDx, Sensor Inc.) comparing fixation to checkerboard visual stimulation. The standard "MEDx" algorithm for cluster analysis was used with a Z score threshold of 2.3, the details of this method can be found in (18).

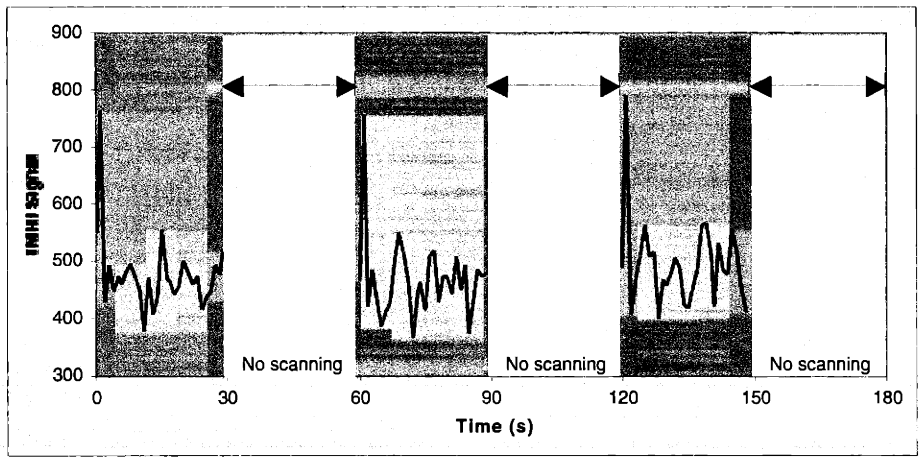

Fig. 3: The MRI signal using our gradient echo sequence at an arbitrary voxel, this time course shows the overshoot problem of lack of equilibrium for the spins at the beginning of

the fMRI window. We selected a voxel without activation to show that the overshoot is much larger than the common fluctuations of the BOLD signal.

EEG acquisition: Continuous EEG was recorded inside the 1.5 T magnetic field with a 32-channel OptiLink EEG (Neuro Scan Labs, Sterling, VA), amplified using SynAmps (Neuro Scan Labs) and all subjects were wearing a 32-channel MRI-Quickcap (Neuro Scan Labs). All recordings were bipolar starting from the first amplification stage, to reduce ballistocardiogram noise. (We modified the OptiLink system to obtain the following montage (-) → (+): 1.Cz→C3 2.C3→T7 3.T7→M1 4.M1→M2 5.M2→T8 6.T8→C4 7.C4→Cz 8.FP1→F3 9.F3→FC3 10.FC3→C3 11.C3→CP3 12.CP3→P3 13.P3→O1 14.FP2→F4 15.F4→FC4 16.FC4→F4 17.C4→CP4 18.CP4→P4 19.P4→O2 20.F7→FT7 21.FT7→T7 22.T7→TP7 23.TP7→P7 24.F8→FT8 25.FT8→T8 26.T8→TP8 27.TP8→P8 28.Fz→FCz 29.FCz→Cz 30.Cz→CPz 31.CPz→Pz 32.Pz→Oz). The data were acquired with a PC (400 MHz Pentium PII) running the Scan acquisition software (Neuro Scan Labs). Bandpass filtering was performed from 0.01 Hz to 70 Hz and a subsequent 50 Hz Butterworth lowpass IIR filter with a Hanning window (1024 points) was applied. An O2 computer (SGI, Mountain View, CA) sent triggering signals to the scanner and generated the visual stimulus that was synchronized to this scanner. Trigger signals were also sent to the SynAmps to tag the stimulus events for subsequent binning, temporal epoching and averaging of EEG data into the relevant EP averages according to stimulus type and experimental condition. The electrode positions were digitized using a Fastrack 3D digitizer (Polhemus, Colchester, VT). Before applying the linear estimation algorithm, we discarded 3 to 5 noisy channels based on visual inspection. The EEG window had an ISI of 125 ms for subject NH and 250 ms for subject DS, 1,200 epochs were collected for each subject.

Visual Stimuli: Each epoch of the visual stimulus consisted 15 seconds of a full-field reversing checkerboard pattern (4-8 Hz frequency) followed by 15 seconds of uniform gray field. In all conditions, a central fixation spot was present. The 10×10 black and white checkerboard pattern was rear-projected by a color LCD projector, through a collimating lens onto an acrylic screen (visual field 40° × 25°) degrees. The screen was positioned inside the magnet, immediately below the subject's jaw. A mirror was interposed between, and oriented approximately 45 degrees to the screen and the subject's line of sight.

Forward Solution: We used a realistic boundary element method (BEM) for calculating the EEG forward solution (19, 20). The EEG forward solution computation requires the conductivity boundaries (inner skull boundary, outer skull boundary, and outer skin boundary), the relative conductivities for each region, the locations of all possible sources, and the EEG electrode locations. All surfaces are automatically reconstructed structural MRI acquisition using a previously described technique (21-23). 642 vertices represent each conductivity boundary. Typically, the cortical surface is initially tessellated with about 150,000 vertices per hemisphere. This representation of the cortical surface is used for display. For the inverse computation, the cortical surface is decimated to approximately 3000 dipoles per hemisphere, which is roughly equivalent to 1 dipole every 10 mm along the cortical surface. We used a conductivity ratios for brain:skull:scalp of 1:80:1.

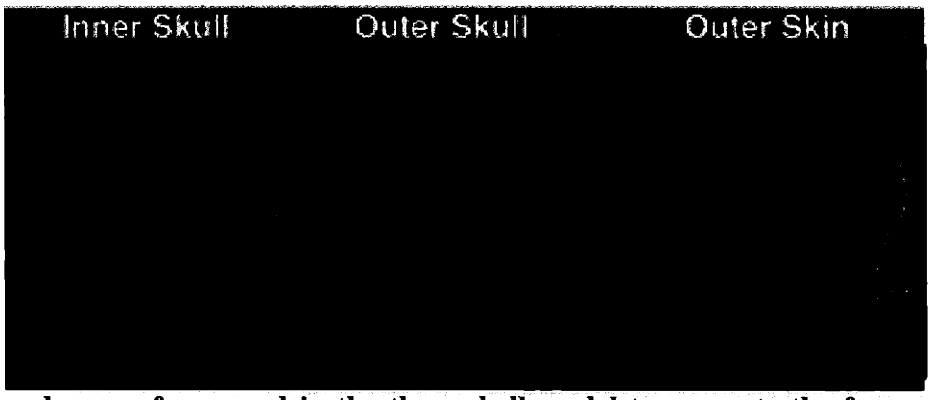

Fig. 4: Boundary surfaces used in the three-shell model to compute the forward solution based on BEM (Subject NH).

Inverse Solutions:

We used the linear estimation approach (23-28) to localized the brain activity for EEG data alone and for fMRI constrained EEG (fEEG). We computed an optimal linear inverse operator (**W**), which maps the external electromagnetic field measurements (**x**) into estimated source activities ($\hat{\mathbf{s}}$) within the brain. This inverse operator explicitly minimizes the expected error between the estimated and actual activity distribution (**s**). The calculation incorporates the forward solution (**A**), *a priori* spatial constraints (**R**) and sensor noise characteristics (**C**). We constrained the source locations, but not the source orientations, by the cortical surface. The expression for the inverse operator is:

$$\mathbf{W} = \mathbf{R}\mathbf{A}^{\mathsf{T}}\left(\mathbf{A}\mathbf{R}\mathbf{A}^{\mathsf{T}} + \mathbf{C}\right)^{-1} \qquad (1)$$

This linear inverse operator provides an estimate of source activity for each time point independently of the other time points. Then, the estimated source activities are given by the simple expression:

$$\hat{\mathbf{s}} = \mathbf{W}\mathbf{x} \qquad (2)$$

When analyzing the EEG data alone, we have no prior spatial information, and thus the **R** matrix is the identity matrix. For the fMRI-constrained solution, the **R** matrix is constructed as follows: each fMRI location on the cortex that is activated, according to the result of cluster analysis (18), is set to 1 and the other locations are set to 0.01. These values correspond to a relative fMRI weighting of 90%, and provide robustness of the solution in the face of mis-specifications of the fMRI (29).

Representation of the results: For display of both the fMRI and the EEG localization results we used the reconstructed pial surface. The cortical surface reconstruction is described in detail in (21-23, 30).

7.4 Results

For both subjects, we were able to record both evoked potentials and fMRI, and to use those measurements for localization of the cortical activity. A typical subset of the bipolar evoked potential measurements is shown in **Fig.** 5A. In both subjects there were two peaks of activity. The variance of the signal for one bipolar channel (channel 32, in the occipital lobe) is shown in **Fig.** 5B. The spatial distribution of the scalp

potentials was typical of evoked potentials of visual stimuli, where the maximum voltage swings are measured in the occipital region (**Fig.** 6).

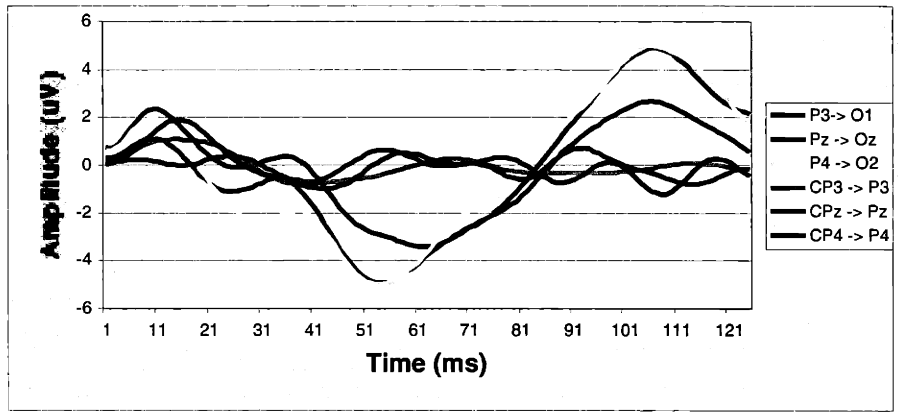

(A)

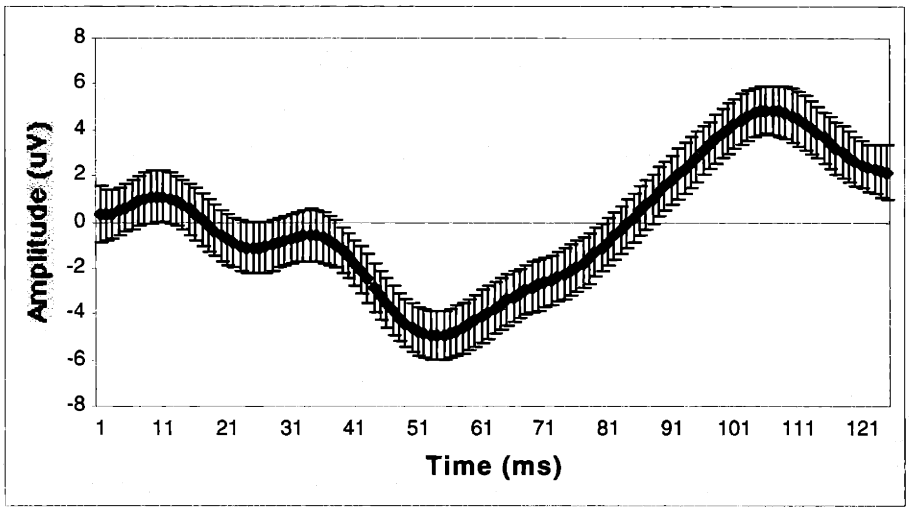

(B)

Fig. 5: (A) Evoked potentials collected from subject NH, positive in the upward direction, collected during fMRI. (B) **Average ± variance of the bipolar recording in channel Pz->Oz.**

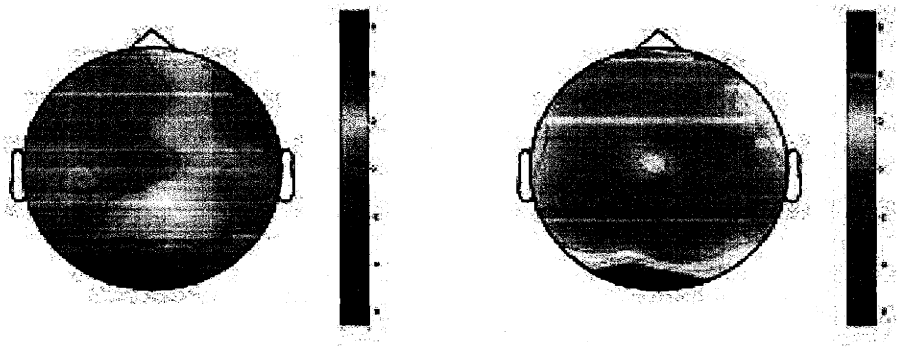

Fig. 6: Evoked potentials collected from Subject NH, during simultaneous EEG/fMRI. Potentials are displayed in μV units.

The simultaneously collected fMRI results (Z scores) are displayed on the medial aspect of the pial surface in **Fig.** 7A. For subject DS we present the left hemisphere

and for subject NH we present right hemisphere. The fMRI activity was consistently localized to the posterior portion of the calcarine sulcus. The Talairach coordinates of the fMRI activity are given in Table 1.

Subject	X	Y	Z
NH (left hemisphere)	-10.8	-78.5	-13.6
NH (right hemisphere)	6.7	-86.8	0.4
DS (left hemisphere)	10.8	-86.1	-2.6
DS (right hemisphere)	-7.3	-82.1	-6.1

Table 1: Talaraich center of mass coordinates for the functional MRI activations of the two subjects

Using the EEG measurements alone, we used the linear estimation approach to localize the cortical generators of the scalp EEG (**Fig.** 6B). In both subjects, the cortical activity was localized along the entire length of the calcarine sulcus. For subject DS the activity was primarily on the lower bank, whereas for subject NH the activity encompassed both upper and lower banks. For each subject, the EEG localization was similar in location to the fMRI results, but was larger in extent.

The fMRI constrained EEG localization results are shown in **Fig.** 7C. For both subjects the localizations are similar to the fMRI results and considerably more focal than the unconstrained EEG localizations. For subject DS the two peaks of activity occurred at 53 ms and 106 ms. For subject NH the first peak had a latency of 63 ms and the second, 111 ms.

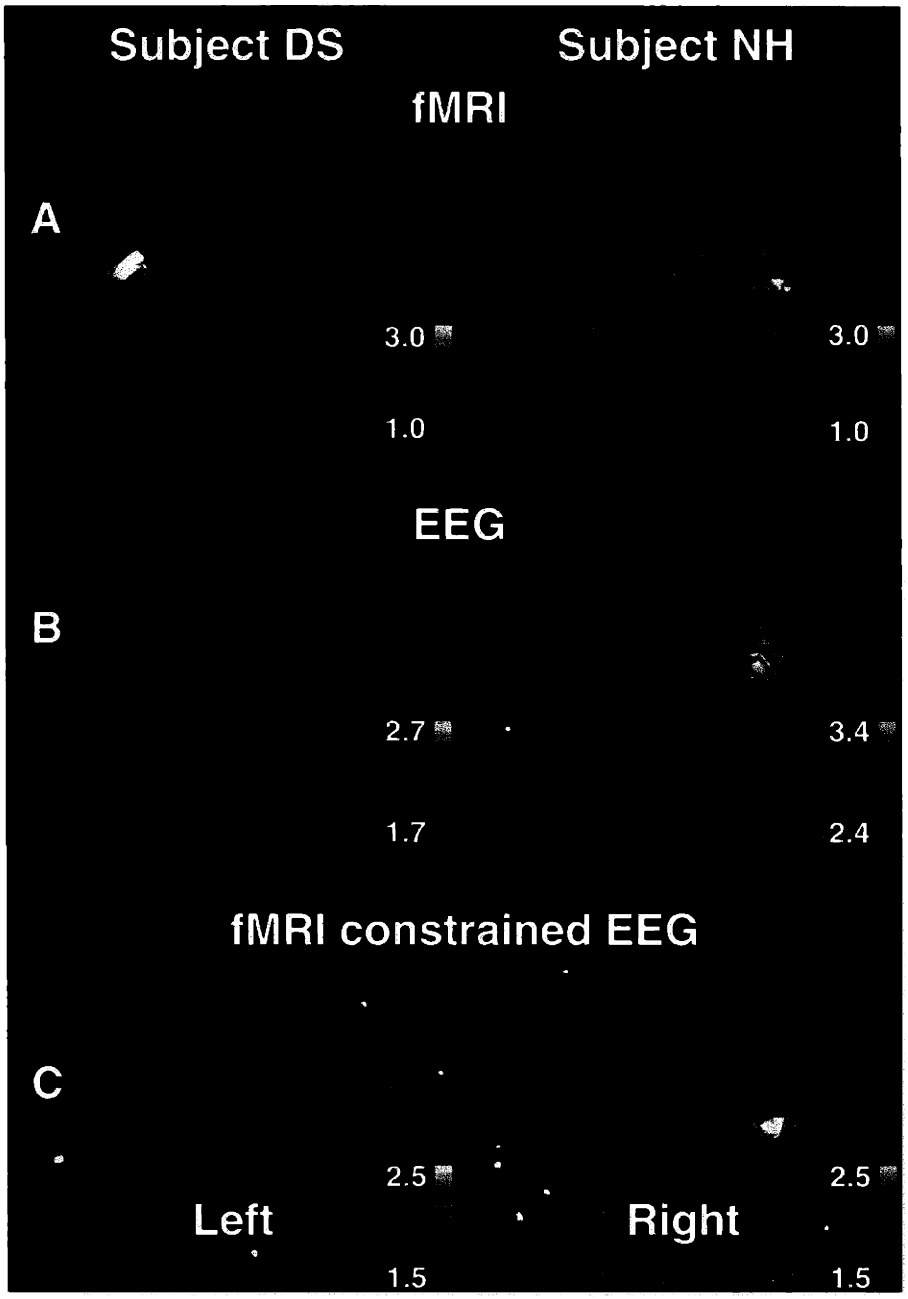

Fig. 7: Spatial localization of the fMRI (A), EEG alone (B), and fMRI constrained EEG (fEEG) (C). The activity is displayed on the medial aspect of the pial surface of the left (Subject DS) and right (Subject NH) hemispheres.

Seven snapshots of the cortical activity movie, without and with fMRI constraint, are shown for Subject NH in **Fig.** 8. The peaks of activity occur at the same time for both the EEG (alone) localization and the fMRI constrained localization. One can again see that the spatial extent of the fMRI constrained EEG localization is more focal than the results based on EEG measurements alone.

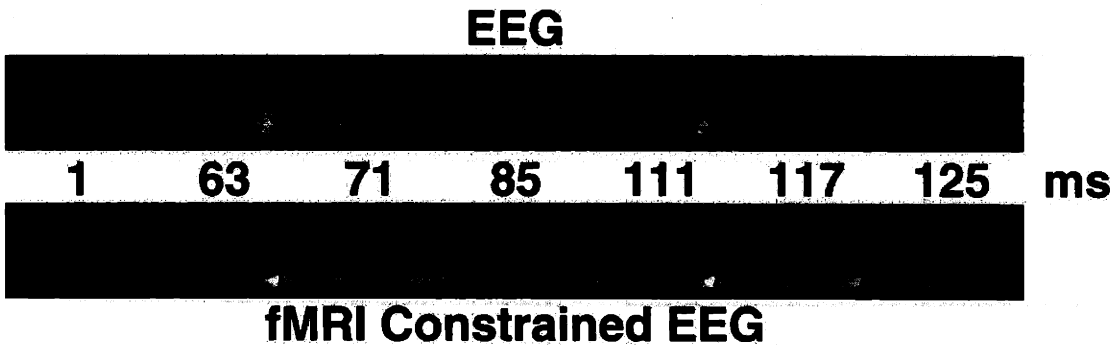

Fig. 8: Movie of the cortical activity for the subject NH showing the activations of the occipital region of the neocortex during the flashing checkerboard task. The upper row contains localizations for EEG alone. The bottom row show localizations for fMRI constrained EEG (fEEG).

7.5 Discussion

Using our state of the art hardware and software, we simultaneously recorded and localized the hemodynamic and electric response of the brain to the exact same visual stimulus. We found good agreement between independently analyzed fMRI and the EEG localization results, consistent with the theory that there is coupling between neuronal activity and hemodynamic change (31). As expected from model studies (29), the combined analysis of the fMRI and EEG characterized the cortical generators with higher spatiotemporal resolution than either technique alone.

This work represents a significant advancement over previous work. Previous simultaneous EEG/fMRI studies recorded interictal activity, which has peak potentials well over 50 μV and is visible in the spontaneous EEG recordings. These studies, however, utilized the EEG only to manually trigger the fMRI. We were able to make measurements of the much smaller evoked potentials that cannot be seen in unaveraged recordings. These evoked potentials were of sufficient quality to allow actual cortical source localization, not just as a trigger for functional acquisitions. Finally, the inverse approach we used allowed a principled combination of the fMRI and EEG data. We were not required to make any manual selection of dipole locations from the fMRI data.

However, there were some limitations to this technique. Primarily, the low SNR of both the fMRI and EEG would limit the range of applications. For example, currently we would be unable to study cognitive paradigms that do not generate relatively large changes in hemodynamics or evoked potentials. The SNR of both the fMRI and EEG measurements were low mainly because of motion of the subjects. This subject motion was primarily caused by discomfort from the EEG cap (as reported by all subjects), given that the EEG electrodes were mounted on protruding plastic cups. In this 32-channel EEG cap only three occipital electrodes supported the whole weight of the subject's head. Additionally the EEG was corrupted by noise due to other types of motion (e.g. due to breathing and heartbeat) of the closed loops that are formed by EEG electrodes, leads and skin. The motion of conductors inside a magnetic field will induce a potential (i.e. noise) in those conductors.

We are planning to address these limitations in future studies. The cap comfort can be improved by reducing the profile of the electrodes and increasing the cap's padding. We are considering adaptive filtering to further improve the SNR of the EEG bipolar recordings during fMRI. Furthermore, we are developing the next generation of EEG amplifiers for simultaneous recordings with higher common mode rejection ratio to improve the SNR of bipolar recordings. This improved amplifier will also include zero transient time that will allow more efficient use of experiment time.

We have demonstrated that it is possible to simultaneously collect EEG and fMRI, with high enough quality to allow for combined modality source localization. This work represents a significant advancement over previous work, both in terms of the hardware used to collect the simultaneous measurements and the use of a principled multimodality inverse approach. Further improvements in these technologies will provide an optimal tool to non-invasively investigate the spatiotemporal dynamics of human brain activity.

7.6 References

1. Belliveau JW, Kennedy DN, McKinstry RC, Buchbinder BR, Weisskoff RM, Cohen MS, Vevea JM, Brady TJ, and Rosen BR. Functional mapping of the human visual cortex by magnetic resonance imaging. *Science*. 1991; 254: 716-719.
2. Kwong KK, Belliveau JW, Chesler DA, Goldberg IE, Weisskoff RM, Poncelet BP, Kennedy DN, Hoppel BE, Cohen MS, Turner R, Cheng HM, Brady TJ, and Rosen BR. Dynamic magnetic resonance imaging of human brain activity during primary sensory stimulation. *Proc. Natl. Acad. Sci. USA*. 1992; 89: 5675-5679.
3. Ogawa S, Tank DW, Menon R, Ellermann JM, Kim S-G, Merkle H, and Ugurbil K. Intrinsic signal changes accompanying sensory stimulation: Functional brain mapping with magnetic resonance imaging. *Proc. Natl. Acad. Sci. USA*. 1992; 89: 5951-5955.
4. Regan D. *Human brain electrophysiology: Evoked potentials and evoked magnetic fields in science and medicine*. New York: Elsevier, 1989: 415.
5. Moonen CTW and Bandettini PA. *Functional MRI*. New York, N. J.: Springer-Verlag, 1999:
6. Warach S, Ives JR, Schlaug G, Patel MR, Darby DG, Thangaraj V, Edelman RR, and Schomer DL. EEG-triggered echo-planar functional MRI in epilepsy. *Neurology*. 1996; 47: 89-93.
7. Krakow K, Woermann FG, Symms MR, Allen PJ, Barker GJ, Duncan JS, and Fish DR. EEG-triggered functional MRI of interictal epileptiform activity in patients with partial seizures. *Brain*. 1999; 122: 1679-1688.
8. Ives JR, Warach S, Schmitt F, Edelman RR, and Schomer DL. Monitoring the patient's EEG during echo-planar MRI. *Electroenceph. Clin. Neurophysiol.* 1993; 87: 417-420.
9. Heinze HJ, Hinrichs H, Scholz M, Burchert W, and Mangun GR. Neural mechanisms of global and local processing. A combined PET and ERP study. *J. Cogn. Neurosci.* 1998; 10: 485-498.

10. Heinze HJ, Mangun GR, Burchert W, Hinrichs H, Scholz M, Munte TF, Gos A, Scherg M, Johannes S, Hundeshagen H, and et al. Combined spatial and temporal imaging of brain activity during visual selective attention in humans. *Nature*. 1994; 372: 543-546.
11. Opitz B, Mecklinger A, Von Cramon DY, and Kruggel F. Combining electrophysiological and hemodynamic measures of the auditory oddball. *Psychophysiology*. 1999; 36: 142-7.
12. Ahlfors SP, Simpson GV, Dale AM, Belliveau JW, Liu AK, Korvenoja A, Virtanen J, Huotilainen M, Tootell RB, Aronen HJ, and Ilmoniemi RJ. Spatiotemporal activity of a cortical network for processing visual motion revealed by MEG and fMRI. *J Neurophysiol*. 1999; 82: 2545-55.
13. Korvenoja A, Huttunen J, Salli E, Pohjonen H, Martinkauppi S, Palva JM, Lauronen L, Virtanen J, Ilmoniemi RJ, and Aronen HJ. Activation of multiple cortical areas in response to somatosensory stimulation: combined magnetoencephalographic and functional magnetic resonance imaging. *Hum Brain Mapp*. 1999; 8: 13-27.
14. Morioka T, Mizushima A, Yamamoto T, Tobimatsu S, Matsumoto S, Hasuo K, Fujii K, and Fukui M. Functional mapping of the sensorimotor cortex: combined use of magnetoencephalography, functional MRI, and motor evoked potentials. *Neuroradialogy*. 1995; 37: 526-530.
15. Luck SJ. Direct and indirect integration of event-related potentials, functional magnetic resonance images, and single-unit recordings. *Hum Brain Mapp*. 1999; 8: 115-201.
16. Lamusuo S, Forss N, Ruottinen HM, Bergman J, Makela JP, Mervaala E, Solin O, Rinne JK, Ruotsalainen U, Ylinen A, Vapalahti M, Hari R, and Rinne JO. [18F]FDG-PET and whole-scalp MEG localization of epileptogenic cortex. *Epilepsia*. 1999; 40: 921-30.
17. Ernst RR, Bodenhausen G, and Wokaun A. *Principles of Nuclear Magnetic Resonance in One and Two Dimensions*. Oxford: Oxford Univ Press, 1990:
18. Friston KJ, Jezzard P, and Turner R. Analysis of functional MRI time series. *Human Brain Mapping*. 1994; 1: 153-171.
19. de Munck JC. A linear discretization of the volume conductor boundary integral equation using analytically integrated elements. *IEEE Trans. Biomed. Eng*. 1992; 39: 986-990.
20. Oostendorp TF and van Oosterom A. Source parameter estimation using realistic geometry in bioelectricity and biomagnetism. In: Nenonen J, Rajala HM, and Katila T, eds. *Biomagnetic Localization and 3D Modeling, Report TKK-F-A689*. Helsinki: Helsinki University of Technology, 1992:
21. Dale AM, Fischl B, and Sereno MI. Cortical Surface-Based Analysis I: Segmentation and Surface Reconstruction. *NeuroImage*. 1999; 9: 179-194.
22. Fischl B, Sereno MI, and Dale AM. Cortical Surface-Based Analysis II: Inflation, Flattening, and a Surface-Based Coordinate System. *NeuroImage*. 1999; 9: 195-207.

23. Dale AM and Sereno MI. Improved localization of cortical activity by combining EEG and MEG with MRI cortical surface reconstruction: A linear approach. *J. Cog. Neurosci.* 1993; 5: 162-176.
24. Liu AK, Belliveau JW, and Dale AM. Spatiotemporal imaging of human brain activity using functional MRI constrained magnetoencephalography data: Monte Carlo simulations. *Proc Natl Acad Sci U S A.* 1998; 95: 8945-50.
25. Hamalainen M, Hari R, Ilmoniemi RJ, Knuutila J, and Lounasmaa OV. Magnetoencephalography - theory, instrumentation, and application to noninvasive studies of the working human brain. *Review of Modern Physics.* 1993; 65: 413-497.
26. Wang JZ, Williamson SJ, and Kaufman L. Magnetic source images determined by a lead-field analysis: the unique minimum-norm least-squares estimation. *IEEE Trans Biomed Eng.* 1992; 39: 665-75.
27. Sarvas J. Basic mathematical and electromagnetic concepts of the biomagnetic inverse problem. *Phys Med Biol.* 1987; 32: 11-22.
28. Hamalainen MS and Ilmoniemi RJ. *Interpreting measured magnetic fields of the brain: estimates of current distributions.* Helsinki, Finland: Helsinki Univ. of Technology, 1984:
29. Liu AK, Belliveau JW, and Dale AM. Spatiotemporal imaging of human brain activity using fMRI constrained MEG data: Monte Carlo simulations. *Proc. Natl. Acad. Sci. USA.* 1998; 95: 8945-8950.
30. Sereno MI, Dale AM, Reppas JB, Kwong KK, Belliveau JW, Brady TJ, Rosen BR, and Tootell RBH. Borders of multiple visual areas in humans revealed by functional magnetic resonance imaging. *Science.* 1995; 268: 889-893.
31. Grinvald A, Slovin H, and Vanzetta I. Non-invasive visualization of cortical columns by fMRI. *Nat Neurosci.* 2000; 3: 105-107.

8. fMRI constrained MEG – Visual motion

8.1 Abstract

Neuroimaging studies have demonstrated the existence of several distinct cortical areas involved in the processing of visual motion. Here, we used a novel method for combining fMRI and MEG data to study the temporal interactions of areas responsible for the processing of coherent versus incoherent motion. The onset of coherent and incoherent motion evoked a complex sequence of activation within the different visual areas. The amplitude of the response in the middle temporal area ("MT+") was not strongly modulated by coherence. However, an area in the parietal occipital sulcus ("SPO") exhibited a 30% larger response to coherent stimuli, peaking at 175 ms post-stimulus. In both MT+ and SPO, this peak response was 20 - 30 ms earlier for coherent stimuli compared to incoherent stimuli. These data support the view that neural changes in both amplitude and timing within a cortical network underlie the perception of particular stimulus attributes, in agreement with theoretical predictions.

8.2 Introduction

The cerebral cortex processes information via neural networks, which are subdivided into anatomically and functionally differing areas. The numerous interconnections between neurons in different areas suggest that multiple areas interact in the course of stimulus processing. The use of fMRI makes is possible to localize "where" processing steps occur in the brain with high spatial resolution. The next question to address is "how" processing occurs in the brain. A crucial step towards answering the "how" question is the characterizations of the temporal interactions of the relevant cortical areas determined by functional imaging. A given network of brain areas can give rise to many functional operations through different temporal patterns of interactions between areas. Thus, understanding cortical information processing requires investigation of the functional properties of each area and the dynamic patterns of activity in networks of areas.

Motion is one of the most prominent and fundamental properties of our visual world. Perception of coherent motion is essential to distinguish different classes of moving objects and self motion, yet relatively little is known about the spatial and temporal patterns of human cortical activity underlying motion processing in human cortex. Area MT+ is a well-studied, cortical region that is selective for visual motion. MT+ is an especially relevant area for study in humans since in monkeys, MT is a magnocellular-dominated signature area in the cortical network that processes motion (dorsal pathway).

In humans, PET and fMRI have demonstrated the motion selectivity of area MT+ (1-6). Here, we have further refined the motion stimulus to examine the differential response to coherent and incoherent dot motion.

8.3 Methods

Four subjects viewed two types of rotation/dilation random dot flow field stimuli. In one condition (coherent motion), each dot moved as part of the same flow field, while in the other condition (incoherent motion), each dot moved independently but with the same local statistics.

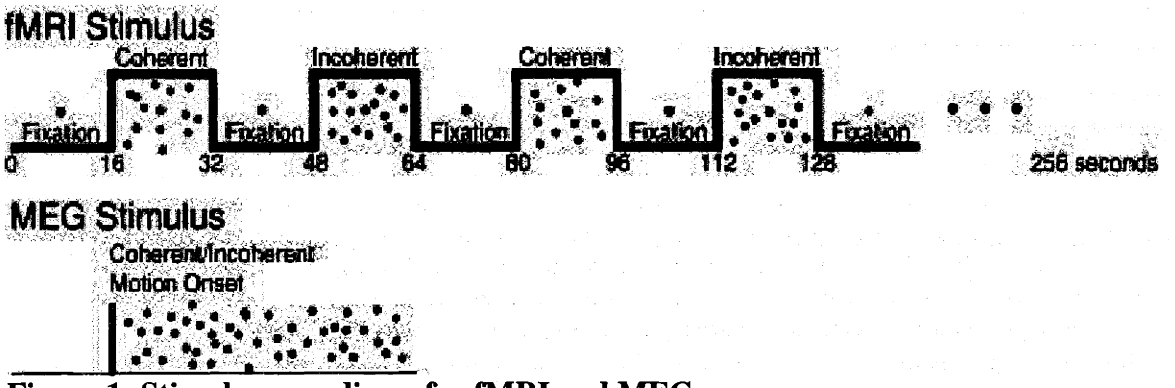

Figure 1: Stimulus paradigms for fMRI and MEG.

The fMRI stimulus consisted of alternating periods of motion (coherent or incoherent) with fixation only. In all conditions, the subject was instructed to fixate on a central point. In each fMRI run, there were 4 blocks of coherent motion, 4 blocks of incoherent motion and 8 blocks of fixation. 7 separate fMRI runs were collected and averaged. fMRI data were acquired from 24 7mm-thick horizontal slices with 3mm x 3mm in-plane resolution, sampling the entire brain using an ASE sequence with TE/tau offset = 70ms/-25ms.

The MEG stimulus consisted of a stationary dot field followed by either coherent or incoherent dot motion. The MEG data were recorded with a whole-head 122-channel dc-SQUID device (Neuromag, Helsinki Finland). The MEG acquisition was timelocked to the onset of motion. For each subject, approximately 500 blink free epochs were averaged, extending from 200 ms before to 800 ms after the onset of motion. The analog filter passband was 0.03–100 Hz and the sampling frequency 397 Hz. The averaged responses were low-pass filtered at 40 Hz, and the zero level was adjusted to the average pre-stimulus baseline of –100 to 0 ms.

The timecourse of electrical activity for each point on the cortical surface was estimated using an anatomically and fMRI constrained linear estimation approach (7, 8). We refer to this approach as "fMEG" for **f**unctionally constrained **MEG**. Modeling studies have shown that when using the fMRI constraint, extra sources are much less problematic than missing sources (8). Therefore, we used the spatial pattern of activity from the coherent motion condition, which provides the largest spatial estimate of activity, in the combined fMRI/MEG spatiotemporal estimation of cortical activity.

8.4 Results

We found that area MT+ responded well to both coherent and incoherent motion, with a slightly more robust response to coherent motion. In addition, the fMRI results revealed a visual area located in the parieto-occipital sulcus ("SPO") which was preferentially activated by coherent motion. The average Talairach coordinates for MT+

in this study (36, -60, 1), were reasonably close to that reported in a previous fMRI study (45, -76, 3) (5). The average Talairach coordinates for SPO were (14, -86, 18). The fMRI data reveals that area SPO is more strongly activated by coherent than incoherent stimuli.

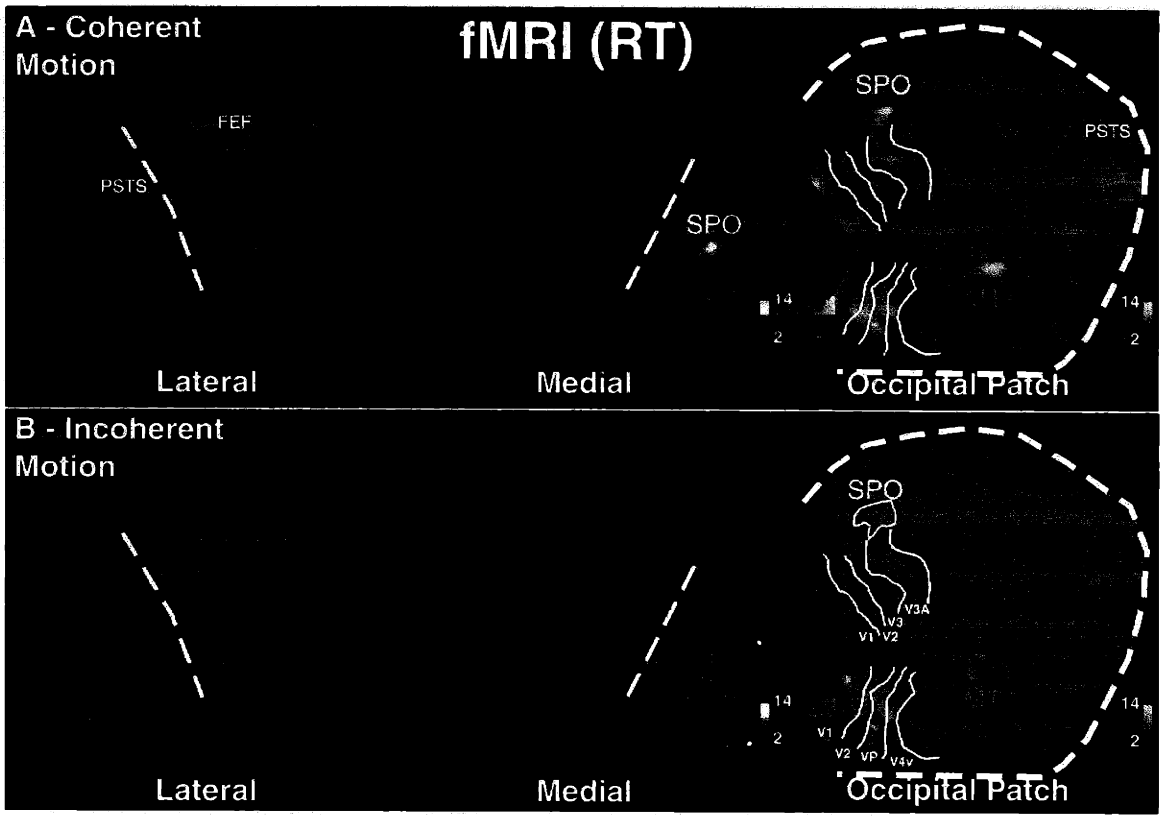

Figure 2: Functional MRI localization of coherent motion versus a stationary dot pattern (A) and incoherent dot motion versus a stationary dot pattern (B). The statistical maps of activation are displayed on the lateral and medial aspects of the inflated cortical surface (left) and the flattened occipital cortex (right). Sulci are shown as dark grey, and gyri are shown as light gray. The cortical inflation and flattening procedures are described in (7, 9, 10).

Numerous retinotopic visual areas also responded preferentially to the visual motion. These areas included the extrafoveal representations of V1, V2, V3, V3a, V4v. The data from one subject for coherent and incoherent motion is shown in Figure 2. Additional activation in this individual was seen in the vicinity of frontal eye field (FEF) and the posterior end of the superior temporal sulcus (PSTS). However, these two more anterior activations were not consistent across the individuals. Comparing the two motion conditions shows that the areas activated by incoherent motion are a subset of those areas activated by incoherent motion. This is exemplified by area SPO, which is strongly activated in the coherent condition, but is not activated in the incoherent condition. This finding, along with the response of area MT+, were found in all four subjects. Subsequently, we have focused our attention on these two components of the motion processing network.

In order to clarify the temporal dynamics of MT+ and SPO, we also tested the same subjects using the same visual stimuli with MEG. Four snapshots of the cortical response to coherent motion are shown in Figure 3. One can clearly see that the peak activity in area MT+ (150 ms) precedes the peak activity in area SPO (185 ms).

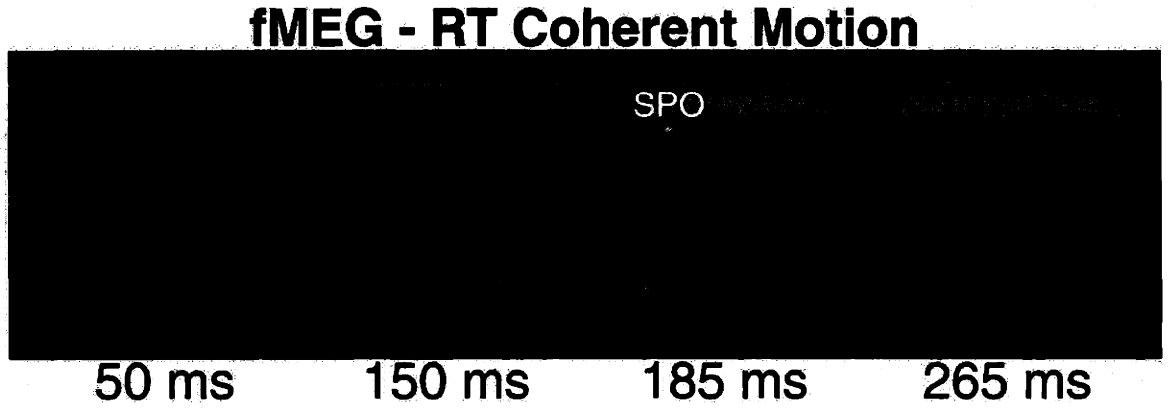

Figure 3: The fMEG localizations are displayed on the flattened occipital cortex at four different timepoints.

Using the fMEG data (n=4), we were able to investigate systematic changes in network timing. For each subject, representative timecourses from areas MT+ and SPO were normalized within each area, relative to the peak of activity to coherent motion. These normalized time courses were then averaged across all four subjects. The mean for peak amplitudes and latencies are shown in Table 1. The average timecourses (for all four subjects) for areas MT+ and SPO are shown in Figure 4.

	MT+		SPO	
	Coherent	**Incoherent**	**Coherent**	**Incoherent**
Normalized Amplitude	1.00	.93 ± .04	1.00	.67 ± .11*
Latency (ms)	143 ± 9	170 ± 4*	175 ± 2	194 ± 2*
				* indicates p < 0.05

Table 1: Average ± standard error of normalized peak amplitudes and latencies for areas MT+ and SPO. For each subject, the timecourses were separately normalized for each area such that the peak of activity to coherent motion was normalized to 1.0.

For both coherent and incoherent motion conditions, the peak activity in area MT+ preceded the peak activity for area SPO by ~30 ms (compare solid blue to solid red, or graded blue to graded red). Examining the effect of the motion type for each area, we found the peak latencies in MT+ were ~30 ms earlier for coherent than incoherent stimuli (compare solid blue to graded blue, or solid red to graded red). There is also a small modulation in amplitude between motion conditions, with larger responses to coherent motion. The amplitude modulation of ~30% was largest for area SPO.

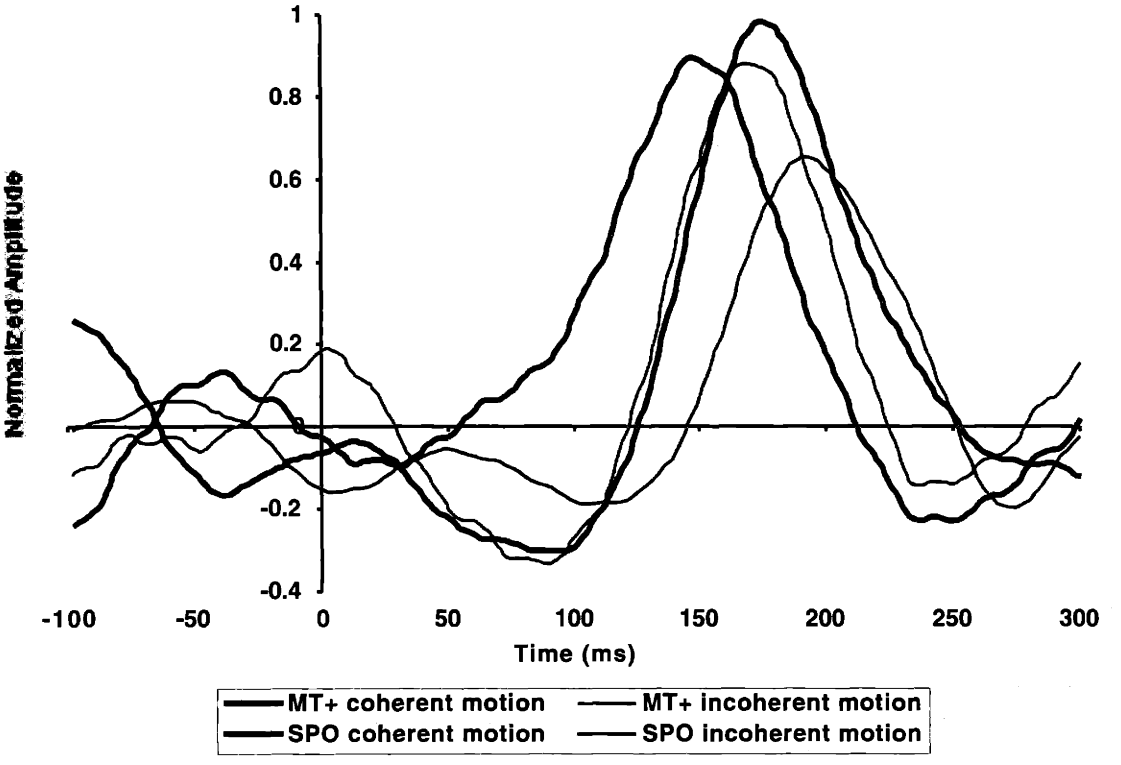

Figure 4: The normalized fMEG timecourses for areas MT+ and SPO were averaged across all four subjects. The timecourses for each area were normalized so that the peak activity in that area for coherent motion was 1.0. The activity for areas MT+ and SPO are shown in blue and red, respectively. The type of motion is indicated as solid (coherent motion) or graded (incoherent motion).

8.5 Discussion

The fMRI modulation seen in these two areas under these two motion conditions suggests that the same cortical network, involving MT+ and SPO, is used to process both coherent and incoherent motion stimuli. The timing data suggest that coherent motion processing proceeds from MT+ to SPO. Thus, although the cortical areas that underlie the processing of visual motion were similar, the activity and timing of the cortical network was stimuli dependent.

The similar response of MT+ to coherent and incoherent motion, and the larger response of SPO to coherent motion suggest that MT+ computes the coherence of motion and sends this information to SPO. If MT+ processes "local" motion (i.e. motion on a finer spatial scale), one would expect to see responses of similar amplitude to these two motion stimuli. In both cases, there was approximately the same amount of local motion. The output of MT+ thus depended on the coherency of that motion, and the "calculation" depended on the spatial correlation of the motion.

SPO prefers globally coherent motion. During such motion, larger spatial regions must be sampled to determine if the individual local motions are "correlated" in some way (e.g., all moving in the same vector field). The hypothesis of large receptive fields in SPO is consistent with the large ipsilateral visual field represented in this region of

cortex (11). Under this assumption, SPO would show larger activity to coherent motion than incoherent motion.

These hypotheses about this cortical network (MT+ and SPO) that processes visual motion required both spatial and temporal data that was provided by the fMEG method. This integrated multimodality imaging approach will allow the further development and characterization of the neural processing of visual motion. In fact, this technique is generally applicable to the study of other sensory, motor and cognitive paradigms.

8.6 References

1. Corbetta M, Miezin FM, Dobmeyer S, Shulman GL, and Petersen SE. Attentional modulation of neural processing of shape, color, and velocity in humans. *Science.* 1990; 248: 1556-9.
2. Watson JD, Myers R, Frackowiak RS, Hajnal JV, Woods RP, Mazziotta JC, Shipp S, and Zeki S. Area V5 of the human brain: evidence from a combined study using positron emission tomography and magnetic resonance imaging. *Cerebral Cortex.* 1993; 3: 79-94.
3. Zeki S, Watson JD, Lueck CJ, Friston KJ, Kennard C, and Frackowiak RS. A direct demonstration of functional specialization in human visual cortex. *J Neurosci.* 1991; 11: 641-9.
4. Tootell RBH, Kwong KK, Belliveau JW, Baker JR, Stern CS, Savoy RL, Breiter H, Born R, Benson R, Brady TJ, and Rosen BR. Functional MRI (fMRI) Evidence for MT/V5 and Associated Visual Cortical Areas in Man. In: *Proceedings of the Society for Neuroscience 23rd Annual Meeting, Washington, D.C., 1993.* Soc. Neuro., Wash D.C. 1500.
5. Tootell RBH, Reppas JB, Kwong KK, Malach R, Born RT, Brady TJ, Rosen BR, and Belliveau JW. Functional analysis of human MT and related visual cortical areas using magnetic resonance imaging. *J. Neuroscience.* 1995; 15(4): 3215-3230.
6. Tootell RBH, Mendola JD, Hadjikhani NK, Ledden PJ, Liu AK, Reppas JB, Sereno MI, and Dale AM. Functional analysis of V3A and related areas in human visual cortex. *J Neuroscience.* 1997; 17: 7060-7078.
7. Dale AM and Sereno MI. Improved localization of cortical activity by combining EEG and MEG with MRI cortical surface reconstruction: A linear approach. *J. Cog. Neurosci.* 1993; 5: 162-176.
8. Liu AK, Belliveau JW, and Dale AM. Spatiotemporal imaging of human brain activity using fMRI constrained MEG data: Monte Carlo simulations. *Proc. Natl. Acad. Sci. USA.* 1998; 95: 8945-8950.
9. Dale AM, Fischl B, and Sereno MI. Cortical Surface-Based Analysis I: Segmentation and Surface Reconstruction. *NeuroImage.* 1999; 9: 179-194.
10. Fischl B, Sereno MI, and Dale AM. Cortical surface-based analysis. II: Inflation, flattening, and a surface-based coordinate system. *Neuroimage.* 1999; 9: 195-207.
11. Tootell RBH, Mendola JD, Hadjikhani NK, Liu AK, and Dale AM. The representation of the ipsilateral visual field in human cerebral cortex. *Proc. Natl. Acad. Sci.* 1998; 95: 818-824.

9. MEG Localization of Interictal Spikes

9.1 Introduction

"No one can admit more fully than I do the difficulties in the localization of 'discharging lesions' ... I still urge that we should go on trying to localize." John Hughling Jackson, 1873.

Epilepsy is a relatively prevalent disorder, affecting nearly 2 million in the USA alone (1). The primary clinical finding is that of recurrent seizures. The most common therapy uses various antiepileptic drugs (AEDs). AEDs provide good control of seizure activity in approximately 80% of patients (2). However, the remaining patients continue to have seizures, in spite of multiple medications. It is estimated that half of these patients (approximately 200,000) who are medically refractory could be candidates for surgery (3). For certain types of epilepsy, the response to surgery is excellent. Nearly 70% of patients with medically refractory temporal lobe epilepsy who received either an anterior temporal lobectomy or an amygdalohippocampectomy were free of seizures for at least two years post-operatively (4).

The results of the surgical resection depend upon the quality of the presurgical workup. This evaluation is a complicated process, whose main goal is "the identification of the epileptogenic zone, namely the areas of the brain that is necessary and sufficient for habitual seizure generation, and whose removal or disconnection will effect a cure (5)." Typically, the presurgical evaluation will include interictal and ictal scalp EEG, imaging studies looking for structural abnormalities (MRI) or functional deficits (SPECT or PET), neuropsychological testing, and invasive EEG measurements (e.g. subdural electrodes, depth electrodes, intraoperative electrocorticography) (6).

A promising additional to the commonly used non-invasive presurgical studies is interictal magnetoencephalograpy (MEG). The first MEG measurements of epileptic activity were made nearly three decades ago (7). Then came the early attempts at some basic type of localization using single channel MEG data (8-11). Since then significant progress has been made towards using MEG measurements for the localization of epileptic foci. Numerous groups have demonstrated the ability of multichannel MEG to provide useful non-invasive localization data for use in presurgical planning. The majority of the published MEG localization of epilepsy have compared the MEG results to invasive recordings, e.g. (12-27). Others compared the MEG results with anatomic abnormalities, clinical findings, functional imaging, surgical outcome or other data (24, 28-33). MEG has also been used in the pediatric patient with abnormal seizure activity, e.g. (34-38).

Our work seeks to build upon the existing foundation of MEG localization in epilepsy. The techniques we present here have a few advantages over many of the previous studies. Our first advantage is the use of a realistic head model. Using the boundary element method, we are able to more accurately represent the tissue conductivity boundaries than a spherical model. In addition to the geometry, we have an explicit representation of the cortical surface. This allows us to constrain our estimates of cortical activity by the location and orientation of cortex. Finally, we are

utilizing a linear estimation approach, instead of the dipole fitting approach used by the most of the above work. The linear estimation approach is insensitive to multiple temporally overlapping sources, which should provide a more accurate description of the propagation of activity. However, we note that while the linear estimation approach may provide accurate representations of extended sources, it does not provide very focal localizations of focal sources. The interictal activity, while initially quite focal, may quickly encompass larger regions of cortex. Also, the extended nature of the localization may be less problematic when MEG results are used to guide the placement of more invasive recordings, since those invasive devices will cover relatively large regions of cortex compared to any focal localization.

9.2 Methods

We analyzed spontaneous interictal spikes from three patients with intractable partial complex epilepsy. Data for two patients was collected at the Center for Advanced Medical Technologies (CAMT), Salt Lake City, Utah. Data for the third patient was collected at CHR PontChaillou, Rennes, France. The analysis performed here used short (2 - 3 second) windows centered around interictal spikes. In addition to MEG measurements, high resolution structural MRI was also performed on each patient. The anatomic data was used for reconstruction of the forward model and for visualization of the localization results.

9.2.1 Patient Data

Patient 1 (TL): Patient 1 is a 22 year old male, with a history of partial seizures since age 7. Non-invasive data for Patient 1 were collected at the CAMT. 10 interictal spikes were analyzed. Invasive recordings and the surgical resection were performed Stanford University Medical Center (Stanford, CA).

Patient 2 (CS): Patient 2 is a 22 year old male, with a history of intractable complex partial and secondary generalized seizures starting at the age of 8 years. Non-invasive data for Patient 2 were collected at the CAMT. 30 interictal spikes were analyzed.

Patient 3 (VVG11): Patient 3 is a 21 year old male, with a 5 year history of complex partial epilepsy. All data for Patient 3 was collected at CHR PontChaillou. 22 interictal spikes were analyzed.

9.2.2 MEG

For patients from the Center for Advanced Medical Technologies (CAMT), measurements were acquired using a whole head 122 channel biomagnetometer (NeuroMag, Helsinki, Finland). For patients from Rennes, data were collected using a 37 channel biomagnetometer (BTi, San Diego). Since the 37 channel system only covered a portion of the head, during the MEG data acquisition the system was moved to various locations around the head of the patient.

Typically, over 60 minutes of continuous MEG was collected (sampling rate of 300 Hz, bandpass filter of 2 – 100 Hz). The localization analysis performed here used

short (2 - 3 second) windows centered around interictal spikes manually selected from the full data set (10 - 30 spikes for each patient).

9.2.3 Forward solution

The realistic boundary element method (BEM) was adapted for calculating the MEG forward solutions (39-41). The MEG forward solution computation requires the locations of all possible sources, the sensor locations, and sensor orientations. Each possible source location is represented by a triplet of orthogonal current dipoles. The MEG and MRI coordinate systems were manually aligned using numerous (> 30) digitized head points taken in the MEG coordinate system.

The computation of the MEG forward solution has been shown to only require the inner skull boundary to achieve an accurate solution (42-44). The surfaces required for computation of the forward solution (cortical surface and inner skull boundary) are semi-automatically reconstructed from high-resolution T1-weighted 3D MRI collected on each patient (45-47). The inner skull conductivity boundary is initially estimated with 2562 and then subsampled to 642 vertices. For reconstruction and visualization, the cortical surface is tessellated with about 150,000 vertices per hemisphere. For the inverse computation, the cortical surface is decimated to approximately 3000 dipoles per hemisphere, which is roughly equivalent to 1 dipole every 10 mm along the cortical surface. The subsampling of the cortical dipoles considerably speeds the forward computation, without sacrificing any accuracy in the final solution.

9.2.4 Inverse Approach

The linear estimation approach, which can be formulated in various equivalent methods (47-59), computes an optimal linear inverse operator. This operator maps the external electromagnetic field measurements into estimated source activities within the brain, while explicitly minimizing the expected error between the estimated and actual activity distribution. The calculation incorporates *a priori* spatial information (such as data from fMRI), the forward solution, and sensor noise characteristics. We estimated the sensor noise by computing the covariance of a selected portion of the time window prior to each interictal spike.

9.3 Results

The consistency of localization was quite variable from patient to patient. For two patients, there was a stereotypical interictal spike morphology. In the other patient, there was significant variation from spike to spike.

For Patient 1, the ten interictal spike localizations were similar. Two typical localizations are shown in Figure 1. The initial activity begins in the inferior frontal region and propagates more posteriorly along the inferior frontal region. For all 10 interictal spikes, the frontal pole was activated. In 8 of 10 interictal spikes, the propagation of activity proceeded from anterior to posterior.

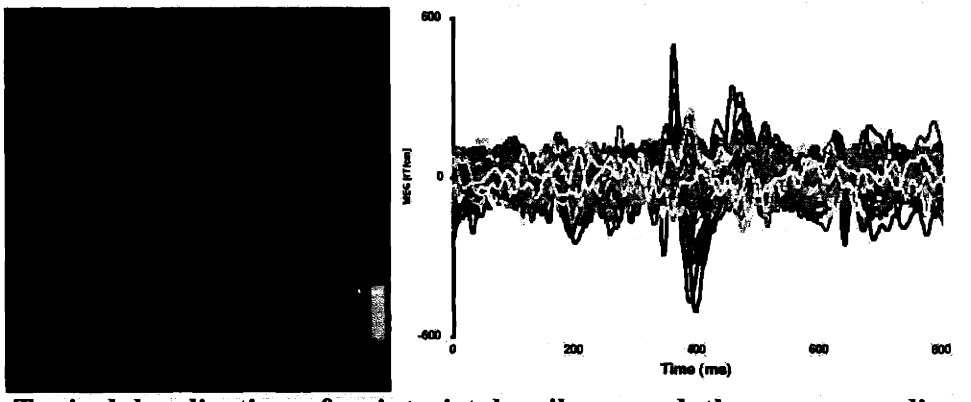

Figure 1: Typical localizations for interictal spikes and the corresponding MEG for Patient 1.

In this patient, the surgical resection is displayed in Figure 2. Intracranial measurements were made from the frontal pole, inferior frontal and subtemporal regions, based on the MEG results. The posterior limits of resection was based on the ictal and interictal spike patterns recorded from the subdural grids. The non-invasive localizations provided a good prediction of the region of resected region. Patient 1 has been seizure free since the surgery.

Figure 2: Surgical Resection for Patient 1. The intraoperative photograph has been coregistered with the cortical surface. The resected region is represented by the hashed region. The brain has been rotated to a slightly superior/lateral view.

Patient 2 had a large variety of spatial localizations. Interictal activity was localized to both hemispheres with no consistent pattern. Three example spatial locations are shown for both hemispheres (Figure 3). For a variety of reasons, Patient 2 has not gone onto surgery.

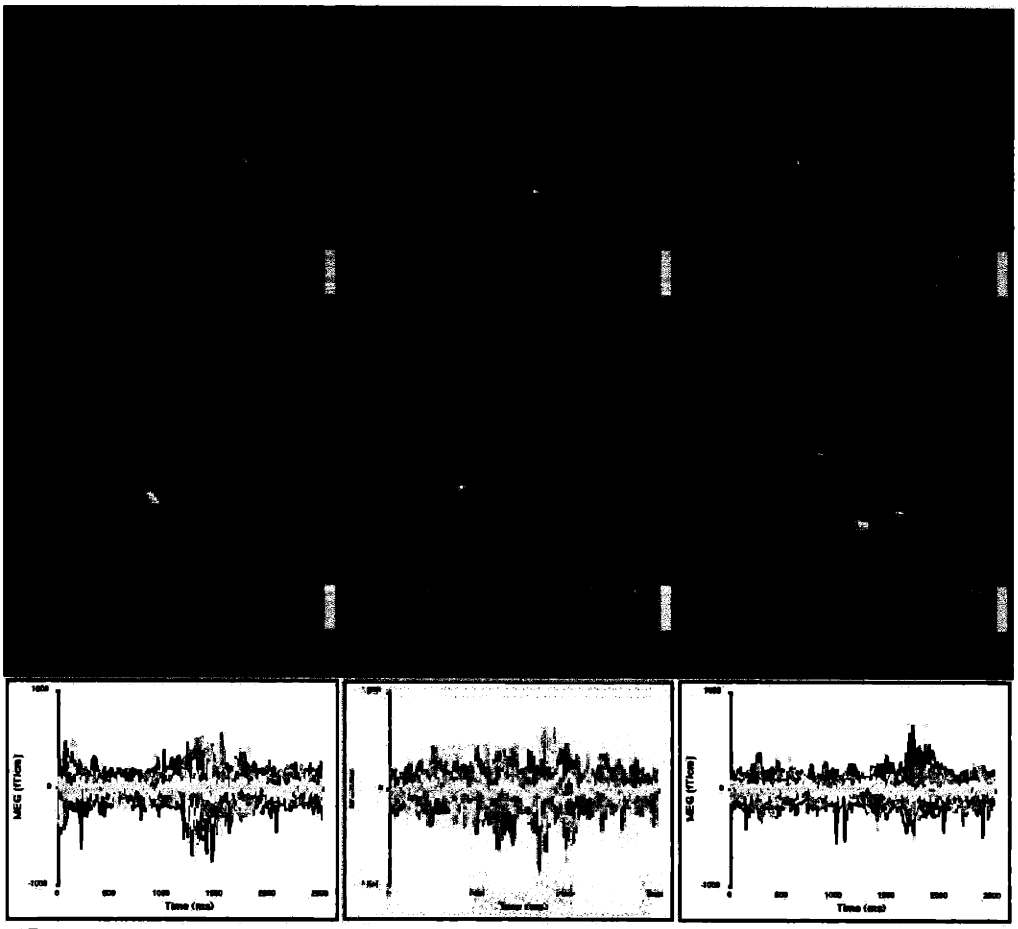

Figure 3: Example localizations of three interictal spikes for Patient 2. The upper row are left hemisphere localizations and the lower row are right hemisphere localizations. The corresponding MEG recordings are displayed in the bottom row.

For Patient 3, of the 22 spikes analyzed, only 3 showed no localizable activity. The remaining 19 spikes were more consistent in the localization. The temporal lobe was active in all 19 spikes. The next most consistent feature was simultaneous activity in the inferior frontal region and the temporal pole (8/22).

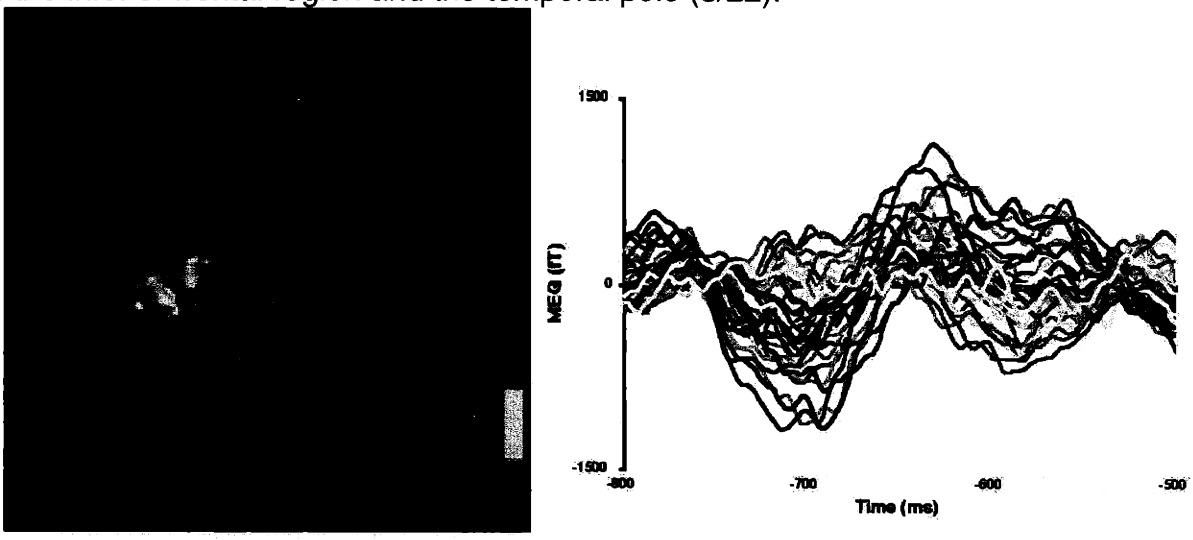

Figure 4: Typical localizations of interictal spikes and the corresponding MEG recording for Patient 3.

Intracranial measurements were also made for Patient 3. One recorded interictal discharge is shown in Figure 5. The initial activity was recorded from electrode I with immediate propagation to electrodes A, R, F and O. This is in excellent agreement with the MEG results. The surgical resection was located around electrodes I and O (lateral and orbitofrontal cortex). The patient has been seizure free for 3 years.

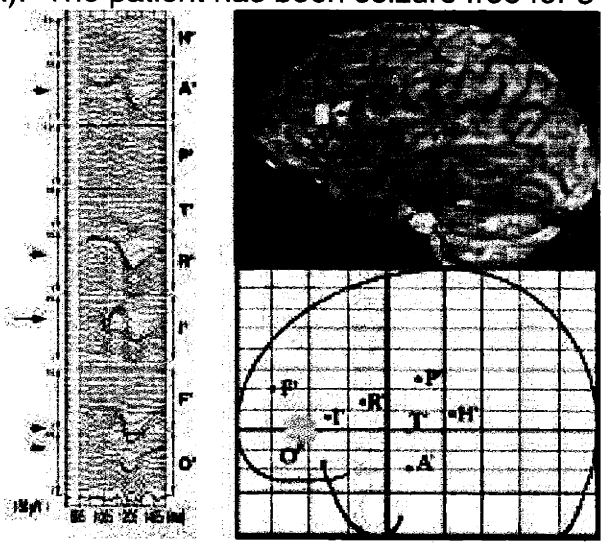

Figure 5: Intracranial measurement of an interictal spike for Patient 3.

9.4 Discussion

In two of the three patients, we found good agreement between the non-invasive MEG localization and intracranial measurements. For those two patients, we were able to determine both the initial site of interictal activity and the spatiotemporal propagation to other regions in the brain. The predictive ability of MEG in these cases was excellent. These MEG results would have provided an excellent guide to placement of intracranial electrodes.

The third patient (Patient 2), unfortunately, was less compelling. The morphology of the interictal spikes was extremely variable. Subsequently, we would be reluctant to speculate as to the actual location of the epileptic focus. In these situations, the interictal data would not be very helpful. While the entire clinical picture must taken into account, the variable localization results would suggest that this patient is not an optimal candidate for surgical treatment.

Although we only have a very limited number of patients, the preliminary results suggest that both positive and negative MEG findings would be useful. When there are consistent interictal spike localizations, those results are in good agreement with more invasive measurements. The placement of more invasive recordings should by guided by these non-invasive results. In comparison, for patients where the MEG results are more equivocal due to the wide variety of interictal spike morphology, more invasive recordings may not be warranted. In those situations, it may be unlikely that there is a well defined epileptic focus that would amenable to surgical treatment.

9.5 References

1. Adams RD, Victor M, and Ropper AH. Epilepsy and Other Seizure Disorders. In: eds. *Principles of Neurology*. New York: McGraw-Hill, 1997:
2. Hauser WA and Hesdorffer DC. *Epilepsy: frequency, causes and consequences*. New York City: Demos Press, 1990:
3. Robb P. Focal Epilepsy: The Problem, Prevalence, and Contributing Factors. In: Purpura DP, Penry JK, and Walter RD, eds. *Advances in Neurology*. New York: Raven Press, 1975: 356.
4. Engel J, Jr., Ness PCV, Ramussen TB, and Ojemann LM. Outcome with Respect to Epileptic Seizures. In: Jerome Engel J, eds. *Surgical Treatment of the Epilepsies*. New York City: Raven Press, 1993:
5. Luders HO, Engel J, Jr., and Munari C. General Principles. In: Engel J, Jr., eds. *Surgical Treatment of the Epilepsies*. New York City: Raven Press, 1993:
6. Engel J, Jr. Surgery for seizures. *N Engl J Med*. 1996; 334: 647-52.
7. Cohen D. Magnetoencephalography: Detection of the Brain's Electrical Activity with a Superconducting Magnetometer. *Science*. 1972; 175: 664-666.
8. Modena I, Ricci GB, and Barbanera S. Biomagnetic measurements of the spontaneous brain activity in epileptic patients. *Electroencephlogr. clin. Neurophysiol*. 1982; 54: 622-628.
9. Barth DS, Sutherling W, Engel JJ, and Beatty J. Neuromagnetic localization of epileptiform spike in the human brain. *Science*. 1982; 18: 891-894.
10. Barth DS, Sutherling W, Engel JJ, and Beatty J. Neuromagnetic evidence of spatially distributed sources underlying epileptiform spikes in the human brain. *Science*. 1984; 223: 293-296.
11. Sutherling WW, Crandall PH, Engel J, Jr., Darcey TM, Cahan LD, and Barth DS. The magnetic field of complex partial seizures agrees with intracranial localizations. *Ann Neurol*. 1987; 21: 548-58.
12. Stefan H, Schneider S, Feistel H, Pawlik G, Schuler P, Abraham-Fuchs K, Schlegel T, Neubauer U, and Huk WJ. Ictal and interictal activity in partial epilepsy recorded with multichannel magnetoelectroencephalography: correlation of electroencephalography/electrocorticography, magnetic resonance imaging, single photon emission computed tomography, and positron emission tomography findings. *Epilepsia*. 1992; 33: 874-87.
13. Ishibashi H, Morioka T, Shigeto H, Nishio S, Yamamoto T, and Fukui M. Three-dimensional localization of subclinical ictal activity by magnetoencephalography: correlation with invasive monitoring. *Surg Neurol*. 1998; 50: 157-63.
14. Ko DY, Kufta C, Scaffidi D, and Sato S. Source localization determined by magnetoencephalography and electroencephalography in temporal lobe epilepsy: comparison with electrocorticography: technical case report. *Neurosurgery*. 1998; 42: 414-21; discussion 421-2.
15. Mikuni N, Nagamine T, Ikeda A, Terada K, Taki W, Kimura J, Kikuchi H, and Shibasaki H. Simultaneous recording of epileptiform discharges by MEG and subdural electrodes in temporal lobe epilepsy. *Neuroimage*. 1997; 5: 298-306.

16. Brockhaus A, Lehnertz K, Wienbruch C, Kowalik A, Burr W, Elbert T, Hoke M, and Elger CE. Possibilities and limitations of magnetic source imaging of methohexital-induced epileptiform patterns in temporal lobe epilepsy patients. *Electroencephalogr Clin Neurophysiol.* 1997; 102: 423-36.
17. Kirchberger K, Schmitt H, Hummel C, Peinemann A, Pauli E, Kettenmann B, and Stefan H. Clonidine and methohexital-induced epileptic magnetoencephalographic discharges in patients with focal epilepsies. *Epilepsia.* 1998; 39: 841-9.
18. Otsubo H, Sharma R, Elliott I, Holowka S, Rutka JT, and Snead OC, 3rd. Confirmation of two magnetoencephalographic epileptic foci by invasive monitoring from subdural electrodes in an adolescent with right frontocentral epilepsy. *Epilepsia.* 1999; 40: 608-13.
19. Wheless JW, Willmore LJ, Breier JI, Kataki M, Smith JR, King DW, Meador KJ, Park YD, Loring DW, Clifton GL, Baumgartner J, Thomas AB, Constantinou JE, and Papanicolaou AC. A comparison of magnetoencephalography, MRI, and V-EEG in patients evaluated for epilepsy surgery. *Epilepsia.* 1999; 40: 931-41.
20. Nakasato N, Levesque MF, Barth DS, Baumgartner C, Rogers RL, and Sutherling WW. Comparisons of MEG, EEG, and ECoG source localization in neocortical partial epilepsy in humans. *Electroencephalogr Clin Neurophysiol.* 1994; 91: 171-8.
21. Sutherling WW, Crandall PH, Cahan LD, and Barth DS. The magnetic field of epileptic spikes agrees with intracranial localizations in complex partial epilepsy. *Neurology.* 1988; 38: 778-86.
22. Paetau R, Kajola M, Karhu J, Nousiainen U, Partanen J, Tiihonen J, Vapalahti M, and Hari R. Magnetoencephalographic localization of epileptic cortex--impact on surgical treatment. *Ann Neurol.* 1992; 32: 106-9.
23. Sutherling WW and Barth DS. Neocortical propagation in temporal lobe spike foci on magnetoencephalography and electroencephalography. *Ann. Neurology.* 1989; 25: 373-381.
24. Stefan H, Schneider S, Abraham-Fuchs K, Bauer J, Feistel H, Pawlik G, Neubauer U, Rohrlein G, and Huk WJ. Magnetic source localization in focal epilepsy. Multichannel magnetoencephalography correlated with magnetic resonance brain imaging. *Brain.* 1990; 113: 1347-59.
25. Tiihonen J, Hari R, Kajola M, Nousiainen U, and Vapalahti M. Localization of epileptic foci using a large-area magnetometer and functional brain anatomy [see comments]. *Ann Neurol.* 1990; 27: 283-90.
26. Eisenberg HM, Papanicolaou AC, Baumann SB, Rogers RL, and Brown LM. Magnetoencephalographic localization of interictal spike sources. Case report. *J Neurosurg.* 1991; 74: 660-4.
27. Aung M, Sobel DF, Gallen CC, and Hirschkoff EC. Potential contribution of bilateral magnetic source imaging to the evaluation of epilepsy surgery candidates. *Neurosurgery.* 1995; 37: 1113-20; discussion 1120-1.
28. Diekmann V, Becker W, Jurgens R, Grozinger B, Kleiser B, Richter HP, and Wollinsky KH. Localisation of epileptic foci with electric, magnetic and combined electromagnetic models. *Electroencephalogr Clin Neurophysiol.* 1998; 106: 297-313.

29.Hari R, Ahonen A, Forss N, Granstrom ML, Hamalainen M, Kajola M, Knuutila J, Lounasmaa OV, Makela JP, Paetau R, and et al. Parietal epileptic mirror focus detected with a whole-head neuromagnetometer. *Neuroreport.* 1993; 5: 45-8.
30.Bamidis PD, Hellstrand E, Lidholm H, Abraham-Fuchs K, and Ioannides AA. MFT in complex partial epilepsy: spatio-temporal estimates of interictal activity. *Neuroreport.* 1995; 7: 17-23.
31.Fuchs M, Drenckhahn R, Wischmann HA, and Wagner M. An improved boundary element method for realistic volume-conductor modeling. *IEEE Trans Biomed Eng.* 1998; 45: 980-97.
32.Merlet I, Garcia-Larrea L, Gregoire MC, Lavenne F, and Mauguiere F. Source propagation of interictal spikes in temporal lobe epilepsy. Correlations between spike dipole modelling and [18F]fluorodeoxyglucose PET data. *Brain.* 1996; 119: 377-92.
33.Lounasmaa OV, Hamalainen M, Hari R, and Salmelin R. Information processing in the human brain: magnetoencephalographic approach. *Proc Natl Acad Sci U S A.* 1996; 93: 8809-15.
34.Paetau R, Hamalainen M, Hari R, Kajola M, Karhu J, Larsen TA, Lindahl E, and Salonen O. Magnetoencephalographic evaluation of children and adolescents with intractable epilepsy. *Epilepsia.* 1994; 35: 275-84.
35.Kamada K, Moller M, Saguer M, Kassubek J, Kaltenhauser M, Kober H, Uberall M, Lauffer H, Wenzel D, and Vieth J. Localization analysis of neuronal activities in benign rolandic epilepsy using magnetoencephalography. *J Neurol Sci.* 1998; 154: 164-72.
36.Paetau R, Granstrom ML, Blomstedt G, Jousmaki V, Korkman M, and Liukkonen E. Magnetoencephalography in presurgical evaluation of children with the Landau-Kleffner syndrome. *Epilepsia.* 1999; 40: 326-35.
37.Minami T, Gondo K, Yamamoto T, Yanai S, Tasaki K, and Ueda K. Magnetoencephalographic analysis of rolandic discharges in benign childhood epilepsy. *Ann Neurol.* 1996; 39: 326-34.
38.Lewine JD, Andrews R, Chez M, Patil AA, Devinsky O, Smith M, Kanner A, Davis JT, Funke M, Jones G, Chong B, Provencal S, Weisend M, Lee RR, and Orrison WW, Jr. Magnetoencephalographic patterns of epileptiform activity in children with regressive autism spectrum disorders [see comments]. *Pediatrics.* 1999; 104: 405-18.
39.Barnard ACL, Duck IM, Lynn MS, and Timlake WP. The application of electromagnetic field theory to electrocardiography - II: Numerical solution of the integral equations. *Biophys.* 1967; 7: 463-491.
40.de Munck JC. A linear discretization of the volume conductor boundary integral equation using analytically integrated elements. *IEEE Trans. Biomed. Eng.* 1992; 39: 986-990.
41.Oostendorp TF and van Oosterom A. Source parameter estimation using realistic geometry in bioelectricity and biomagnetism. In: Nenonen J, Rajala HM, and Katila T, eds. *Biomagnetic Localization and 3D Modeling, Report TKK-F-A689.* Helsinki: Helsinki University of Technology, 1992:

42.Meijs JWH, Bosch FGC, Peters MJ, and Lopes da Silva FH. On the magnetic field distribution generated by a dipolar current source situated in a realistically shaped compartment model of the head. *Electroenceph. Clin. Neurophysiol.* 1987; 66: 286-298.
43.Hamalainen MS and Sarvas J. Realistic conductivity geometry model of the human head for interpretation of neuromagnetic data. *IEEE Trans. Biomed. Eng.* 1989; 36: 165-171.
44.Meijs JWH, Weier OW, Peters MJ, and Van Oosterom A. On the numerical accuracy of the boundary element method. *IEEE Trans.Biomed.Eng.* 1989; 36: 1038-1049.
45.Dale AM, Fischl B, and Sereno MI. Cortical Surface-Based Analysis I: Segmentation and Surface Reconstruction. *NeuroImage.* 1999; 9: 179-194.
46.Fischl B, Sereno MI, and Dale AM. Cortical Surface-Based Analysis II: Inflation, Flattening, and a Surface-Based Coordinate System. *NeuroImage.* 1999; 9: 195-207.
47.Dale AM and Sereno MI. Improved localization of cortical activity by combining EEG and MEG with MRI cortical surface reconstruction: A linear approach. *J. Cog. Neurosci.* 1993; 5: 162-176.
48.Hamalainen MS and Ilmoniemi RJ. *Interpreting measured magnetic fields of the brain: estimates of current distributions.* Helsinki, Finland: Helsinki Univ. of Technology, 1984:
49.Dale AM. *Source Localization and Spatial Discriminant Analysis of Event-Related Potentials: Linear Approaches.* Ph.D., University of California, San Diego, 1994.
50.Hamalainen MS and Ilmoniemi RJ. Interpreting magnetic fields of the brain: minimum norm estimates. *Med Biol Eng Comput.* 1994; 32: 35-42.
51.Gelb A. *Applied Optimal Estimation.* Cambridge: MIT Press, 1974: pp. 374.
52.Phillips JW, Leahy RM, Mosher JC, and Timsari B. Imaging neural activity using MEG and EEG. *IEEE Eng Med Biol Mag.* 1997; 16: 34-42.
53.Phillips JW, Leahy RM, and Mosher JC. MEG-based imaging of focal neuronal current sources. *IEEE Trans Med Imaging.* 1997; 16: 338-48.
54.Schmidt DM, George JS, and Wood CC. Bayesian inference applied to the electromagnetic inverse problem. *Hum Brain Mapp.* 1999; 7: 195-212.
55.Tichonov AN and Arsenin VY. *Solutions of ill-posed problems.* Washington D.C.: Winston, English translation by F. John, 1977:
56.Deutsch R. *Estimation Theory.* Englewood Cliffs, NJ: Prentice Hall, 1965:
57.Smith WE. Estimation of the spatio-temporal correlations of biological electrical sources from their magnetic field. *IEEE Trans Biomed Eng.* 1992; 39: 997-1004.
58.Sekihara K and Scholz B. Average-intensity reconstruction and Wiener reconstruction of bioelectric current distribution based on its estimated covariance matrix. *IEEE Trans Biomed Eng.* 1995; 42: 149-157.
59.Sekihara K and Scholz B. Generalized Weiner estimation of three-dimensional current distribution from biomagnetic measurements. *IEEE Trans Biomed Eng.* 1996; 43: 281-291.

10. Conclusions

In this thesis I have described a neuroimaging method that provides both high spatial and temporal resolution. This approach combines information from fMRI, EEG, and MEG. In Chapter 1, I describe the various types of physiological constraints that can be used to improved the forward (e.g. cortical surface) and inverse (e.g. fMRI) solutions. In Chapter 2, I provide an mathematical overview of the forward problem and various derivations of the linear estimation inverse operator.

The modeling results are presented in Chapters 3-5. In Chapter 3, model studies using a volumetric spherical head model (i.e. unconstrained by the cortical surface) demonstrated the effect of extra fMRI sources, missing fMRI sources, and a spatial mis-registration between the fMRI and EEG/MEG coordinate systems. Using a more realistic head model (realistic geometry and cortical surface) in Chapter 4, I show that an intermediate fMRI weighting produces a reasonable compromise between minimizing the crosstalk between areas of fMRI activation and the larger error from missing fMRI sources. I also show the relative independence from the extent and number of sources, and the minimal dependence on errors in the cortical orientation. The final set of modeling studies in Chapter 5 examined the effect of EEG, MEG, and combined EEG/MEG sensor configurations. The results show that EEG has better accuracy than MEG for the same number of sensors, but the best spatial resolution and accuracy is provided by combined EEG/MEG configurations. I also present a noise sensitivity normalization of the traditional linear estimator that improves the average point spread, increases the spatial homogeneity of the point spread, and allows for a statistical interpretation of movies of brain activity.

The remaining four chapters describe various experimental studies. Chapter 6 presents validation and comparison of the realistic and spherical BEM head models. Using data from implanted electrodes in an epilepsy patient, I found the improvement of the realistic head model versus the spherical head model for ventral sources. Also, this data allowed the initial estimation of the absolute resisitivities for the three regions in the BEM head model (i.e. scalp, skull, and brain). The absolute resisitivities are crucial for proper combination of EEG with MEG for source localization.

The last three chapters present applications of this multimodal imaging approach to experimental data. Simultaneous EEG/fMRI data acquisition is shown in Chapter 7. Although the SNR of both the EEG and fMRI data were low, I was still able to perform the source localization. Chapter 8 presents a combined fMRI/MEG study of visual motion coherency. While numerous cortical areas were active, I focused on the motion coherency effects in areas MT and SPO. This data demonstrated latency differences between the two areas, latency shifts between coherent and incoherent motion for a given area, and modulations in amplitude between motion conditions. These data support the view that neural changes in both amplitude and timing within a cortical network underlie the perception of particular stimulus attributes, in agreement with theoretical predictions. Finally, localization of MEG measurements of interictal spikes in three epilepsy patients in shown in Chapter 9. For two patients, the non-invasive localizations were consistent across different interictal spikes, and were in good

agreement with the surgical and the intra-cranial measurements. Both of those patients have clinical improvements in their seizure activity. In the third patient, the non-invasive localizations were extremely variable. That patient has not gone onto surgery at this time.

In summary, this thesis has presented a convincing validation of some of the currently available forward models and inverse approaches. This should improve the confidence of the localizations provided by these techniques, allowing more advanced studies of the human mind at work.